

PATTERN RECOGNITION AND CLASSIFICATION OF CT IMAGES OF DIFFUSE
LUNG DISEASES USING FEATURE EXTRACTION AND
ARTIFICIAL NEURAL NETWORKS



PATTERN RECOGNITION AND CLASSIFICATION
OF CT IMAGES OF DIFFUSE LUNG DISEASES
USING FEATURE EXTRACTION AND
ARTIFICIAL NEURAL NETWORKS



By MEHRDAD ALEMZADEH, B.Sc., M.Sc.

A THESIS

SUBMITTED TO THE SCHOOL OF GRADUATE STUDIES AT

MCMASTER UNIVERSITY

IN PARTIAL FULFILMENT OF THE REQUIREMENTS FOR THE DEGREE

OF

DOCTOR OF PHILOSOPHY

McMaster University © Copyright by Mehrdad Alemzadeh, March 2016

Doctor of Philosophy (2016)
Computing and Software

McMaster University
Hamilton, Ontario, Canada

TITLE	PATTERN RECOGNITION AND CLASSIFICATION OF CT IMAGES OF DIFFUSE LUNG DISEASES USING FEATURE EXTRACTION AND ARTIFICIAL NEURAL NETWORKS
AUTHOR	MEHRDAD ALEMZADEH, B.Sc., M.Sc.
SUPERVISOR	Prof. Markad V. Kamath
NUMBER OF PAGES	xxiii, 227

ABSTRACT

Diffuse Lung Diseases (DLD), impute to 15% of respiratory practice and are accountable for a large class of disorders, primarily affecting lung parenchyma. As a part of the diagnostic workup by the physician, a chest CT image is often required in addition to a thorough medical history and physical examination. The reliable identification of the features among interstitial lung diseases and the patterns they may take is challenging, particularly given the volume of data on a CT scan that must be processed by the radiologist. It has been shown that even among expert chest radiologists there is significant inter-observer and intra-observer variability.

To make an objective quantitative and qualitative assessment of lung disease patterns, an accurate and reliable computer aided diagnostic system is likely to be extremely useful to assist with dealing with data volume for an expert radiologist. There will also be the opportunity to improve sensitivity and specificity in a non-expert radiologist group. Literature suggests that computer based pattern classifiers can discern image abnormalities due to lung diseases such as consolidation, cyst, emphysema, fibrosis, ground glass opacity, honey combing, nodularity, reticulation, scar and tree-in-bud.

Researchers have focused on developing algorithms to quantify and analyse the surface changes of the lung, since DLD patterns often manifest as texture differences within the lung parenchyma. Research reported in this thesis has incorporated texture quantification, fractal analysis and scale invariant feature transform methods as complementary feature extraction techniques to improve the classification accuracy, especially in the presence of

large number of classes associated with interstitial diseases. Classification of ten lung pathologies and healthy lung regions are validated based on different combination of diseases using leave-one-out and 5-fold cross validation techniques and an Artificial Neural Network (ANN).

Classification accuracy based on features selected using scale invariant feature transform method alone generates 99% accuracy for up to four classes and more than 71% for up to eleven classes using an ANN. Classification accuracy is 85% for eleven classes using a combination of scale invariant feature transform, texture and fractal based features. Classification accuracies improve for higher number of classes (> 5) when the combination of above mentioned features are incorporated. Detailed classification accuracies for several DLD features compared to a healthy lung, and combinations of DLD features, such as fibrosis, reticulation, honey combing in comparison with healthy lung are evaluated throughout this thesis.

ACKNOWLEDGEMENTS

I would like to thank Prof. Markad V. Kamath who has been supporting and guiding me throughout this research. Your advices and guidance both academically and in life is much appreciated. THANK YOU.

My sincere thanks goes to Dr. Colm Byolan and St. Joseph's Healthcare Hamilton, Chair of the Radiology Department. Without his selfless devotion and insights, research reported in this thesis would have not been possible.

I would also like to express my gratitude to late Dr. Skipper Poehlman who put his trust in me as one of his last students and provided me with PhD admission at McMaster University.

Foremost, I should thank my lovely wife Negar, my dearest parents and my sister Farnoosh, for being there for me during all the challenges and difficulties. They are the reason I engaged in graduate studies.

Last but not least, I should thank Dr. Myrna Dolovich for the space she provided in Aerosol Lab at St. Joseph's Hospital.

تقدیم به هما و رضا

Contents

Abstract	iii
Acknowledgements.....	v
CHAPTER 1	
INTRODUCTION.....	1
I. preface.....	2
II. Motivation.....	4
III. Problem Statement and Challenges.....	4
IV. Contributions.....	6
V. Limitations	8
VI. Thesis Structure.....	9
CHAPTER 2	
A REVIEW OF TEXTURE QUANTIFICATION OF CT IMAGES FOR CLASSIFICATION OF LUNG DISEASES	11
I. Introduction	12
II. Texture Analysis	13
A. Feature Extraction	14
1. Structural Methods	15
2. Statistical Methods	15
3. Model Based Methods.....	19
III. Segmentation.....	24
A. Texture Based Segmentation	24
IV. Classification.....	28
V. Fractal Texture Analysis	29
VI. Applications of Texture analysis toward diagnosis Using CT images of the lung in diagnosis of DLD	31
A. Identification of Abnormal Image segments	32
1. Emphysema.....	40

2. Cancer	42
VII. Application of Scale Invariant Feature Transform in CT Images of The Lung .	45
VIII. Assessment	48
IX. Discussion	49
X. Chapter Summary	50

CHAPTER 3

EVALUATION OF TEXTURE FEATURES OF PATHOLOGICAL PATTERNS

IN THE CT IMAGES OF THE LUNG.....	52
I. Introduction.....	53
II. Feature Extraction using Texture Based Methods	53
A. Tamura Features	54
B. Compound Local Binary Pattern Algorithm	58
C. Gray Level Co-occurrence Matrix	60
D. Haralick Features.....	62
E. Gabor Filter Analysis	77
F. Geometric Quantification based on Minkowski Functionals	80
III. Processing of Labelled CT Image Data and Training of the ANN.....	85
IV. Classification Accuracy of Feature Sets Derived From Various Texture Analysis Methods.....	89
V. Results.....	98
VI. Chapter Summary	100

CHAPTER 4

CLASSIFICATION OF CT IMAGES OF THE LUNG USING

FRACTIONAL DIMENSIONAL ANALYSIS.....	101
I. Introduction.....	102
II. Mathematical preliminaries.....	102
A. Segmentation-based Fractal Texture Analysis	106
B. Box Counting Algorithm.....	108
C. Fractal Dimension Semi Variance Feature extraction Technique.....	109
III. Accuracy of Classification of CT Image of The Lung Based on Fractal Features	

IV. Classification Accuracies of The Combination of Texture and Fractal Features .	114
V. Results.....	115
VI. Chapter Summary	117

CHAPTER 5

SCALE INVARIANT FEATURE TRANSFORM FOR CLASSIFICATION OF CT IMAGES OF THE LUNG.....118

I. Introduction.....	119
II. SIFT Methodology and Algorithm description.....	119
A. Edge and Corner versus SIFT Interest Point.....	121
B. SIFT Transformation Using Gaussian Filter.....	124
C. Edge Detection Based on Scale-Space.....	126
1. Detecting Interest Points Using Zero Crossing Method.....	127
2. Identifying Interesting Points Using Interval tree	130
D. Potential key-Point Identification Using Laplacian of Gaussian or Difference of Gaussian.....	131
E. Eliminating Outliers Using Taylor Series and Hessian Matrix.....	136
F. Evaluation of Key-Point Orientation and Descriptor Vector.....	138
III. Processing of Labelled CT Image Data and Training of the ANN Algorithm	140
IV. Results of Classification of CT images of the lung Based on SIFT Features.....	141
VI. Accuracy of Classification Based on A Combination of SIFT and Texture and Fractal Features	144
VII. Results.....	145
VIII. Chapter Summary.....	147

CHAPTER 6

CLASSIFICATION ACCURACY OF TEXTURE, FRACTAL AND SIFT METHODOLOGIES USING 5-FOLD CROSS VALIDATION ON ANN.....149

I. Introduction.....	150
II. 5-Fold Cross Validation Technique.....	150
III. Classification Accuracy Based on Texture Features.....	153
IV. Classification Accuracy Based on Fractal and Texture Features.....	163
V. Classification Accuracy Based on SIFT, Texture and Fractal Features	165

VI. Comparison of Classification Accuracy of Leave-one-out and 5-Fold Cross validation.....	168
VII. Support Vector Machine Classification Results on SIFT.....	171
VIII. Chapter Summary.....	171
CHAPTER 7	
SUMMARY AND CONCLUSIONS.....	173
I. Introduction.....	174
II. Research Summary and Conclusion.....	174
III. Contributions.....	181
IV. Future Work.....	182
Appendix I: DIFFUSE LUNG DISEASES.....	185
Appendix II: Minkowski Functionals.....	193
APPENDIX III: Most Popular Classifiers in Medical Imaging.....	195
A. Artificial Neural Networks.....	195
B. Support Vector Machine.....	200
C. K-Nearest Neighbor.....	203
References.....	205

List of Tables

TABLE 1.1 SEGMENTATION ALGORITHMS IN IDENTIFYING DISEASES IN THE LUNG	28
TABLE 3.1 NUMBER OF PATIENTS AND ROI'S PER CLASS	87
TABLE 3.2 AN EXAMPLE OF ANN AVERAGE CLASSIFICATION ACCURACY FOR ANY GENERAL FEATURE	88
TABLE 3.3 ANN AVERAGE CLASSIFICATION ACCURACY BASED ON COARSENESS, TAMURA TEXTURE METHOD	90
TABLE 3.4 ANN AVERAGE CLASSIFICATION ACCURACY BASED ON TAMURA'S CONTRAST FEATURE	91
TABLE 3.5 ANN AVERAGE CLASSIFICATION ACCURACY BASED ON DIRECTIONALITY, TAMURA TEXTURE METHOD	91
TABLE 3.6 ANN AVERAGE CLASSIFICATION ACCURACY BASED ON ALL THREE TAMURA TEXTURE FEATURES SHOWS BETTER RESULTS COMPARED TO WHEN ONLY ONE OF THE FEATURES WERE USED	92
TABLE 3.7 ANN AVERAGE CLASSIFICATION ACCURACY BASED ON COMPOUND LOCAL BINARY PATTERN (CLBP) ALGORITHM	93
TABLE 3.8 ANN AVERAGE CLASSIFICATION ACCURACY BASED ON GRAY LEVEL CO- OCCURRENCE MATRIX (GLCM) SHOWS BETTER RESULTS COMPARED TO SINGLE TAMURA FEATURES	93
TABLE 3.9 ANN AVERAGE CLASSIFICATION ACCURACY BASED ON ALL THIRTEEN HARALICK TEXTURE FEATURES SHOWS HIGHEST CLASSIFICATION COMPARED TO ALL OTHER METHODS	94
TABLE 3.10 ANN AVERAGE CLASSIFICATION ACCURACY BASED ON IFFT, GABOR FILTER METHOD	95
TABLE 3.11 ANN CLASSIFICATION ACCURACY BASED ON TEXTURE ENERGY FEATURE USING GABOR FILTER	95
TABLE 3.12 ANN AVERAGE CLASSIFICATION ACCURACY BASED ON TRANSFORMED IFFT, GABOR FILTER METHOD	95

TABLE 3.13 ANN AVERAGE CLASSIFICATION ACCURACY BASED ON ALL THREE GABOR FILTER TEXTURE FEATURES SHOWS HIGHER CLASSIFICATION RESULTS THAN WHEN ONLY ONE OF THE FEATURE WAS USED	96
TABLE 3.14 ANN AVERAGE CLASSIFICATION ACCURACY BASED ON MINKOWSKI’S GEOMETRIC FUNCTIONALS.....	96
TABLE 3.15 ANN AVERAGE CLASSIFICATION ACCURACY BASED ON ALL TEXTURE FEATURES	97
TABLE 3.16 SPECIFICITY AND SENSITIVITY OF ALL TEXTURE FEATURES BASED ON 2, 3 AND 11 CLASSES	99
TABLE 4.1 ANN AVERAGE CLASSIFICATION ACCURACY BASED ON SFTA FEATURE ANALYSIS.....	112
TABLE 4.2 ANN AVERAGE CLASSIFICATION ACCURACY BASED ON BOX COUNTING FEATURE ANALYSIS.....	112
TABLE 4.3 ANN CLASSIFICATION ACCURACY BASED ON FD SEMI-VARIANCE ANALYSIS..	113
TABLE 4.4 ANN CLASSIFICATION ACCURACY BASED ON ALL FRACTAL DIMENSION FEATURES IN THE PRESENT CHAPTER	113
TABLE 4.5 ANN CLASSIFICATION ACCURACY BASED ON ALL FD AND ALL TEXTURE FEATURES	114
TABLE 5.1 ANN CLASSIFICATION ACCURACY BASED ON SIFT FEATURES	142
TABLE 5.2 ANN CLASSIFICATION ACCURACY BASED ON SIFT AND ALL TEXTURE FEATURES	143
TABLE 5.3 ACCURACY OF ANN CLASSIFICATION OF CT LUNG IMAGES USING SIFT, FOR TEXTURE AND FEATURES FROM FRACTAL DESCRIPTION OF THE IMAGE	144
TABLE 6.1 ANN AVERAGE CLASSIFICATION ACCURACY BASED ON TAMURA’S COARSENESS FEATURE	154
TABLE 6.2 ANN AVERAGE CLASSIFICATION ACCURACY BASED ON CONTRAST; A TAMURA TEXTURE FEATURE.....	154
TABLE 6.3 ANN AVERAGE CLASSIFICATION ACCURACY BASED ON DIRECTIONALITY; A TAMURA TEXTURE FEATURE	155

TABLE 6.4 ANN AVERAGE CLASSIFICATION ACCURACY BASED ON ALL THREE TAMURA TEXTURE FEATURES SHOWS BETTER RESULTS COMPARED TO WHEN ONLY ONE OF THE FEATURES WERE USED	156
TABLE 6.5 ANN AVERAGE CLASSIFICATION ACCURACY BASED ON CLBP	156
TABLE 6.6 ANN AVERAGE CLASSIFICATION ACCURACY BASED ON GLCM SHOWS BETTER RESULTS COMPARED TO SINGLE TAMURA FEATURES	157
TABLE 6.7 ANN AVERAGE CLASSIFICATION ACCURACY BASED ON ALL THIRTEEN HARALICK TEXTURE FEATURES SHOWS BEST CLASSIFICATION RESULTS AMONG ALL OTHER METHODS	158
TABLE 6.8 ANN AVERAGE CLASSIFICATION ACCURACY BASED ON ALL THREE GABOR FILTER TEXTURE FEATURES SHOWS BETTER RESULTS THAN WHEN ONLY ONE OF THE FEATURES WERE USED	158
TABLE 6.9 AVERAGE ACCURACY OF CLASSIFICATION FOR MINKOWSKI GEOMETRIC FUNCTIONALS.....	159
TABLE 6.10 ANN AVERAGE CLASSIFICATION ACCURACY BASED ON ALL TEXTURE FEATURES SHOWS A WELL-TRAINED ANN READY FOR CLASSIFICATION.....	160
TABLE 6.11. ANN CLASSIFICATION ACCURACY BASED ON ALL FRACTAL DIMENSION FEATURES	163
TABLE 6.12. ANN CLASSIFICATION ACCURACY BASED ON ALL FD AND ALL TEXTURE FEATURES	164
TABLE 6.13. ANN CLASSIFICATION ACCURACY BASED ON SIFT FEATURES USING 5-FOLD CROSS VALIDATION.....	165
TABLE 6.14. ANN CLASSIFICATION ACCURACY BASED ON SIFT AND ALL TEXTURE FEATURES	166
TABLE 6.15. ANN CLASSIFICATION ACCURACY BASED ON SIFT, ALL TEXTURE AND FD FEATURES	166
TABLE 6.16. AVM CLASSIFICATION ACCURACY BASED ON SIFT FEATURES USING 5-FOLD CROSS VALIDATION.....	171

TABLE 7.1 NUMBER OF FEATURES FOR EACH TEXTURE, FRACTAL AND SIFT METHOD ARE
REPRESENTED 179

List of Figures

FIGURE 1.1 IMAGES OF TEN PATHOLOGICAL DLD PATTERNS AND OF A HEALTHY LUNG	5
FIGURE 2.1 NORMAL LUNG	13
FIGURE 2.2: FOUR DIRECTIONS AND ITS EIGHT NEIGHBORING PIXELS.....	17
FIGURE 2.3. GROUND GLASS DENSITY WITH TRACTION BRONCHIECTASIS AS INDICATED BY ARROWS.....	34
FIGURE 2.4. PARA-SEPTAL EMPHYSEMA AND CENTRI-LOBULAR EMPHYSEMA, IDENTIFIED BY ARROWS.....	41
FIGURE 3.1. TAMURA FEATURES OF A CT IMAGE FROM A PATIENT WITH GGO. TOP LEFT: ORIGINAL IMAGE; ALL OTHERS ARE IMAGE REPRESENTATIONS OF THEIR FEATURES WITH THE VALUES CALCULATED FOR EACH	56
FIGURE 3.2 EFFECTS OF TAMURA FEATURES ON AN IMAGE IDENTIFIED WITH EMPHYSEMA; TOP LEFT: ORIGINAL IMAGE; ALL OTHER IMAGES ARE VALUES DERIVED FROM TAMURA FEATURES	57
FIGURE 3.3 UPPER LEFT CORNER (A) SHOWS PIXEL VALUES AROUND A CENTERED PIXEL. UPPER MIDDLE (B) IS THE LPB EVALUATION. UPPER RIGHT CORNER (C) IS CT IMAGE OF LUNG IDENTIFIED WITH HONEY COMBING AND GGO. THE ABOVE GRAPH DEMONSTRATES THE HISTOGRAM OF THE CT IMAGE BASE ON CLBP	59
FIGURE 3.4 GLCM EVALUATION OF AN IMAGE WITH DIFFERENT OFFSETS	62
FIGURE 3.5 SAMPLE IMAGE ROIS FROM DIFFERENT PATHOLOGIES. COMPARING ENERGY VALUE ON TWO SETS OF HONEY COMBING, CONSOLIDATION, EMPHYSEMA & GGO SHOWS SIMILAR RANGE OF VALUES. THIS FEATURE IS WELL DESCRIPTIVE FOR GGO (UPPER:0.22; LOWER:0.24)	64
FIGURE 3.6 A COMPARISON OF CONTRAST VALUES ON TWO SETS OF HONEY COMBING, CONSOLIDATION, EMPHYSEMA & GGO SHOWS SIMILAR VALUES. CONTRAST FEATURE IS WELL DESCRIPTIVE FOR HONEY COMBING (UPPER:0.92) AND EMPHYSEMA (UPPER IMAGE:1.1; LOWER IMAGE:0.95)	65

FIGURE 3.7 A COMPARISON OF CORRELATION VALUES ON TWO SETS OF HONEY COMBING, CONSOLIDATION, EMPHYSEMA & GGO SHOWS SIMILAR VALUES	66
FIGURE 3.8 A COMPARISON OF SUM OF SQUARES VARIANCE VALUES ON TWO SETS OF HONEY COMBING, CONSOLIDATION, EMPHYSEMA & GGO. THIS FEATURE WORKS BETTER FOR HONEY COMBING AND EMPHYSEMA AS THE RESULTS ARE IN THE SAME RANGE	67
FIGURE 3.9 A COMPARISON OF INVERSE DIFFERENT MOMENT VALUE ON TWO SETS OF HONEY COMBING, CONSOLIDATION, EMPHYSEMA & GGO SHOWS SIMILAR RANGE OF VALUES	68
FIGURE 3.10 A COMPARISON OF SUM AVERAGE VALUE ON TWO SETS OF HONEY COMBING, CONSOLIDATION, EMPHYSEMA & GGO SHOWS SIMILAR RANGE OF VALUES	69
FIGURE 3.11 A COMPARISON OF ENTROPY VALUES ON TWO SETS OF HONEY COMBING, CONSOLIDATION, EMPHYSEMA & GGO SHOWS SIMILAR RANGE OF VALUES	70
FIGURE 3.12 A COMPARISON OF SUM ENTROPY VALUE ON TWO SETS OF HONEY COMBING, CONSOLIDATION, EMPHYSEMA & GGO SHOWS SIMILAR RANGE OF VALUES	71
FIGURE 3.13 A COMPARISON OF DIFFERENCE VARIANCE ON TWO SETS OF HONEY COMBING, CONSOLIDATION, EMPHYSEMA & GGO SHOWS BETTER RESULTS FOR CONSOLIDATION AS THE RANGE IS MUCH SIMILAR	72
FIGURE 3.14 A COMPARISON OF DIFFERENCE ENTROPY ON TWO SETS OF HONEY COMBING, CONSOLIDATION, EMPHYSEMA & GGO SHOWS SIMILAR RANGE OF VALUES	73
FIGURE 3.15 A COMPARISON OF SUM VARIANCE ON TWO SETS OF HONEY COMBING, CONSOLIDATION, EMPHYSEMA & GGO	74
FIGURE 3.16 A COMPARISON OF INFO. MEASURE OF CORRELATION 1 ON TWO SETS OF HONEY COMBING, CONSOLIDATION, EMPHYSEMA & GGO	75
FIGURE 3.17 A COMPARISON OF INFO. MEASURE OF CORRELATION 2 ON TWO SETS OF HONEY COMBING, CONSOLIDATION, EMPHYSEMA & GGO SHOWS SIMILAR RANGE OF VALUES	76
FIGURE 3.18 EIGHTEEN ORIENTATIONS OF GABOR FILTER, USED FOR FEATURE EXTRACTION; EACH DIFFERING FROM EACH OTHER BY 20 DEGREES	78

FIGURE 3.19 FOUR FREQUENCIES APPLIED TO EACH ORIENTATION FOR GABOR FEATURE EXTRACTION	78
FIGURE 3.20 MEASURING PERIMETER OF A POLYGON WITH MINKOWSKI FUNCTIONALS.....	81
FIGURE 3.21 I) PIXEL NEIGHBOURHOOD OF 3X3, II) 4 TILES OF 2X2	83
FIGURE 3.22 THE SELECTED AREAS ON THE LOWER LOBE OF BOTH LONGS ARE DETECTED WITH HONEYCOMBING	84
FIGURE 3.23 HONEY COMBING ROI FORM A LOWER LOBE LEFT LUNG	85
FIGURE 3.24 BINARIZED VERSION OF A HONEYCOMBING ROI.....	85
FIGURE 3.25 COMPARISON OF CLASSIFICATION ACCURACY FOR DIFFERENT SETS OF FEATURES AND COMBINATION OF DIFFUSE LUNG DISEASE PATTERNS.....	98
FIGURE 4.1 THE LINE AND THE FIRST SQUARE ARE MADE UP OF SCALES EQUAL TO 3 AND THE LAST SQUARE'S SCALING FACTOR IS 2.5.....	103
FIGURE 4.2 KOCH'S SNOWFLAKES	103
FIGURE 4.3 A ROI IDENTIFIED WITH HONEY COMBING AND OTSU'S THRESHOLDING RANGES	106
FIGURE 4.4 IMAGE BINARIZATION BASED ON OTSU'S THRESHOLDS	107
FIGURE 4.5 SEGMENTED BORDERS ARE USED FOR FD CALCULATION BASED ON BOX COUNTING.....	107
FIGURE 4.6 DIVIDING THE NUMBER OF CONTAINED GRIDS RESULTS IN FD	109
FIGURE 4.7 HORIZONTAL (H:) AND VERTICAL (V:) FDSV RESULTS ON TWO PAIRS OF HONEYCOMBING, CONSOLIDATION, EMPHYSEMA AND GGO.....	110
FIGURE 4.8 CLASSIFICATION ACCURACY OF DIFFERENT NUMBER OF CLASSES BASED ON FRACTALS, ALL TEXTURES AND THE COMBINATION OF TEXTURE AND FRACTAL FEATURES	115
FIGURE 5.1. CORNER AND EDGE DETECTION BASED ON HARRIS DETECTOR	122
FIGURE 5.2. CORNERS DETECTED WITH HARRIS ALGORITHM (GREEN +).....	123
FIGURE 5.3. EVALUATION OF EDGE DETECTION USING CANNY, PREWITT AND ZERO- CROSSING ALGORITHMS	124

FIGURE 5.4. A CHEST CT IMAGE WITH GAUSSIAN FILTER APPLIED AT DIFFERENT SIGMA VALUES.....	125
FIGURE 5.5. EFFECT OF DIFFERENT FILTERS ON A CT IMAGE OF THE LUNG IDENTIFIED WITH CYSTS.....	126
FIGURE 5.6. EDGES TEND TO FADE AWAY WHILE SIGMA VALUE OF THE GAUSSIAN FILTER INCREASES	128
FIGURE 5.7. (A) SIGNAL REPRESENTATION AT DIFFERENT SCALES (B) ZERO-CROSSINGS OF THE SAME SIGNAL	129
FIGURE 5.8. ZERO CROSSING REPRESENTATION OF AN IMAGE WITH DIFFERENT SIGMA VALUES.....	129
FIGURE 5.9. RECTANGULAR REPRESENTATION OF SCALE-SPACE.....	130
FIGURE 5.10. THE SHADED RECTANGLES REPRESENT THE SMOOTHED SIGNAL	130
FIGURE 5.11. SCALE SPACE REPRESENTATION OF GAUSSIAN FILTER ON DIFFERENT OCTAVES AND DOG.....	132
FIGURE 5.12. FINDING POTENTIAL KEY-POINT ON THE BASIS OF LOWER AND UPPER SCALE COMPARISON	133
FIGURE 5.13. LOG OF THE SAME IMAGE AT DIFFERENT SCALES SHOWS HOW AN IMAGE GETS BLURRED BY PRESERVING THE SUB-STRUCTURE	133
FIGURE 5.14. TOP LEFT CORNER: REPRESENTS ORIGINAL IMAGE WITH SIGMA=0; TOP RIGHT CORNER: REPRESENTS GAUSSIAN OF THE ORIGINAL IMAGE WITH SIGMA 10; THE LAST IMAGE: REPRESENTS THE LOG OR DOG	135
FIGURE 5.15. POTENTIAL KEY POINTS BASED ON LOCAL MAXIMA (LEFT) AND KEY-POINTS (RIGHT) WITH RED +.....	137
FIGURE 5.16. WEIGHTED DIRECTION HISTOGRAM IN A KEY-POINT NEIGHBORHOOD	139
FIGURE 5.17. WEIGHTED DIRECTION HISTOGRAM IN A KEY-POINT NEIGHBORHOOD	139
FIGURE 5.18. MAXIMA (RED) & MINIMA (BLUE) INTERESTING KEY-POINTS AND THEIR DIRECTION (GREEN)	139
FIGURE 5.19 COMPARISON OF THE CLASSIFICATION ACCURACY OF THE COMBINATION OF FEATURES IN CHAPTERS 3, 4 AND 5 FOR DIFFERENT NUMBER OF CLASSES.....	146

FIGURE 6.1 THE 5-FOLD CROSS VALIDATION FOR CLASSIFICATION ASSESSMENT; EACH ROW REPRESENTS AN ITERATION. BLUE AREAS ARE THE TRAINING SETS AND ORANGE AREA IS THE TESTING SET	152
FIGURE 6.1. CLASSIFICATION ACCURACY OF TEXTURE FEATURES BASED ON 5-FOLD CROSS VALIDATION ON ANN.....	162
FIGURE 6.2. CLASSIFICATION ACCURACY OF ALL TEXTURE & FRACTAL FEATURES BASED ON ANN AND 5-FOLD CROSS VALIDATION	164
FIGURE 6.3. COMPARISON OF CLASSIFICATION ACCURACY OF ALL TEXTURE, FRACTAL AND SIFT FEATURES BASED ON 5-FOLD CROSS VALIDATION ON ANN.....	167
FIGURE 6.4. COMPARISON OF CLASSIFICATION ACCURACY OF ALL TEXTURE, FRACTAL AND SIFT FEATURES BASED ON 5-FOLD CROSS VALIDATION AND LEAVE-ONE-OUT METHODS ON ANN	170
FIGURE 7.1. COMPARISON OF CLASSIFICATION ACCURACY OF ALL TEXTURE, FRACTAL AND SIFT FEATURES BASED ON 5-FOLD CROSS VALIDATION AND LEAVE-ONE-OUT METHODS ON ANN	180

APPENDIX LIST OF FIGURES

FIGURE 1. CT IMAGE OF THE LUNG IDENTIFIED WITH CONSOLIDATION	186
FIGURE 2. CT IMAGE OF THE LUNG IDENTIFIED WITH PULMONARY CYST	186
FIGURE 3. CT IMAGE OF THE LUNG IDENTIFIED WITH PULMONARY EMPHYSEMA	187
FIGURE 4. CT IMAGE OF THE LUNG IDENTIFIED WITH PULMONARY FIBROSIS	188
FIGURE 5. CT IMAGE OF THE LUNG IDENTIFIED WITH GGO.....	188
FIGURE 6. CT IMAGE OF THE LUNG IDENTIFIED WITH HONEYCOMBING	189
FIGURE 7. CT IMAGE OF THE LUNG IDENTIFIED WITH PULMONARY NODULE	190
FIGURE 8. CT IMAGE OF THE LUNG IDENTIFIED WITH RETICULATION	191
FIGURE 9. CT IMAGE OF THE LUNG IDENTIFIED WITH SCAR	191
FIGURE 10. CT IMAGE OF THE LUNG IDENTIFIED WITH TREE-IN-BUD.....	192
FIGURE 11 SIGMOID TRANSFORM FUNCTION	196
FIGURE 12 AN EXAMPLE OF A NEURON	196
FIGURE 13 AN EXAMPLE OF 2X3X1 NN	197
FIGURE 14 SUPPORT VECTOR LINEAR CLASSIFICATION	202
FIGURE 15 K-NEAREST NEIGHBOUR CLASSIFIER	203

Achronyms

AMFM (adaptive multiple feature method)
ANN (Artificial neural networks)
BAC bronchioalveolar cell carcinomas
BMP (Microsoft Windows Bitmap)
CAD (Computer Aided Diagnosis)
CBIR (Content-Based Image Retrieval)
CE (contrast enhanced)
CLE (Centrilobular emphysema)
CT (Computed Tomography)
DBS (discontinuous breath sounds)
DFFT (Discrete Fast Furrier Transform)
DICOM (Digital Imaging and Communications in Medicine)
DLD (Diffuse of Lung Disease)
DPLDs (Diffuse parenchyme Lung disease)
DPLDs (diffuse parenchyme Lung disease)
DWF (discrete Wavelet Frames)
FD (Fractal dimension)
FPF (false-positive fractions)
GIF (Graphics Interchange Files)
GLCM (gray-level cooccurrence matrix)
GLDM (Gray Level Difference Method)
GLNU (Gray-level non-uniformity)
GLRLM (grey level run length matrix)
GLRLM (Grey level run length method)
GTSDM (Grey-tone spatial dependence matrices)
GTSDM (Grey-tone spatial dependence matrices)
HDF (Hierarchical Data Format)

HRCT (High Resolution CT)
HU (Hounsfield unit)
ILD (interstitial lung disease)
IP (interstitial pneumonia)
IPF (Idiopathic Pulmonary Fibrosis)
IPF (idiopathic pulmonary fibrosis)
JPEG (Joint Photographic Experts Group)
KBS (knowledge base system)
K-NN (k- Nearest neighbor)
LBP (Local binary patterns)
LF (Lung Field)
LOO (leave-one-out)
LP (lung parenchyma)
LRE (long run emphasis)
MDCTs (Multi-Detector CT scanners)
MDEE (multi-level dominant eigenvector estimate)
MLR (Multinomial logistic regression)
MRI (Magnetic Resonance Imaging)
NN (Neural Networks)
PBR (Pathology bearing regions)
PCA Principal Component Analysis
PCX (Paintbrush)
PFT (pulmonary function tests)
PLE (Panlobular emphysema)
PNG (Portable Network Graphics)
PNN (Probabilistic Neural Network)
PSE (Paraseptal emphysema)
ROI (Region of Interest)
RPC (run percentage)

RWF (rotated wavelet frames)
SARS (severe Acute Respiratory Syndrome)
SFTA (segmented based fractal texture analysis)
SMDC (selective marking and depth constrained)
SIFT Scale Invariant Feature Transform
SRE (short run emphasis)
SVM (support vector machine)
TB (tuberculosis)
TbTF (texture based transfer functions)
TIFF (Tagged Image File Format)
TPF (True-positive fraction)
UIL (Usual interstitial pneumonia)
UIP (Usual interstitial pneumonitis)
VO (volume overlap)

CHAPTER 1

INTRODUCTION

I. preface	2
II. Motivation	4
III. Problem Statement and Challenges	4
IV. Contributions	6
V. Limitations	8
VI. Thesis Structure	9

I. PREFACE

Diffuse Lung Disease (DLD), imputes to 15% of respiratory practice, accountable for a large class of disorders primarily affecting lung parenchyma⁶. As a part of the diagnostic procedure by the physician, a chest CT image is often essential, in addition to the physical examination and recording medical history. Usually, a radiologist with special interest in chest diseases is called upon to provide expert opinion about the CT image. The Appendix I provides a quick guide to a list of pathologies which are generally referred to as DLD. To diagnose these diseases, a radiologist goes through hundreds of images for each patient, in great detail. To assess progress of disease and therapeutic interventions, CT images recorded during successive visits are frequently compared. Such a task is often time consuming and vulnerable to significant inter-observer and intra-observer variability, even among expert radiologists.

Identifying diseases at an early stage is crucial, however, to visualize changes in CT images over successive visits is fraught with difficulties. The challenge lies in identification, localization and finding abnormal image patterns that are present. Different pathological causes can result in distinct diseases with specific treatments that follow. CT images cost less to produce compared to an MR generated images, and have long been the standard modality of lung parenchyma screening. However, the amount of X-ray dosage is required to be at its minimum in order not to exceed the limitations of X-ray exposure. Also during imaging, breathing adds motion artefacts and makes some images un-readable.

Such an important problem necessitates a computer aided system to reduce the inter-observer and intra-observer variability of diagnosis and bring the diagnostic accuracy of

general radiologists up to the level of expert radiologists. It is thus possible to provide high level knowledge with the help of a computer software during diagnosis, through enriched information provided to the expert radiologist.

To make an objective assessment of the image, the program needs to discern various radiological patterns due to pathologies as honey combing, ground glass opacity, various types of nodules, reticulations, emphysema and fibrosis. These abnormal patterns that manifest within the region of interest occur in various combinations with each other and sometimes with other diseases.

In order to develop a computer aided diagnostic (CAD) system, the software designer has to learn lung anatomy and the process of identifying DLD patterns under the tutelage of a trained radiologist. Next, appropriate image processing methods such as texture analysis, fractal dimension quantification have to be selected for their suitability and incorporated in the software design and development. The use of these methods in classification of lung diseases sets the path for incorporating relevant algorithms. The training and classification using artificial neural network (ANN) is performed in consultation with the expert radiologist who provides labelled sample patterns of various DLD pathologies. The radiologist's reading of these standard patterns is considered to be the gold standard, because of considerable years of experience and specialized knowledge.

In order to develop algorithm which yield highest possible classification accuracy performance, one has to try many algorithms and compare results for those features that would provide increased accuracy. While the literature reports many viable classification strategies, to our knowledge, no combination of texture and fractal analysis exists for

automatically classifying more than 6 pathologies identifiable from CT images of the lung. In order to overcome such a limitation, algorithms from face recognition field, namely scale invariant feature transform (SIFT) were identified to assist in developing powerful classification paradigms. Scale invariant feature transform (SIFT) is an interesting method with many applications in face recognition. Research reported in this thesis demonstrates that SIFT based features on their own and when combined with features from texture and fractal analysis, significantly enhance the performance of lung CT image classification.

II. MOTIVATION

Imaging of the body through various modalities such as CT, MDCT, PET and MRI have significantly contributed to the diagnostic capabilities of the physician by providing 2-D and 3-D rendering of body organs. The need for a specialist radiologist physician who can read images and quantify them with a high degree of accuracy is inevitable. Because of the large number of images produced from each patient through CT scans and MRI, abnormal image patterns that are only a few millimetres in span can be inadvertently missed by a radiologist due to the large volume of the work in a day and the ensuing fatigue. Thus, the necessity of finding pathological image patterns in a timely manner has defined the problem of identification and classification of DLD patterns in CT images of the lung through computer based algorithms and is the subject of present thesis.

III. PROBLEM STATEMENT AND CHALLENGES

The objective of this thesis is to develop and evaluate computational tools to assist the process of identification and classification of pathological image patterns from selected regions of interest in CT images in patients with DLD and compare them to normal healthy

lung tissue, with a high level of accuracy. Specifically, identification of image patterns from patients with lung diseases which include, consolidation, cyst, emphysema, fibrosis, ground glass opacity, honey combing, nodularity, reticulation, scar and tree-in-bud is the subject of this thesis. An artificial neural network is trained with quantitative feature vectors from labelled image data in order to assign each ROI under consideration to a specific disease class. Figure 1.1 demonstrates the ten sample images from patients with DLD and which are analysed in this thesis. Appendix I provides detailed description of each disease and a larger view of each ROI in a CT image of the lung.

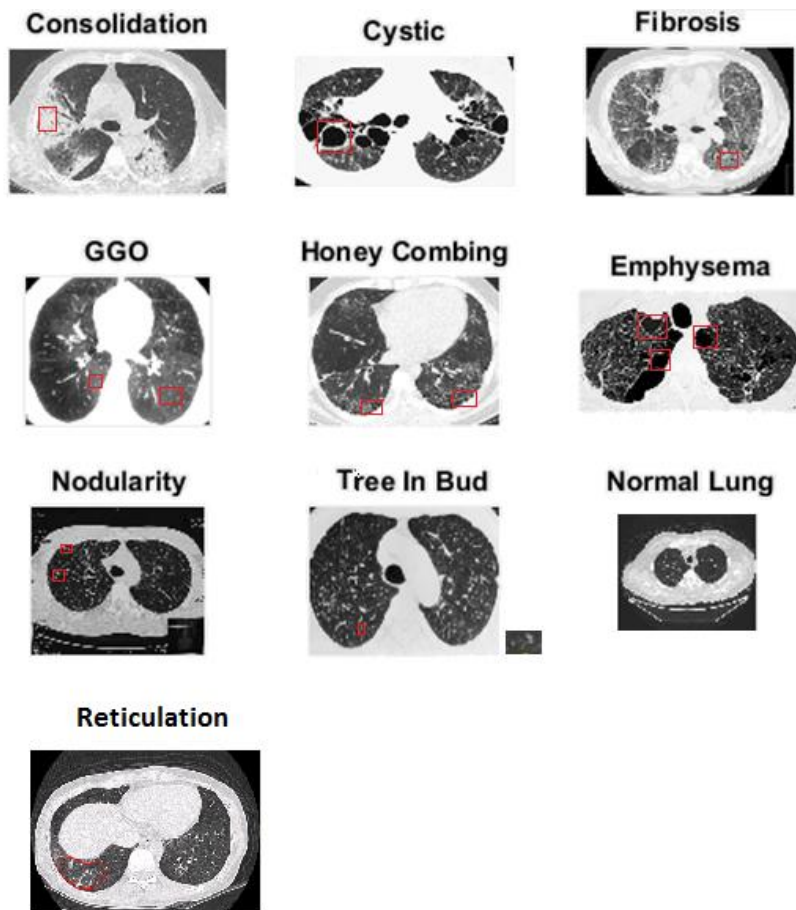


Figure 1.1 Images of ten pathological DLD patterns and of a healthy lung

There are several hurdles one has to overcome to achieve above objectives. One has to have continuous and unstinted support from a radiologist who agrees to lend his/her time and expertise. Acquiring image data sets for each disease class and identifying thousands of ROI's to train the ANN based classifier, requires considerable amount of time. One cannot record high resolution images without motion artifacts or noise in a real world image setting. Although MRI has advanced in recent years in visualizing lung parenchyma, only images recorded in a CT scanner were available for this research. Analytical methods that can characterize images generated by patients with DLD lung pathologies, with a high level of confidence and high specificity is challenging. To train an ANN based on limited number of images requires features which quantitate images with high level of specificity. With texture and fractal methodologies which are the most commonly used approaches in the literature, classification accuracy in our study did not exceed those achieved by other laboratories. Detecting image quantification in fields other than medical imaging that could relate with the problem was cumbersome. Another aspect of this work was the expectation that software had to interactively analyze DICOM images, extract features from each DLD pattern, train an ANN and classify a ROI with a high level accuracy.

IV. CONTRIBUTIONS

The research in this thesis has attempted to identify and employ innovative computational algorithms for classifying regions of interest derived from CT images with diffuse lung disease patterns. A large number of texture analytic algorithms and quantitative indices from fractal analysis have been invoked to obtain a broad range of comprehensive features. In addition, a scale invariant feature transform (SIFT) has been employed to obtain unique

features from the regions of interest in lung CT images in order to enhance the machine learning and pattern classification. The combination of texture, fractal and SIFT features were introduced for the first time in this research. Such a broad combination features, integrates information from several characteristic aspects of features, including: texture, morphology, localization, and quantitative descriptors which some are invariant to illumination, noise and scale.

Classification accuracies for different combination of pathologies and different number of classes are assessed based on leave-one-out and 5-fold cross validation methods. Classification results based on 5-fold increases from 68% for eleven classes using SIFT to 85% when using all SIFT, texture and fractal features. The classification accuracies are higher with leave-one-out method. Classification accuracy based on SIFT generates over 99% accuracy up to four classes and more than 71% for up to eleven classes on ANN. Classification accuracies are higher when these features are combined with features generated by texture and fractal analysis.

Many textural, fractal and SIFT based features that can characterise DLD patterns with the least information overlap as possible, have been assembled in this thesis work.

Classification results based on 11 patterns has not been reported in the literature. Therefore a CAD system which can classify and separate regions of interest selected from CT images recorded from as many as 10 diseases and healthy ROI's, is an attractive research proposition and has served as the primary motivation for the work reported in this thesis.

In the present research, blinded data was not available and therefore, two validation techniques were incorporated; namely, the leave-one-out and 5-fold cross validation procedure for testing various classification results.

Trained artificial neural network based on different combination of texture, fractal and SIFT features on 10 types of DLD's and healthy ROI's are described in the thesis.

V. LIMITATIONS

There are a number of challenges associated with such an undertaking. On one hand, a computer scientist faces the challenge of acquiring relevant data which is often confidential, it also requires a radiology specialist to devote considerable amount of time in narrowing down many images which are highly indicative of pathologies of the lung. Some regions of interest may have several abnormalities which will not result in a clean feature extraction and classification. On the other hand in order to write good software, the computer scientist must familiarize himself/herself with a new field of study and understand the pathophysiology of several diseases so as to be able to identify and characterize patterns associated with specific diseases. The major limitations of this research are:

1. Lack of blinded image data set for a thorough validation of extracted features and the assessment of classification results.
2. High resolution CT images requires more X-ray dosage. However, for patient's safety, only a certain dosage, which is assessed by the specialist is incorporated. Additionally, motion artifacts based on patient's movement and breathing defects images. Therefore, the classifier in this research could not be trained based on a perfect set of images.

3. Extracting regions of interest is time consuming, especially if one is interested in ROI's which represents a specific disease/pattern. Many extracted ROI's in this research have multiple diseases which will make it more difficult for any pattern recognition method and classifier to perform at its best.

VI. THESIS STRUCTURE

Research described in the present dissertation employs texture, fractal dimension and scale invariant feature transform methods for extracting quantitative features from CT images of the lung. An artificial neural network is used for training and classification purposes. In addition, features derived from SIFT algorithm by itself have been used in the present work. The chapter 2, which was a part of the research proposal submitted to Computer Science department at McMaster University, reviews texture analysis methods applied for classifying most commonly occurring DLD patterns. A version of the chapter 2 was submitted and accepted by Critical Reviews in Biomedical Engineering¹⁴⁶ on October 1st, 2015. Chapter 3 describes the application of Tamura, Haralick, Minkowski Functionals and GLCM methods to classify DLD patterns in CT images. An artificial neural network (ANN) based on backpropagation was used for the research described in this thesis. Fractal dimension analysis and their application in classification of diffuse lung diseases is detailed on chapter 4. The issue, whether features derived from fractal analysis on its own or in combination of texture analysis enhances the accuracy, is also examined in chapter 4. Chapter 5 introduces the application of SIFT analysis to CT images of the lung and describes the results of classifying ROIs from pathologies commonly termed as DLD, step by step. Different combinations of features developed in chapters 2, 3 and 4 are combined

with features generated by SIFT, to provide classifiers with high specificity that can assist a diagnostic radiologist in clinical decision making. Partial results and the application of SIFT descriptors on DLD patterns were published by Mehrdad Alemzadeh, Dr. Colm Boylan and Markad V. Kamath at Biomedical Engineering Society's conference held in Tampa, Florida, in October 2015. Classification results are based on leave-one-out method, which is useful for testing the accuracy of classifier. Chapter 6 provides classification accuracies based on 5-fold cross validation and compares the results for every feature extraction method and their combinations. Finally, chapter 7 provides conclusions and suggests for potential future research.

CHAPTER 2

A REVIEW OF TEXTURE QUANTIFICATION OF CT IMAGES FOR CLASSIFICATION OF LUNG DISEASES

I. Introduction.....	12
II. Texture Analysis.....	13
A. Feature Extraction.....	14
1. Structural Methods.....	15
2. Statistical Methods.....	15
3. Model Based Methods.....	19
III. Segmentation.....	24
A. Texture Based Segmentation.....	24
IV. Classification.....	28
V. Fractal Texture Analysis.....	29
VI. Applications of Texture analysis toward diagnosis Using CT images of the lung in diagnosis of DLD.....	31
A. Identification of Abnormal Image segments.....	32
1. Emphysema.....	40
2. Cancer.....	42
VII. Application of Scale Invariant Feature Transform in CT Images of The Lung.....	45
VIII. Assessment.....	48
IX. Discussion.....	49
X. Chapter Summary.....	50

I. INTRODUCTION

Radiologists evaluate thousands of medical images every day and are expected to deliver diagnosis in many patients with a high level of accuracy and reliability. However, due to continuous reading of diagnostic images, they are vulnerable to errors, especially due to fatigue. Overlooking even a minor abnormality can sometimes result in wrong diagnosis. Computer aided diagnostic systems are promising tools that assist a radiologist in identifying abnormal radiological patterns and therefore, can be of assistance in increasing the accuracy of diagnosis and reduce the time required for preparing an expert report on each image. Towards this end, a number of laboratories have developed methodologies and mathematical algorithms which can assist the physician during diagnosis of images in a hospital environment.

Images acquired through Computer Tomography (CT) of the lung have been generally accepted as the gold standard for diagnosing diseases of the lung. Lungs are filled with air and therefore, ribs can be easily eliminated in a CT image. The rest of the image are the parenchyma and the lung tree, which provide clear contrast from the background and will be the aim of CAD systems analysis. Following image acquisition, the CT scanner generates images which can be translated to different image formats such as DICOM, TIF and JPG. A review of literature on texture analysis of certain salient parts of CT images of the lung combined with segmentation and classification of abnormalities is the primary focus of this chapter. Relevant work on scale invariant feature transform (SIFT) is also included. Certain parts of this chapter have been published in Critical Reviews in

Biomedical Engineering Journal under the title “A Review of Texture Quantification of CT images for classification of Lung Diseases¹⁴⁶”.

II. TEXTURE ANALYSIS

Texture analysis of an image is concerned with the study of the variations in the intensity of pixel values¹ extracted from a ROI. Cambridge advanced learner's dictionary describes texture as a surface that is not smooth but has a raised pattern on it. And a computing dictionary refers to it as a measure of the variation of the intensity of a surface, quantifying properties such as smoothness, coarseness and regularity². In biomedical images, which are viewed in a two dimensional format, an altered quantified texture can adequately identify certain kinds of pathologies. Although many lung diseases alter the tissue density, resulting in intensity changes in the CT image data, segmentation based only on intensity alone, will not provide acceptable levels of accuracy.

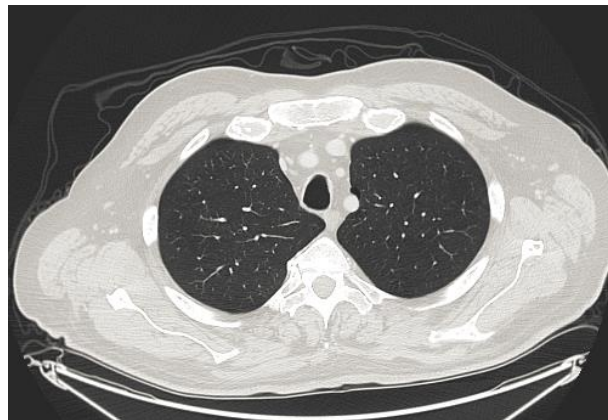


Figure 2.1 Normal lung

Specifically, research has demonstrated the significant potential of texture analysis in identifying diseases of the lung by extracting texture based features and use them as an input to a pattern classifier. Applications of texture analysis to certain regions of interest in

medical imaging can be followed by segmentation, classification³ and synthesis of other relevant information by an experienced physician. In image segmentation, boundaries and regions that have significantly differing properties are identified. The goal of pattern classification is to categorize images based on their quantitative descriptors called features, into different pathologies. Synthesizing images is useful in 3-D applications when the surface needs to be visualized more realistically. Texture analysis methods use statistical, geometrical, model based and signal processing approaches towards quantifying specific characteristics of an image⁵⁻⁴.

A. FEATURE EXTRACTION

In general, the process of segmentation consists of identifying a particular region of interest, usually by the physician. Feature extraction based on texture analysis of images followed by pattern recognition are applied subsequently to classify the regions of interest⁴. However, a common limitation is that the information contained in different features may overlap and is correlated. Reducing the number of features based on their relevance and correlation can reduce the dimensionality of the feature vector and could lead to an increase in the accuracy of classification. There are several linear and non-linear feature reduction techniques which make classification and machine learning efficient. Image classification methods based on Artificial Neural Networks (ANN), k-nearest neighbor (K-NN) and Support Vector Machine (SVM) have also been developed to distinguish between different types of complex pathologies⁶.

These classifiers are trained based on extracted features from labeled data and the class (identified by the radiologist) they belong to. Subsequently, the feature set developed using the labeled classifier can be used to categorize an image with unknown diagnosis.

Texture extraction methods will be discussed in the next section. These include structural methods, statistical methods (First-Order, second-order and higher-order statistical Texture features), and model based methods, transform domain methods (Fourier Transform, Gabor Filters, Multi-resolution).

1. Structural Methods

A structural model, presumes that texture primitives have different textures. The texture is created based on the placement of these primitives. Structural methods are suitable for regular textures. In this kind of analysis, the texture elements are extracted first and then one deduces placement rules. Usually elements are defined to be regions with different grey levels and there are algorithms for extracting them from an image⁵. If we are developing a symbolic description of the image or texture analysis, structural methods are very useful. There is a large variability within the micro texture and the macro texture in natural images. It has been shown that structural methods would not be helpful in quantification of medical images because the distinction between micro and macro textures will not be adequate to carry out segmentation⁷.

2. Statistical Methods

In this section, we present a succinct description of statistical methods. While performing texture analysis, we assume that the surface of the image is a two dimensional representation of a three dimensional object, in this case, the lung. Texture defines a 3-

dimensional surface and textural boundary detection is a distinct capability of human's eye which is why 2-D texture segmentation is an outgrowth of surface discrimination in 3-D.

There are three main classes of statistical methods for texture analysis. First-order statistics such as the mean, calculate the probability of measuring a certain grey level value at a location within the image. First order statistic(s) of an image or a region within an image do not take into account either correlation and/or co-occurrence between pixels. Usual statistics that are used include mean, variance, coarseness, skewness, kurtosis, energy and entropy. Second-order statistics play an important role in separating two images based on their textural features⁴. Second-order statistics measures the probability of the presence of a pair of grey level values of random length and orientation. Higher order statistics increase the number of parameters to be measured and also contribute information for discriminating disorders of the parenchyma⁸.

Certain textural features can be computed from a grey level dependency matrix, also called a co-occurrence matrix. Such a matrix has a dimension $N \times N$ where N is number of grey levels. In an image where co-occurrence matrix is used as an element for measuring texture, the probability distribution is far from the diagonal⁹. A 3-D co-occurrence matrix has similar characteristics, but it assumes the comparison of intensities in 13 different directions of a VOI¹⁰. Textures within an image can differ by order/disorder, regularity/irregularity, and roughness/smoothness and so on. Textural patterns are presented as feature vectors of properties which characterize a point in multi-dimensional feature space. One of the goals of a classifier is to find a decision rule that categorizes each textural pattern to a particular class⁹.

a. First-Order Statistical Texture Analysis

This analysis uses image histograms (or occurrence probability) and simply uses standard descriptions such as mean and variance to characterize pixel data. Since this method does not take spatial relation and correlation of pixels into consideration, its usability is limited. Gray level has a range of $0 \leq i \leq N_g - 1$ (N_g : number of gray levels). The histogram or pixel occurrence probability is calculated as:

$$P(i) = \frac{N(i)}{M}$$

Where $N(i)$ is the number of pixels with intensity I and M is the number of image pixels. Properties of the histogram that analyzes texture are: mean, variance, coarseness, skewness, kurtosis, energy, and entropy⁴.

b. Second-Order Statistical Texture Analysis

In the second order statistical texture analysis, a co-occurrence matrix or GTSDM (Grey-Tone Spatial Dependence Matrix) is computed. The entries to this matrix are based on the probability of finding a pixel that has grey level i with a distance and angle of d and α respectively from a grey level j (formally $P(i, j; d, \alpha)$). There will be a need to describe the texture content of GTSDM in four directions (Figure 2.2; horizontal, vertical, left-diagonal and right-diagonal) because each pixel has eight neighbors connected to it⁴.

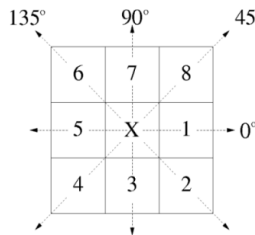


Figure 2.2: Four directions and its eight neighboring pixels

If the co-occurrence matrix is calculated in all four directions, we can construct a complete textural representation of the image. Haralick⁴ suggested that we can extract information from these matrixes using texture features which are sensitive to particular elements of texture. He then proposed fourteen textural features based on particular characteristics describing the texture. Certain features may be correlated and would not provide discriminatory information for subsequent classification. So feature selection algorithms are very useful for reducing the redundancy between features⁴.

The grey level difference method (GLDM) is another technique based on the co-occurrence of grey level vales and their absolute difference in a particular distance and direction. This will be a histogram and its size is equal to the number of grey levels in the region of interest. Normalized histogram $H(k|d,\theta)$, calculates the probability of occurrence of grey level with value k between two pixels at a specific distance d at direction θ . These formulas are explained in greater detail by Vasconcelos et al.⁹

c. Higher-Order Statistical Texture Analysis

Grey level run length method (GLRLM) is an approach that carries information on the grey level run/range (run length is number of pixels on the run) in a specific direction used in higher order statistics of textural analysis. For instance coarse textures will have long run while a fine texture will have a short one. The inputs for this matrix is calculated by

$$R(\alpha) = [r'(i, j|\alpha)]$$

Where r' is the number of runs is, i is the grey level (range), j is the run length and α is the direction. The directions are defined like GTSDM⁴.

Galloway has identified five run-length features, where a run is a sequence of pixels which have the same gray level intensity along a planar orientation¹¹. These features focus on following aspects of pixel intensities⁹:

1. Short Run Emphasis that measures the most important short primitives in a textural design,
2. Long Run Emphasis measures look for long runs. Gray-level non-uniformity measures the gray level characterization of the primitives,
- 3, Run-length non-uniformity measures the similarity of the length of runs through the CT image.
4. Run Percentage measures the homogeneity and,
5. Distribution of runs, the largest value is obtained when all the primitives have a length of one.

Run length serves as a statistical measure for defining coarseness of texture in a particular direction.

3. Model Based Methods

Model based methods use mathematical models as the basis for describing an image with regards to its texture and synthesis. The quality of texture is analyzed based on the parameters of its model⁵. Markov and Fractal models can be used for describing texture and synthesizing it. They describe an image as a probability model or as a liner combination of a set of functions⁷.

A model based method can analyze the texture and even synthesize it based on fractal or Markov modeling. With these methods we obtain the probability model of an image as a

set of linear functions. Fractal¹² analysis is used for modeling natural images to analyze textures that contain statistical behaviors such as roughness at different scales. Finding the orientation based on fractal analysis is not an easy task and is the main weakness of such model based methods⁷.

Pixel based modeling examines an image based on its pixels, while region based models analyze images based on different patterns and arrangements of pixels. There are many modeling techniques based on neighboring pixels and noise orientation. For example, random field models can delineate spatial changes based on global random and local random models. Global random models characterize the entire image based as a realization of random field and local random models take into account relationships between different intensities in a field of view⁷. Markov models are local random field models wherein conditional probability of the intensity of a pixel is dependent of the intensity of pixels in the neighbourhood.

4. Transform Domain Methods

Transform domain methods such as Fourier, Gabor and wavelet transform the image to highlight textural properties in a different domain. In practice, most image transforms use filters and similar algorithms to compute the energy within an image. Transfer functions can be combined with texture analysis to differentiate structures and features that have the same intensity. Caban et al. have suggested a direct volume rendering with this strategy¹³. For instance, if the intensity values of blood vessels and lung boundaries are the same, they will be colored differently due to their differing textures. Identifying objects in volumetric data is difficult but using direct volume rendering has potential benefits. However, transfer

functions that map densities to specific colors provide an acceptable visual representation of 3-D data¹³.

a. Fourier Transformation

Currently, most of the transforms that are being used in biomedical imaging applications are in 2-D. They are useful in image description and enhancement. Fourier transform is a well-known computational procedure that can be used to study coarseness or fineness and directionality of textured surfaces. Ring and wedge filters can extract textural properties from a Fourier transform of the image. Rings can have different sizes based on their application but the coarseness or fineness can be measured between rings of inner radius r_1 and r_2 . We can measure the average power of wedge shaped regions which are centered at the power spectrum to find directionality of textures. The size of wedge also varies between different applications ($\phi_w = \phi_1 - \phi_2$).

Power spectrum $P(u, v)$ is calculated from a discrete Fourier transform $F(u, v)$ in image processing

$$P(u, v) = |F(u, v)|^2.$$

b. Gabor Filter and Gabor Transform

Gabor Filter is a linear filter that has been found useful in classification, texture segmentation image recognition and edge detection. The Gabor Filter is a well-established technique for feature extraction from 2D images in texture analysis too. The formula for this filter is⁷

$$g(x, y; \lambda, \theta, \phi, \delta, \gamma) = \exp\left(-\frac{x'^2 + \gamma^2 y'^2}{2\sigma^2}\right) \cos\left(\frac{2\pi x'}{\lambda} + \phi\right)$$

where $x' = x \cos\theta + y \sin\theta$, and $y' = -x \sin\theta + y \cos\theta$.

where λ represents the wavelength of the cosine, θ is the orientation, ϕ is the phase offset, δ is the sigma of the Gaussian envelope, and γ is the spatial aspect ratio. The Gabor features are calculated as shown in the equation below and (x, y) is the spatial coordinate, f is frequency, and θ represents the orientation⁷:

$$r_{\xi}(x, y; f, \theta) = \Psi(x, y; f, \theta) * \xi(x, y) = \int \int \xi(x - x_T, y - y_T; f, \theta) \xi(x_T, y_T) dx_T dy_T.$$

Determining the window size and the number of channels at the same frequency in Gabor filtering is the primary draw back in its application for extracting texture features.

Windowed Fourier transform also known as short-time Fourier Transform of a one-dimensional signal $f(x)$ is defined as:

$$F_w(u, \xi) = \int_{-\infty}^{\infty} f(x) w(x - \xi) e^{-j2\pi ux} dx$$

When the window function $w(x)$ is Gaussian, the transform becomes a Gabor transform⁵.

The Gabor transform has some difficulties with texture analysis such as discriminating between edges and texture. It has been observed that Wavelet transform has more advantages in textural studies⁷. Wavelet transform allows a better texture representation based on a proper scale with a varying spatial resolution. Since there are many different wavelet functions, the choice of the wavelet function is determined by the nature of texture analysis and its application⁷.

5. Multi-resolution Method

Multi-resolution technique is a multiple channel analysis method that has been tuned with different frequencies. The methods of feature selection from rings and wedges are

analogous to this method, with the difference of information phase retained in multiresolution method⁵. The multi-resolution method retains the information of the image, based on different levels of resolution and blurring. The texture structure is therefore preserved with this method. This method is carried out in the following two steps: extracting the most discriminating texture feature of the region and then classification of various tissues⁷.

a. Wavelet Based Method

When a function $f(at)$ is scaled over time (t), the function is concentrated if $a > 1$ or expanded when $a < 1$; we can formulate the wavelet transform as follows:

$$W_{f,a}(u, \xi) = \frac{1}{\sqrt{a}} \int_{-\infty}^{+\infty} f(t) h * \frac{t - \xi}{a} dt$$

The scale of a is based on frequency of the filter and we can create a wavelet model for texture analysis.

b. Ridgelet Based Method

This transformation acquires information in multiple directions which includes: vertical, horizontal and diagonal radial directions of frequency domain. Studies show that first order statistics can be applied for classification of texture by applying 1-D wavelet transform. Ridge based method has been used in images acquired during computed tomography⁷.

c. Discrete Wavelet Transforms

Discrete wavelet framework is a variation of DWT which is explicitly refined for texture characterization of an image. This method provides rich information about the boundaries of a region using parameters of texture analysis. The mean of texture features are applied

to NXN regions and features are extracted from region. The limitation of DWT method is that, when the region is relatively small it cannot adequately describe texture features of that region. To improve segmentation, higher dimensional feature space can be used by extending spatial feature space using mean shift algorithm⁷. Calculating median values of energy in the region of interest at the corresponding filter bank can be used for texture characterization. It is important to retain the total energy that characterizes texture in between regions, and that can be achieved by using median filters⁷.

III. SEGMENTATION

The segmentation process partitions an image into classes or subsets that are homogeneous with respect to one or more characteristics or features¹⁴. Following segmentation, measurements, and image display may be undertaken¹⁵.

A. Texture Based Segmentation

Textural properties provide discriminatory information for segmentation of images based on certain properties¹⁶. One of the problems in segmenting lung lobes in CT is to identify fissure regions. The lobar fissure which is a long narrow opening in the form of a crack, is difficult to identify due to its variable shape. Using gray level co-occurrence matrix (GLCM) and grey level run length matrix (GLRLM)¹⁷ as features, identification of the lobar fissure has been achieved in CT images of lung, with accuracies as high as 86% and 87% respectively. For example, accurate segmentation of the lung field in CT images on volumetric data is challenging due to lung border differences and the presence of pathology. Studies have shown that 3-D lung field (LF) segmentation which is adapted to interstitial lung diseases can be successful¹⁸. In their research, Korfiatis et al. use K-means clustering

technique to obtain an initial order estimate on the LF. Final analysis of the borders is based on iterative SVM¹⁹ (support vector machine) labeling of 3-D texture features can classify abnormalities in the lung¹⁸. The Table I lists research publications from laboratories which have used textural properties to perform segmentation of lung images recorded during CT scans.

A classification system developed by Singh et al. annotates and indexes specific regions of an image as soon as it is registered into the system²⁰. At first the lung image is partitioned into homogeneous regions. Then the segmented regions are annotated using a knowledge base system (KBS). The KBS contains pattern signatures created by machine learning and heuristic rules acquired from domain experts. The system consists of three main components. The first component deals with the extraction of visual features for segmentation and classification. The second component consists of an unsupervised segmentation technique to extract features for partitioning the image into homogeneous regions. Finally, a segmented region is classified using a knowledge base system (KBS). The KBS captures signatures and heuristic knowledge incrementally from machine learning and the domain expert.

The Table 1.1 summarizes some recent reports on segmentation in lungs.

Area	Disease	Algorithm	Results
Extract pulmonary parenchyma from multi sliced CT ²¹	Pulmonary diseases such as lung cancer, tumor, and mass cells	Improved 2D Otsu based on swarm optimization Employs line-encoded methodology and uses contour tracing method	Decreased the processing time from 90 seconds to less than 1 second per slice
Lung tissue ¹⁵	Tested on fifteen 3-D CT data with lung diseases	Graph search driven by a cost function combining the intensity, gradient, boundary smoothness, and the rib information	The results are compared with manual assessments
Parenchyma ²²	Pulmonary diseases	Optimal threshold value and the boundary tracking method for background elimination. Mathematical morphology method for boundary repairing	Automatic and accurate segmentation of lung regions
Morphological changes of the lung ²³	Airway diseases	Principal curvatures and directions. Puzzle game algorithm for false positive detection.	Segmented the 3-D human airway tree. Partial volume effects are alleviated; no leakages.
Pulmonary parenchyma ²⁴	Cancer	Extract pulmonary parenchyma and use FCM to segment patients with lung cancer	Improved diagnostic accuracy of lung cancer
Structure and shape of airways in lungs ²⁵	Airways	Edge-detecting slice-by-slice method & projections method	Accurately segmented to the 6th bifurcation

Lung tissues ²⁶	Cancer	Employs a combination of EM algorithm and morphological operations vs. level sets and energy optimization by Graph Cuts technique	Maintaining the details of the nodules & boundary regions in the chest cavity does it segment?
Lung lobe ²⁷	analysis of pulmonary functions	A linear structure filter based on the Hessian enhancing lung fissures. By Canny operator, ridge of the image is extracted. Uniform Cost Method to the detection of ridge of the fissures.	Detects and locates lung fissures.
Estimation of the volume of lungs & viable lung tissue ²⁸	Severe pulmonary disease	Pre-computed compact regions with homogeneous texture combined with a classifier	Can be used to segment lungs in scans in which automatic segmentation methods fail
Pulmonary lobes ²⁹	parenchymal disease	Based on a multi-atlas approach. A cost function is used to obtain information when most reliable information is not available.	It is robust against incomplete fissures
Airway tree ³⁰	Diagnosing disorders of the lung	Region growing, 3D wave propagation and morphological refinement to segment bronchi.	Successfully segmented up to the 6 th generation in 2Sec/airway tree
Lung tissue ³¹	Cancer	active contouring for lung tumor segmentation in 3D-CT on a cluster function	Defining the gross tumor volume for irradiation in cancer therapy

Pulmonary parenchyma ³²	Pulmonary nodule detection	Adaptive threshold, connected regional Labeling and morphological operations	Average segmentation accuracy = 91.55%
Vessel tree structures ³³	ILD	A 3-D multi-scale vessel enhancement filter based on Eigen value. texture-based voxel classification for possible over-segmentation	Evaluation by means of area overlap demonstrated a statistically significantly ($p < 0.05$) high performance
Lung tissue adhesion ³⁴	Lung volume segmentation,	Is based on the classical watershed algorithm. Employs line-encoded methodology and uses contour tracing method	More continuous boundary after segmentation and minimal Cross-segmentation. Prevents over segmentation.
Lung ³⁵		Combined complex-valued artificial neural network	The accuracy of this algorithm is better than ANN

Table 1.1 Segmentation algorithms in identifying diseases in the lung

IV. CLASSIFICATION

Classification of images and image segmentation can be based on a number of algorithms, once features which have significant discriminatory properties have been extracted. Researchers have examined quantitative texture measures to determine potential features and then evaluate them through different metrics based on similarity or dissimilarity analysis³⁶. CT images are very rich in terms of their texture which explains why its analysis has found its place in image classification for diagnosis⁹.

We can categorize image(s) based on its different texture patterns and use learning algorithms to help classify those images³⁷. During classification, each image is assigned to

a class that is most similar in some sense, in this case based on features derived such as texture analysis, SIFT and fractals.

V. FRACTAL TEXTURE ANALYSIS

The idea of describing the real world by well-defined mathematical constructs such as cubes, spheres etc. is conceptually difficult, especially when one encounters objects of complex shapes. The main idea behind fractals is based on self-similarity over a range of scales, meaning that an object can be decomposed into smaller pieces which are self-similar (i.e. similar to itself) and have fractional dimensions. The concept of self-similarity and associated mathematical descriptors introduced by Dr. Benoit Mandelbrot have also been used to describe the degree of irregularity of a surface (texture) in biomedical imaging⁴. Irregular or rougher structures would likely to have a fractal dimension. There are two categories of fractal analysis: deterministic (self-similar) and random (or non-deterministic). Objects that do not change their appearance in different magnitudes and stay consistent (exactly self-similar) are called deterministic fractals but if they show subtle changes, they are called non-deterministic.

Fractals can be defined formally as a geometrical set whose Hausdorff–Besicovitch dimension strictly exceeds the topological dimension. There are many biological and natural structures that have discontinuities and fragmentation so they can also have a fractal dimension. These types of features rarely have an exact Euclidean shape, meaning that they are not usually smooth. Therefore, by using FD we can have a precise measurement of the dimension of the image segment¹. Fractal dimension is a numerical description of disordered objects which is close to the description of Euclidean geometry but it has the

capability to quantify objects in non-integer dimensions. When the object is sophisticated it will have a higher fractal dimension⁴. There are different methods to study fractal dimensions such as box-counting for random structures or Korcak method which treats the input as a textured surface⁴.

The FD of an image segment can provide a measure of its texture complexity¹. For instance, the pixel intensities within an image can be thought of an elevated plane and the intensity at any point on the surface is thought to be a rugged surface. The relationship between fractal dimension and Euclidean has been compared to that between digital and fuzzy logic, where FD is a value which lies between two integer dimensions. Thus, the FD can provide us with a numeric information about the surface. Computation of the FD is based on following concepts.

In a Euclidean space n we can account for a bounded set S to be similar to itself in the condition for this set to be the union of N_r (number of self-similar or invariant shapes) non-overlapping subsets, with r being the scaling factor, which has the relation $r(S_n)$ for N_r and S_n to be congruent sets in distribution to S . Therefore, fractal dimension is a real number which is a bounded in the set R^n and it describes the geometric complexity of S as if Euclidean space uses length for measurement¹.

We can compute FD as follows¹:

$$FD = \frac{\log(N_r)}{\log\left(\frac{1}{r}\right)}$$

We can deal with fractals in a statistical manner because most of natural fractals are random. For instance blood vessels branching in lungs are random fractals but are not

completely self-similar. In its formal description FD of a structure has to have self-similar non-changeable fragments and irregular shapes in every scale up to infinity. Based on the depth of images in biological structures FD can only be scaled finitely which means, scales above or below will be either Euclidean or random (rough and non-similar).

The relationship between fractals and texture of an image has come under scrutiny. For example, even if FD value of both images are the same, their texture characteristics can be different¹³. Lacunarity of the FD texture is a measure of how a fractal filling space; in other words, the higher lacunarity is, the more inhomogeneous the image can be. Dense fractals have low lacunarity and the coarser a fractal is, the higher its lacunarity. This is defined in terms of the ratio of the variance over the mean value of the function,

$$L = \frac{\frac{1}{MN} \sum_{m=0}^{M-1} \sum_{n=0}^{N-1} I(m, n)^2}{\left(\frac{1}{MN} \sum_{k=0}^{M-1} \sum_{l=0}^{N-1} I(k, l) \right)^2} - 1.$$

Where M and N are the sizes of the FD processed image.

Al-Kadi and Watson have successfully combined fractal dimension and lacunarity to differentiate between aggressive and nonaggressive malignant lung tumors¹.

VI. APPLICATIONS OF TEXTURE ANALYSIS TOWARD DIAGNOSIS USING CT

IMAGES OF THE LUNG IN DIAGNOSIS OF DLD

Quantitative texture analysis of lung has permitted classification and identification of diseases such as pulmonary fibrosis, normal/abnormal lungs, SARS, DLD, reticulation, emphysema, honey combing and parenchyma disorders.

Examples of various techniques described for identifying some of the above abnormal image segments are presented below. These are followed by usefulness of texture analysis in diagnosis of lung diseases based on CT image analysis.

A. Identification of Abnormal Image segments

Sutton and Hall were the first to recognize the significance of computer analysis for interpreting chest radiographs as early as 1973. They used texture analysis to generate features and pattern classification methods to automatically distinguish between normal and abnormal lung tissues in patients with pulmonary fibrosis⁶.

Park et al. extracted the lung field with power spectrum and Quasi Gabor filter and used a 2D-DFFT (Discrete Fast Fourier Transform) to overcome the problem of ribs and vessel shadows of lung. They report a novel method called score-block operation that is combined with K-nearest neighbor method classifier to identify normal and abnormal lung areas. Their method can make padding of the border and quantification easier³⁸.

Detecting abnormalities in chest radiographs by diffuse texture was devised by Van Ginneken et al³⁹. They found the overlapping areas of different sizes by segmentation. Texture features are extracted and the difference between the left and right lung is used for additional information. A weighted multiplier is used on K-nearest classifier which gave a higher score to regions and with an increased classification reliability. Tang et al.⁴⁰ studied severe Acute Respiratory Syndrome (SARS) to distinguish SARS infected regions of CT images from normal lung using co-occurrence matrix as texture features. Since regions infected by SARS are irregular, texture analysis is very helpful in identifying those regions. Tang et al. developed a multi-level dominant eigenvector estimate (MDEE) to approximate

Principal Component Analysis (PCA), to overcome the problem of large dimensionality of the co-occurrence matrix⁴⁰.

Tolouee et al⁴¹ proposed a novel approach using two sets of wavelet filters: discrete wavelet frames (DWF) and rotated wavelet frames (RWF). They used these frames to extract features and lung tissue patterns. Four different lung patterns (ground glass, honey combing, reticulation, and normal) were selected from a database of 340 images are classified using support vector machine (SVM). They reported that the best results are obtained by a combination of the two filter banks, suggesting to use them together to provide information which shows a complementary benefit.

Diffuse lung disease (DLD) accounts for fifteen percent of respiratory diseases. The DLD can lead to respiratory failure and affects the surface of parenchyma which can be identified with texture analysis methods.

In a research paper by Korfiatis et al¹⁰, MDCT identified interstitial pneumonia (IP) for a gray level thresholding combined with an edge-highlighting wavelet preprocessing step, followed by a texture-based border refinement. Identification and characterization of IP patterns is formulated as a three-class pattern classification of LP into normal, ground glass, and reticular patterns, by means of k -nearest neighbor classification. Figure 2.3 demonstrates ground glass opacity and traction bronchiectasis on a CT image.

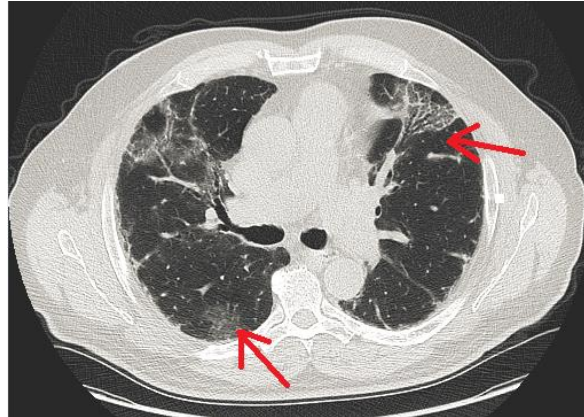


Figure 2.3. Ground Glass density with traction bronchiectasis as indicated by arrows

Extraction of segmented texture features can be computed by fractal dimensions of images that were transformed to binary by a two-threshold binary decomposition (TTBD) method by Costa et al.⁴². Their method was faster (1.6-3.7 times) in feature extraction and more accurate in classification than methods developed based on previous algorithms. TTBD uses two-level Otsu algorithm recursively to minimize intra-class variance and obtain a number of thresholds. To decompose images into binary, two-threshold segmentation is applied, and the lower and upper thresholds are extracted. Fractal dimension is computed from box-counting on extracted borders.

Applying fractal dimension and Lempel-Ziv complexity features to a linear classifier, Xu⁴³ reached a 90.7% accuracy in classifying GGO and normal lung out of 86 reticular ROIs.

Huang et al. developed a classification system based on features based on fractional Brownian motion⁴⁴ for analyzing pulmonary nodules. A total of 107 images from 107 different patients with pulmonary nodules were analyzed. Classifying malignant and benign nodules using fractal features and SVM resulted in 83.11% accuracy.

Additional information about aggressive and nonaggressive lung tumor differentiation was provided through fractal texture analysis of time-sequence enhanced CT images¹. Since differential box counting (DBC) algorithm is faster than fractional Brownian motion technique in calculating fractal dimensions, DBC is used for transforming images to FD images.

Kido *et al.*^{45,46} characterized ROI from lung CT images using fractal dimensions FDs. The texture of bronchioalveolar cell carcinomas (BACs) that reveal ground glass opacities are more complicated compared to non-BACs. Thus texture analysis could be useful in differentiating between normal and abnormal lung tissues for patients with lung tumors.

Zavaletta *et al.* employ features derived from image texture and the histogram of the ROI to analyze diffuse lung diseases such as interstitial pneumonitis and idiopathic pulmonary fibrosis⁶. They used multiple discrimination paradigms to cross validate their methods to report their results, which give accuracies, ranging from 75%-93% consistent with clinical diagnosis.

Park *et al.* present a new method called “score-block operation”, which is based on general image retrieval concept, with the K-NN classifier being employed for automated categorization of interstitial patterns in chest radiographs³⁸. They first extract the lung field with power spectrum and Quasi Gabor filter and subsequently use a 2-D Discrete Fast Fourier Transform to reduce the algorithm’s sensitivity to ribs and vessel shadows of lung. Van Ginneken *et al.*³⁹ developed a method to detect abnormalities in frontal chest radiographs through identification of abnormal diffuse textural nature, which are seen in mass chest screening for tuberculosis (TB). They employ automatic segmentation of the

lung fields, using active shape models and subdivide the lung fields into overlapping regions of various sizes. Texture features using the moments of responses to a multiscale filter bank are the first set of features in their study. They also use "difference features" obtained by subtracting feature vectors from corresponding regions in the left and right lung fields which are classified by majority voting using k-NN method. A separate training set is constructed for each region of interest. All regions are classified by voting among the k nearest neighbors, with leave-one-out method. Next, the classification results of each region are combined, using a weighted multiplier in which regions with higher classification reliability weigh more heavily. This produces an abnormality score for each image. They tested their methods on two databases. The first database contained 147 images from suspected Tuberculosis and had with textural abnormalities which were compared with 241 images from healthy subjects. The second database contained 100 normal images and 100 images with interstitial diseases. Authors report that their classification has sensitivity of 86% and 97% and specificity of 50% and 90% respectively in two databases³⁹.

Chest images of patients with Severe Acute Respiratory Syndrome (SARS) was studied by Tang et al⁴⁰. They examined the hypothesis that they could distinguish regions infected by SARS from normal lung using co-occurrence matrix as texture features. Since SARS regions are irregular, one cannot use shape to distinguish them from normal areas. They developed a multi-level dominant eigenvector estimate (MDEE) to alleviate the problem of large dimensionality of feature vectors and the high degree of correlation of neighbourhood features. Their accuracy of classification exceeded 96%.

A novel approach using two sets of wavelet filters, discrete wavelet frames (DWF) and rotated wavelet frames (RWF) were used to extract features from the lung tissue patterns⁴¹. Four different lung patterns (ground glass, honey combing, reticulation, and normal) are selected from a database of 340 images and are classified using support vector machine (SVM). Best results were obtained when above two filter banks were combined; which shows a complementary benefit in using them together.

Korfiatis et al. developed an automated scheme for volumetric quantification of interstitial pneumonia (IP) patterns, in a subset of diffuse interstitial parenchyma lung disease (DPLD), from a multidetector CT (MDCT) dataset. A lung-field segmentation is achieved by 3-D automated gray-level thresholding combined with an edge-highlighting wavelet preprocessing step, followed by a texture-based border refinement step. The vessel tree volume is identified and removed from lung field, resulting in lung parenchyma (LP) volume. Thereafter, identification and characterization of IP patterns are formulated through a three-class classification system into normal, ground glass, and reticular patterns, using 3-D co-occurrence features. Performance of the proposed scheme in identifying and characterizing ground glass and reticular patterns was evaluated by means of volume overlap¹⁰.

Approximately 15% of all respiratory diseases are known as diffuse lung disease (DLD), which can lead to respiratory failure. The DLD radiologically manifests as texture alteration of lung parenchyma. The clinical diagnosis of DLD in CT is primarily based on an assessment of lung parenchyma, its textural pattern and the extent and distribution of abnormal pattern within the lung. Certain protocols using high Resolution CT (HRCT),

only sample 10% of lung volume, however, volumetric Multi-Detector CT (MDCT) protocols are capable of capturing the entire lung volume. Such methods permit computer aided characterization and quantification of the entire extent of DLD. Using 3D feature sets, Mariolis et al. have obtained classification accuracies higher than 96.5%¹¹.

Quantitative textural analysis of lung has enabled the physician to perform classification and identification of diseases such as pulmonary fibrosis, normal/abnormal lungs, SARS, DLD, reticulation, emphysema, honey combing and parenchyma disorders. In this section, we examine classification of CT images from patients with specific disease conditions of the lung.

Identification of certain pulmonary diseases through CT images of the lung is through region growing procedures. In region growing, image characteristics in a particular part of the image are used to group individual pixels into regions. Coupled with boundary detection, region growing procedure is commonly used in segmentation of images. Region growing method involves selection of seed points to determine whether the pixel neighbors should be added to the region. Often several iterations are run on a particular image to identify areas which have similar characteristics.

Malone et al. employed texture based features from 102 image slices recorded from 34 patients⁴⁷. Of these 11 had normal lungs, 13 had fibrosis and 14 had emphysema. They trained an SVM based classifier to recognize typical disease patterns in the lung parenchyma using cross validation methods. They achieved accuracies ranging from 74% - 94%.

A pre-processing step in identifying pulmonary disease is to segment the lung tree. Segmenting pulmonary emboli and nodules will also give us useful information in terms of a computer aided diagnostic system. But this is challenging because of partial volume effect and high density air way walls⁴⁸.

Common interstitial pneumonia also known as UIP and UPF, involves inflammation of lung parenchyma. These diseases will affect the anatomy and decrease lung volume. The source of these diseases are found in characterization of changes caused by the disease process and extent of pulmonary involvement, which are best seen on HRCT⁶.

Honey combing is an extensive lung fibrosis with alveolar destruction which can be diagnosed with HRCT by thick-walled air-filled cysts. Wong et al. detected honeycombing by finding potential cysts by extracting dark, roughly circular structures of the lung from HRCT⁴⁹. Then they are clustered for potential honeycombing. Subsequently, regional information of clustering is calculated and machine learning algorithms are used for classifying these regions. The lung is segmented using morphological and active contour snake algorithm, since this disease is primarily located only in the lung boundary⁴⁹.

To enable content based retrieval of patterns of pathological conditions, Shyu et. al implemented a human-in-the-loop (a physician-in-the-loop, more specifically) approach in which an expert delineates the pathology bearing regions (PBR) and a set of anatomical land-marks in the image when the image is entered into the database⁵⁰. The ASSERT system developed By Shyu et al. requires physicians to manually mark the regions. Then they record honeycombing, texture attributes among other information. An optimal set of features is chosen among those with higher divergence and subsequently a Bayesian

classifier is used⁵⁰. To reduce the dimensionality of the attribute space, they use sequential forward selection method and then a decision tree to determine whether that region is similar to other honeycombing images in the database. Another related paper uses an adaptive multiple feature method (AMFM) to detect abnormal tissues which use 17 texture based features⁵¹.

Measuring pulmonary abnormalities in chest CT images when an infection such as H1N1 is present, is reported by Yao et al.¹⁴. They first segment both left and right lung using region growing and dynamic programming methods. Then using blocks of 16×16 pixels they apply a multidimensional feature vector which contains 25 different texture features of histogram, co-occurrence and run length matrix. They also detected statistically significant differences in the receiver operator characteristics (ROC) curves for detecting abnormal regions in H1N1 infection between normal lung and regions of fibrosis⁵², with significant differences in texture features of different infections. It is reported that the researchers were able to quantify abnormal lung volumes in CT imaging.

1. EMPHYSEMA

Cigarette smoking is the primary risk factor for chronic obstruction pulmonary disease (COPD) and mostly affects people in the sixties and seventies. As a major component of COPD, emphysema is defined histologically as the condition of the lung characterized by permanent, abnormal enlargement of airspaces distal to the terminal bronchiole, accompanied by tissue destruction of alveolar walls, leading to breathlessness⁸. Emphysema often results in shortness of breath and leads to COPD which is characterized by airflow limitations⁵³. There are three types of emphysema, commonly called centeri-

lobular, paraseptal, and panlobular⁵³. Figure 2.4 shows Para-septal emphysema and centri-lobular emphysema on CT image of the lung.

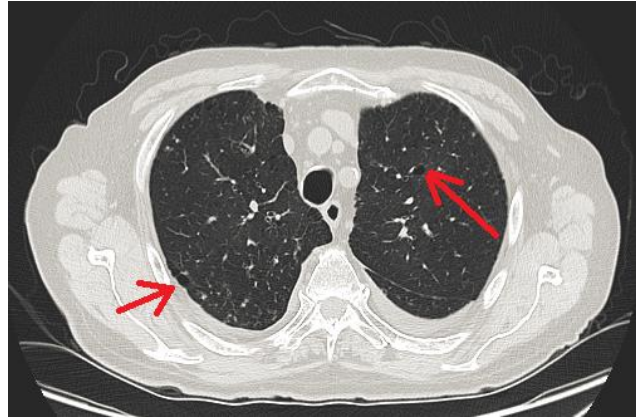


Figure 2.4. Para-septal emphysema and centri-lobular emphysema, identified by arrows

CT is very helpful in identifying Emphysema which is chronic and progressive. The CT has remained the gold standard for identifying emphysema especially with multi-detector CT scanners that are capable of acquiring more than 300 sections per rotation⁹. Radiologist's accuracy in identifying the abnormal pattern generated by emphysema in a lung CT is between 65 to 80 percent. Classification based on texture analysis is a very useful method in quantification of the disease⁹.

Identifying emphysema, fibrosis or normal parenchymal tissue based on thresholding can be performed with relative ease, but the challenge is to differentiate between normal and abnormal lung, due to the volume effect. If emphysema and fibrosis are both present, density based methods do not work well and because, fibrosis⁵⁴ will lead to a small number of voxels with low attenuation, while emphysema has many more voxels and the mean values of intensities of both diseases can be classified as belonging to normal lung.

Therefore, texture analysis can be useful, since it is not only based on density features⁵⁵ but it takes local values into account too⁵³.

Xu et al. have enhanced the ability to differentiate normal lung with 3D texture features arising out of MDCT images. They had 34 human patients with chest MDCT and they categorized them as following: EC, emphysema in severe chronic obstructive pulmonary disease (COPD); MC, mild emphysema in mild COPD; NC, normal appearing lung in mild COPD; NN, normal appearing lung in normal non-smokers; and NS, normal appearing lung in normal smokers. COPD was based on pulmonary function tests (PFT). Airways and vessels were excluded from texture features. Bayesian classifier and leave one out method were employed for discrimination and validation respectively⁸. Accuracy with two way classification reached up to 99%.

Sørensen et al employed local binary patterns (LBP) obtained from CT images as texture features, and joint LBP and intensity histograms are used for characterizing regions of interest⁵³. Classification is performed through a k-NN classifier wherein a histogram dissimilarity measure is used as distance metric. They report a 95.2% classification accuracy on 168 manually annotated ROIs, comprising 3 pathologies, namely normal tissue, centri-lobular emphysema, and paraseptal emphysema⁵³.

2. CANCER

Lung cancer is the major cause of cancer deaths in North America^{17, 56}. Tobacco consumption is the main reason for lung cancer and about 87% of lung cancers are likely due to smoking or passive exposure to tobacco smoke⁵⁶. If lung cancer is detected at an early stage, there is a 40% chance for 5 year survival⁵⁶. Studies have calculated an average

of 30% miss rate in early detection of lung cancer. Imaging of the lung through CT has found a prominent place in diagnosis of lung cancer. In earlier stages cancer is seen as non-calcified nodules in CT images which has a low attenuation with spherical appearance⁵⁷. Fractal analysis of sequenced contrast enhanced images of CT have been studied as a potential tool for identifying aggressive and malignant tumors³⁹. Using box counting algorithm, DICOM images were transformed to fractal dimension (FD) are measured. Based on their research vascularized tumor regions had fractal characteristics and their quantitative classification had accuracy of 83%⁵⁷.

Tumor vasculature is related to tumor aggression and CT is routinely used in identifying soft tissue behind the bone which makes detecting them with other anatomical imaging modalities difficult. Assessment of lesion heterogeneity and surface irregularity on CT using fractal analysis can identify normal tissue and tumors. Identification of aggressiveness of the tumor can be researched by examining the image texture. The extent of spread of cancer is described by the tumor stage, so it is very important to be able to improve tumor stage prediction¹.

Interpreting chest radiographs is not always straight forward because of its complex background. CT images can eliminate the superposition of an atomic structure but the trade-off is much more data for the radiologist. By use of the Eigen values of Hessian matrix of the image, Sato *et al.* constructed blob, line, and sheet enhancement filters⁵⁸. Those filters may also consume much time for computing Eigen values of Hessian matrix for each image pixel at different scales, even just from a number of equations. A filter is used to detect

early cancer that enhances the local contrast of the ROI, including nodules and normal structures (vessels and airway walls) with similar attenuation or textures to nodules⁵⁹.

It has been shown that fractal analysis of lung tumor's texture in CT images can assist in distinguishing between aggressive and non-aggressive tumors⁶⁰. Fractal contrast enhancement (CE) using CT for differentiating between aggressive and non-aggressive malignant tumors was studied on branches of blood vessels¹. Al-Kadi and Watson performed fractal analysis on contrast enhanced CT images from each of 15 patients. A sequence of 11 images recorded in time were used from each patient to determine the fractal dimension and lacunarity. Fractal texture features and quantitative classification over tumor regions resulted in 83.3% accuracy to distinguish between advanced (aggressive) and early-stage (nonaggressive) malignant tumors.

Lung with CT using fractal extraction based on DBC to compare bronchiole alveolar cell carcinomas with non-bronchiole alveolar cell carcinomas was examined by Kedi et al⁴⁵. Characterization of lung CT images using FD can help distinguish brochiogeic carcinomas from benign pulmonary nodules⁴⁶.

An effective surgical treatment for cancer is the removal of the diseased lung lobes which is called lobectomy. In order to maintain the maximal lung functionality, the surgical team and the radiologist needs accurate information regarding how the cancer has spread across lung lobes. A 3-D visualization can make these kind of assessments easier since it would eliminate the reconstruction of objects¹⁷. To create such 3-D visualization we need to be able to segment lung lobes. Wei and Hu¹⁷ have combined two textural features to achieve

such an objective and claim that textural analysis can be more easily investigated for visualization.

Small and non-small size cancers in lung were studied through nodule detection using geometrical and texture features. Namely the GLCM was used to compare texture features⁵⁶. Pulmonary nodules are a common sign of lung cancer. Anand computed GLCM based textural features from CT images which served as input to a backpropagation neural network, to classify each image as cancerous or non-cancerous and report promising results. He suggest that the procedure can provide supplementary information to the radiologist to arrive at the diagnosis of lung cancer⁵⁸. Textural (GLCM) and geometrical features were inputs to a NN to classify benign and malignant tumors.

VII. APPLICATION OF SCALE INVARIANT FEATURE TRANSFORM IN CT IMAGES OF THE LUNG

The SIFT method of detecting features from images was introduced by David Lowe⁶², and it is mainly used in object detection and face recognition applications. SIFT has recently been used in medical image quantification. Chapter 5 describes the method in detail and discuss results in classification of CT images of the lung. Below is a review of SIFT applications in medical imaging

Kamencay et. al⁶³ proposed a hybrid approach of using SIFT descriptors with PCA and KNN for classification. SIFT features are extracted and PCA method is applied for labeling proper matches based on the closest neighbor to the training set, if not successful, the output of PCA is applied to a KNN. An application of this method can be a 3D model of internal organs from an endoscopic video. This method was tested on Caltech 101

database and colonoscopy test image database with resulting recognition rates of 92% and 84% respectively.

Four categories of lung nodules, namely: well-circumscribed, vascularised, juxta-pleural and pleural-tail are classified using SVM by extracting SIFT descriptors in two steps: first, an image patch division approach is used for foreground and background pixel indexing, second, transforming the result of the first step into feature vector using context curve feature descriptors (Zhang et. al^{64,65}). This method was tested on Early Lung Cancer Action Program database with near 90% average classification rate which was higher than similar methods such as SVM-SIFT, PCA-SIFT and linear discriminant analysis upon SIFT descriptors.

Effectiveness of SIFT, LBP and SURF descriptors are assessed on false positive and classification of lung nodules (Farag et. al⁶⁶). An active appearance model creates templates for common nodules. Candidates are detected by a normalized cross-correlation from this template. And geometric descriptors are extracted from nodule candidates. These methods are tested on early lung cancer action project (ELCAP) database and demonstrated a 2% increase in specificity of the above assessment.

While raw SIFT and LBP were not successful in classification, transforming SIFT descriptors to smaller vectors using PCA and linear discriminate analysis (LDA) increased nodule accuracy of classification when coupled with LBP.

Classification of four lung nodule categories: well-circumscribed, vascularized, juxta-pleural and pleural-tail, is performed with SVM. SIFT descriptors are reduced to 4-length probability vector for every category using weighted similarity network on SVM.

Overlapping types are assessed using clique Percolation method. This algorithm is evaluated on ELCAP database⁶⁵.

In another laboratory, SIFT descriptors were used for segmenting lung fields that were obtained from serial radiographs, along with deformable contour that was constrained based on population and patient-specific shape statistics. This method had higher accuracy and specificity was higher in comparison with active shape models⁶⁹.

The SIFT keypoint identification was evaluated by applying changes such as rotation, scaling, stretching, brightness, contrast and adding noise to an image and re-calculating the keys. 78% of the keys matched in location, scale and orientation in its altered image.

Since texture analysis can only take the averaged feature into account, identifying honeycombing and reticular patterns can become cumbersome due to inhomogeneous texture.

Kato et. al⁶⁷ used texture images as histogram and use intensity and SIFT descriptors for feature extraction. This Method was applied to 1109 ROIS from 211 patients for classifying five classes: ground glass, reticulation, honeycombing, emphysema and normal lungs that resulted in 92.8% accuracy for each class. However, their analysis is focused on inhomogeneous texture patterns and texture classification accuracy. This method lacks the capability of homogeneous patterns quantification, analysis based on ROI's of different sizes, and classification accuracy for more than 5 patterns. However, higher accuracy was reported based on only texture features with more classes is discussed by Rui Xu et al⁶⁸. They demonstrated the highest classification accuracy on six pulmonary patterns: consolidation, ground-glass opacity, honeycombing, emphysema, nodules and normal

tissue. Since shape detection is a useful information, they extracted features from 3D data sets and calculated Eigen-values of Hessian matrices. 16 statistical measures based on mean, variance, skewness and kurtosis statistical features are extracted from three Eigen-value cubes. A Gaussian SVM classifier reaches 95.85% recognition rate based on 20-cross validation test based on their report.

VIII. ASSESSMENT

To estimate general capability of a statistical classifier we can use a cross validation procedure. The standard deviation of two or more parameters is calculated to measure accuracy and robustness of the system.

Leave one out is a simple validation technique that omits the i^{th} element where the original data $X_1, \dots, X_i, \dots, X_n$ is in separate sets $S_1, \dots, S_i, \dots, S_n$ with $n - 1$ elements. The static mean of each set is calculated as n-fold estimate. So each element is used as a training set and also for testing. The evaluation is as follows⁵⁵

$$\text{Volume overlaps (VO)} \quad VO = \frac{O \cap C}{O \cup C}$$

$$\text{True positive fraction (TPF)} \quad TPF = \frac{o \cap c}{o}$$

$$\text{False-positive fractions (FPFs)} \quad FPF = \frac{O \cup C - O}{O}$$

O is the ground truth that is provided by a radiologist and C is the computer driven result¹⁰.

To measure performance of classification we can also use⁶¹

$$SENSITIVITY = \frac{TP}{TP + FN}$$

$$SPECIFICITY = \frac{TN}{TN + FP}$$

$$ACCURACY = \frac{TP + TN}{TP + FP + TN + FN}$$

Where, TP is the true positive, TN is the true negative, FP is the false positive and FN is false negative.

IX. DISCUSSION

It is becoming increasingly evident that texture analysis applied to lung images obtained from CT has significant potential in identifying regions of pathology and thereby assist the diagnosing physician. This is due to the nature of these patterns, as radiologists also compare texture of the lung parenchyma to understand the root causes of a disease. Computerizing the identification process and classification of diffuse lung disease would help radiologists save time during radiological examination of CT images of the lung and narrow down abnormal disease patterns, which is the primary motivation for this thesis.

For instance it is easy to miss a nodule or identify the type of nodularity incorrectly. Such small misses may result in increased false positives which can potentially jeopardise someone's life. Therefore, a computer assisted classification method can result in a higher accuracy and will benefit both the patient and the radiologist.

There are a number of challenges associated with such an undertaking. On one hand, a computer scientist faces the challenge of acquiring relevant data which is often confidential, it also requires a radiology specialist to devote considerable amount of time in narrowing down many images which are highly indicative of pathologies of the lung. Some regions of interest may have several abnormalities which will not result in a clean feature extraction

and classification. On the other hand in order to write good software, the computer scientist must familiarize himself/herself with a new field of study and understand the pathophysiology of several diseases so as to be able to identify and characterize patterns associated with specific diseases. When these challenges are successfully overcome, it may trigger creative thinking of the programmer to come up with an algorithm that captures the process which a radiologist goes through to identify and classify the image segment under question. Such novel algorithms will consist of multiple image processing tools and techniques to capture as many angles of the manual process as possible.

Although many texture analyzing algorithms are produced by research groups all over the world, results and challenges documented in this review demonstrate that there is considerable amount of work that needs to be done to usher such algorithms into clinical practice.

X. CHAPTER SUMMARY

A set of features that can correctly identify the pathological patterns in a biomedical image are needed to perform identification and classification of lung images. To obtain features with high specificity, all images need to have suitable resolution and well defined radiological pathology. Extraction of optimal features from an image often requires a combination of domain knowledge and formulation of mathematical descriptors of features. In this context the use of texture analysis accompanied by fractal analysis can provide a well-defined set of features to enable classifiers such as ANN and SVM to classify CT images of the lung, as being from a healthy subject or from a patient, with high

accuracy and assist the physician during diagnosis. These issues are the subject of subsequent chapters.

CHAPTER 3

EVALUATION OF TEXTURE FEATURES OF PATHOLOGICAL PATTERNS IN THE CT IMAGES OF THE LUNG

I. Introduction	52
II. Feature Extraction using Texture Based Methods	52
A. Tamura Features	53
B. Compound Local Binary Pattern Algorithm	57
C. Gray Level Co-occurrence Matrix.....	59
D. Haralick Features.....	61
E. Gabor Filter Analysis	76
F. Geometric Quantification based on Minkowski Functionals	79
III. Processing of Labelled CT Image Data and Training of the ANN	84
IV. Classification Accuracy of Feature Sets Derived From Various Texture Analysis Methods	88
V. Results	97
VI. Chapter Summary.....	99

I. Introduction

Empirical observations by practicing radiologists and a review of literature published from a large number of laboratories suggest that diffuse lung diseases (DLD) are well described by variations of texture in CT images of the lung^{70, 71, 72, 73, 74}. These diseases impact the texture of parenchyma to a level that it has resulted in significant amount of research which focuses on algorithms that can detect the texture and surface changes on images of the lung. Using these methods, researchers have achieved reasonable accuracies in classifying typically up to five or six pathological patterns^{75, 76, 77, 78}. A major limitation of current research is that classification accuracy has been reported for only 6 set of pathologies. Therefore, it is worth examining if various combination of texture features, identified from literature, can perform better than what is reported in literature.

In this chapter, several texture analysis methods and features derived from CT lung images are theoretically analysed and their quantification results are expressed and evaluated for different pathological patterns. Furthermore, this chapter will describe the most effective algorithms used for feature extraction of the lung texture from CT images, to enable classification of up to 10 classes of DLD pathologies. Accuracy of classification while using ANN for different number of abnormalities is also provided.

II. Feature Extraction using Texture Based Methods

Several texture based methods were systematically described in chapter 2. Details of some of the most effective and descriptive texture algorithms which have demonstrated high classification accuracies in literature are presented in this chapter. Algorithms based on Tamura^{79, 80}, CLBP^{90,91}, GLCM^{99,100}, Haralick^{103,104}, Gabor filter^{110,111}, geometric

quantification and Minkowski Functionals^{117,118,119,120} generate a wide variety of features, and are highlighted with corresponding DLD CT images, in this chapter.

A. Tamura Features

Tamura features^{81, 82, 83} provide an accurate approach towards texture analysis since they focus on human psychological perception of texture. It consists of six visual features which quantify coarseness, contrast, directionality, line likeness, regularity and roughness^{84,85,86,87}. However, only initial three features are used. The latter three features are highly correlated with the initial three features and therefore, are not used.

Coarseness is the most fundamental texture element among Tamura features^{88,89}. It defines the roughness of a surface by averaging gray level value (GLV) of each pixel in the image on six different window sizes, $2^n \times 2^n$; where $n = 1, 2, \dots, 6$. When $n = 1$, GLV is calculated in four directions, taking the pixel in question as one of the four pixels. And for every increasing window size, the pixel will be at the middle of the window where average GLV is evaluated. The average GLV at the window size with the highest absolute difference of the pixel GLV is divided by the whole image's average GLV. Since the feature computed as above, is so effective in identifying roughness, we have used its histogram distribution as another feature too.

The average at every pixel over a neighbourhood is calculated as below:

$$A_n(x, y) = \sum_{i=x-2^{n-1}}^{x+2^{(n-2)}-1} \sum_{j=y-2^{n-1}}^{y+2^{(n-2)}-1} \frac{f(i,j)}{2^{2n}}.$$

The difference between each average at every neighbourhood in horizontal orientation is given by:

$$E_{n,h} = |A_n(x + 2^{k-1}, y) - A_n(x - 2^{k-1}, y)|$$

and the vertical difference is also calculated.

Contrast is computed from the image's gray level (GL) range and the extent of black or white distribution. It is not simply the mean GLV of an image in Tamura analysis. The first element is measured based on GL standard deviation (σ) and the second element is based on kurtosis. Kurtosis is the fourth central moment (μ_4) of the GLV, relative to the square of the variance. Kurtosis is defined as $(\frac{\mu_4}{\sigma^4})$ where μ_4 is the fourth central moment of variable^{88,89}.

Thus, Contrast is defined as:

$$Contrast = \frac{(\sigma)}{\left(\frac{\mu_4}{\sigma^4}\right)^{1/4}}$$

Directionality is determined by Sobel edge detector to calculate edge strength $e(x, y) = 0.5(|\Delta_x(x, y)| + |\Delta_y(x, y)|)$ and direction angle $a(x, y) = \tan^{-1} (\Delta_y(x, y)/\Delta_x(x, y))$ on horizontal and vertical GL pixel difference of 3×3 windows^{88,89}

$$\begin{array}{ccc} -1 & 0 & 1 \\ -1 & 0 & 1 \\ -1 & 0 & 1 \end{array} \quad \begin{array}{ccc} 1 & 1 & 1 \\ 0 & 0 & 0 \\ -1 & -1 & -1 \end{array}$$

Δ_y, Δ_x are the gray level differences of neighbouring pixels in vertical and horizontal directions. A histogram $H(\alpha)$ with bins as directional angle and edge strength characterized as counts is computed. If the image is highly directional, peaks will be more vivid in the histogram. The formula for calculating the Tamura's directionality is given by:

$$D = 1 - rn_p \sum_{p=1}^{n_p} \sum_{\alpha \in w_p} (a - a_p)^2 H(\alpha).$$

Where r is normalizing factor, α is a quantised directional angle, n_p is the number of peaks, a_p is the p^{th} peak position and w_p is the p^{th} peak angle range.

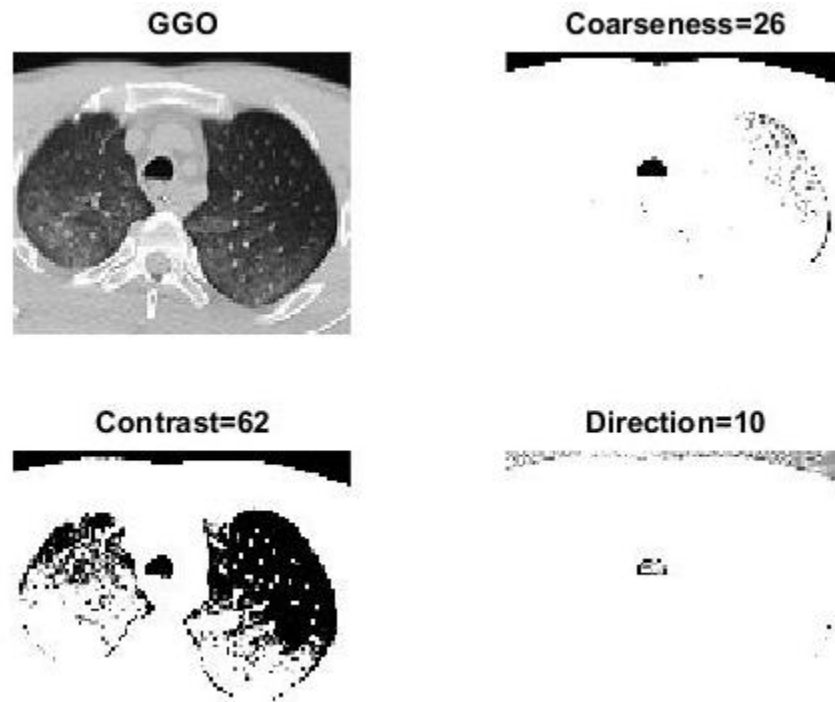


Figure 3.1. Tamura features of a CT image from a patient with GGO. Top left: original image; All others are image representations of their features with the values calculated for each

These three features are shown by gray level range on CT image segments of ground glass opacity (GGO) and Emphysema on figures 3.1 and 3.2. The GGO is best characterized by contrast in terms of computational description, as it is with human eye. Emphysema on the other hand is best described by coarseness and directionality. The learning algorithm of the classifier, will be trained based on such information computed from a set of training images

and can potentially result in high classification accuracies when combined with other features.

Computed values for each Tamura feature from the images with the GGO and emphysema (depicted in Figures 3.1 and 3.2) are extracted from the relevant ROI. However, in order to provide a better visualization, the whole lung is shown.

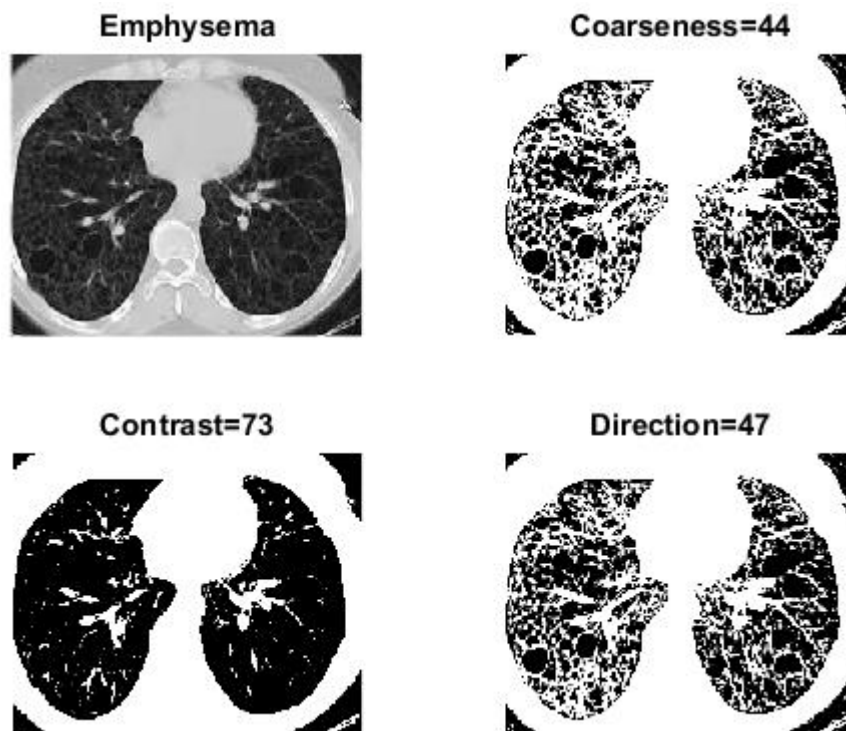


Figure 3.2 Effects of Tamura features on an image identified with emphysema; Top left: original image; all other images are values derived from Tamura features

The ROI value for coarseness is 26 for the image depicting GGO and 44 for the image of patient with emphysema. This implies that when a classifier is trained based on coarseness feature alone, it will associate a ROI which has a Tamura coarseness value of 26 for GGO class and a value of 44 to the Emphysema are demonstrated on Figures 3.1 and 3.2. The same principle is applied to other Tamura features demonstrated in both figures. The range

of each feature will be determined primarily based on the formula and to a lesser extent on the number of ROI's provided to the classifier for training with semi-supervised learning. The usefulness of multiple features to identify a pattern generated by a particular disease is obvious. Furthermore, feature ranges vary and are not always perfectly set for every pathological pattern. For instance, feature F could have value X for a GGO ROI and value Y for another GGO ROI. If X and Y are in the similar range (eg: $X=1.1$, $Y=1.12$) then they have a high probability of being generated by the same disease. However, if ranges are different (eg: $X=1.1$, $Y=22$), it is likely that images belong to different classes properly. The same feature F can be well descriptive for a number of patterns, and not so for the rest. In addition, a single texture feature does not describe a class completely, since the image is generated by stochastic variations in the image intensity. Therefore, it is intuitive that multiple features are needed to characterise each disease pattern distinctly, and a combination of such features will separate images into different classes. Automation of such a task is performed by an artificial neural network (ANN) trained for the above paradigm.

B. Compound Local Binary Pattern Algorithm

Compound local binary pattern (CLBP) is a frequently used texture feature in the literature^{92,93,94}. Although, it is called a pattern, essentially the CLBP is a single number to characterize the variation of intensities and consequently the CLBP denotes the texture within a ROI. To compute CLBP, each pixel is compared with its eight neighbouring pixels. When the pixel in question is greater than its neighbour, a number 1 is assigned to that neighbour or a zero otherwise. An eight digit binary number is formed in a clockwise

manner, starting from the pixel on the upper hand left corner. A normalized histogram is then computed based on the decimal values assigned to each pixel to demonstrate CLBP texture feature of the ROI, since regions of interest could be of different size and normalizing them can result in a comparable feature^{95,97,98}.

As an example, consider an image (Figure 3.3) with pixel value 152. By comparing it with its eight neighbours, the binary output from all 8 pixels is $(01110000)_2$ which is equal to $(112)_{10}$. Figure 3.3 demonstrates CLBP on an image identified with honeycombing. The histogram is depicted based on the honeycombing ROI⁹⁶.

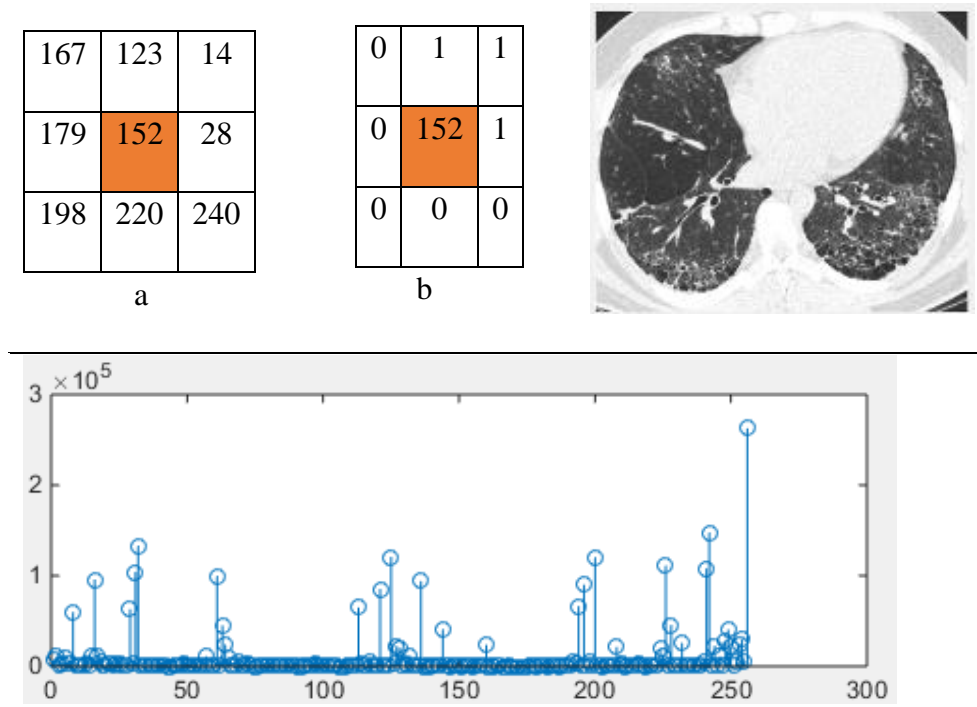


Figure 3.3 Upper left corner (a) shows pixel values around a centered pixel. Upper middle (b) is the CLBP evaluation. Upper right corner (c) is CT image of lung identified with honeycombing and GGO. The above graph demonstrates the histogram of the CT image base on CLBP

C. Gray Level Co-occurrence Matrix

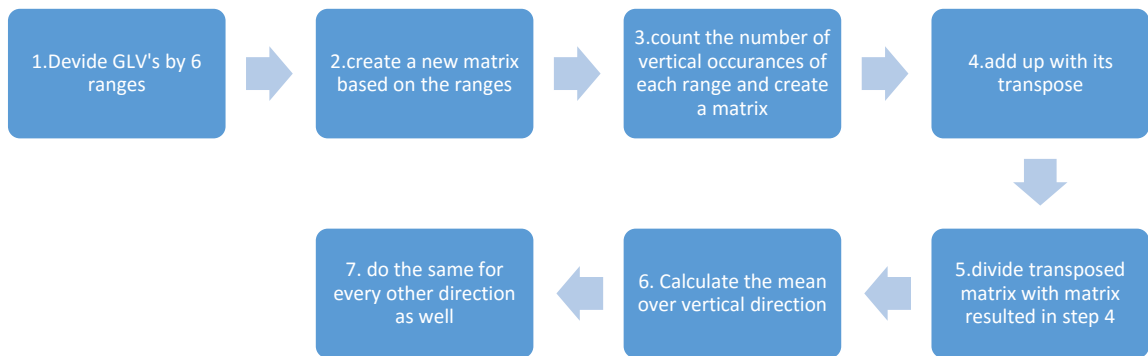
The gray level co-occurrence matrix (GLCM) extracts second order statistical texture features and generates a matrix where the number of rows and columns are equal to the number of gray levels in the image^{101,102}. The GLCM is defined as a tabulation of how often different combinations of pixel brightness values (grey levels) occur in an image. The GLCM has characteristics that can be summarized through some feature functions over the ROI matrix (GLCM calculates occurrence frequency of a relative pixel at a specific distance and neighbourhood. If an image has a random texture pattern vertically, and a dominant horizontal structure, GLCM will have a description which is in between these two extremes. This is because, the analysis is averaged over every direction. To calculate a GLCM one can use the formula:

$$C_{\Delta x, \Delta y}(i, j) = \sum_{p=1}^n \sum_{q=1}^m \begin{cases} 1, & \text{if } I(p, q) = i \text{ and } I(p + \Delta x, q + \Delta y) = j \\ 0, & \text{otherwise} \end{cases}$$

Image I is of size $n \times m$, and $\Delta x, \Delta y$ are the horizontal and vertical pixel neighbourhood differences. The GLV is denoted by i and j ; p and q are spatial positions in the image.

Computation of the GLCM is as follows: One divides GLV's of each pixel to 6 different thresholds. Then assigns each pixel to its respective class. Then a one counts of the number of vertical occurrences of a threshold with its right neighbour generates a new matrix. We add up the values in this matrix with its transpose (T) and calculate the sum of resulting values (S). Then a similarity matrix is created based on $\frac{T}{S}$. The normalized value is the sum

of $\frac{T}{S}$ for each matrix cell. The mean over vertical and horizontal normalized matrix is calculated. The offset or the distance of the gray level value repeated in its neighbourhood affects GLCM.



To generate a GLCM, first one divide GLV's of each pixel to 6 different thresholds. Then assign each pixel to its respective class and create a new matrix based on that. Then a count of the number of vertical occurrences of a threshold with its right neighbour generates a new matrix. We add up the values in this matrix with its transpose (T) and calculate the sum of resulting values (S). Then a similarity matrix is created based on $\frac{T}{S}$. The normalized value is the sum of $\frac{T}{S}$ for each matrix cell. The mean over vertical and horizontal normalized matrix is calculated. The offset or the distance of the gray level value repeated in its neighbourhood affects GLCM.

This method is demonstrated on a ROI which is classified as honeycombing with four different offsets; figure 3.4.

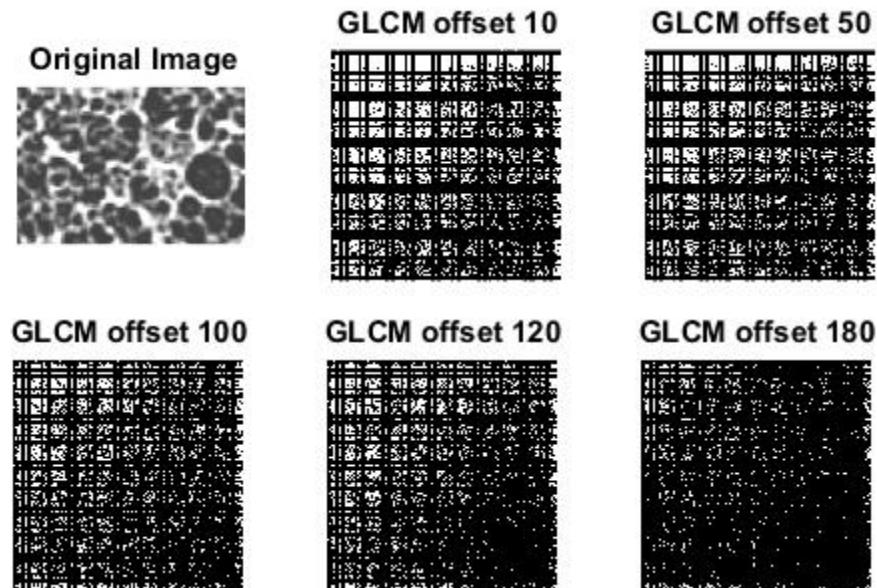


Figure 3.4 GLCM evaluation of an image with different offsets

If the offset is too close or too far, the matrix would have less data for statistical analysis.

The offset is calculated as

$$\frac{\max\{pixels_x, pixels_y\}}{2}$$

The honey combing ROI has 240×220 pixels in vertical and horizontal directions, so the offset for this GLCM would be 120. $pixels_x$ and $pixels_y$ demonstrates pixel values in x and y directions.

D. Haralick Features

Haralick introduced 14 features which have been used as the source of texture descriptors in various forms: angular second moment, contrast, correlation, variance, inverse difference moment, sum average, sum variance, sum entropy, entropy, difference variance, difference entropy, information measure of correlation. We have chosen not to use maximal

correlation coefficient function from this list, as it is the least descriptive feature and gets omitted by principal component analysis in every extraction^{105,106}.

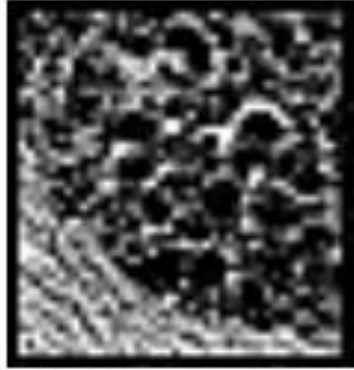
In order to illustrate the computation of Haralick features, the following figures are generated. For each Haralick formula two sets of images, each containing four ROI's (honey combing, consolidation, GGO and emphysema) are evaluated below. To compare the range of each feature, driven from each formula, one can compare the ROI from the upper set with the one from the lower set of images to assess how that feature describes a particular pathological pattern. Features which provide excellent quantitative measure of the texture within the ROI are pointed out for these figures^{107,108}. When the features are in the same range for the same pattern on all ROI's, the classifier will be trained more accurately and therefore classification results will be higher.

In formulas¹⁰⁹ that follow, ϕ_{ij} is the $(i, j)^{\text{th}}$ normalized matrix pixel value, μ and σ are the mean and standard deviation (variance) over horizontal and vertical columns of GLCM. L is the number of gray levels in GLCM. Haralick features are demonstrated for various images and the formula used for calculating each feature is also presented¹⁰⁹.

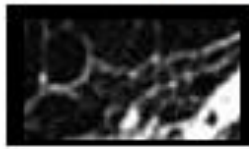
Haralick feature 1: Angular Second Moment (Energy) is the sum of squared GLV of

$$\text{every pixel within the ROI: } \sum_{i=0}^{L-1} \sum_{j=0}^{L-1} (\phi_{ij})^2$$

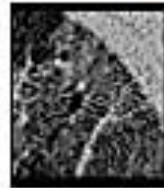
Honey Combing=0.025 Consolidation=0.13



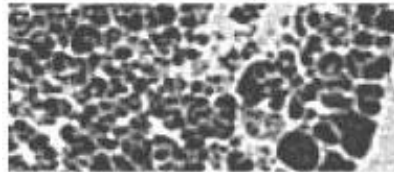
Emphysema=0.29



GGO=0.22



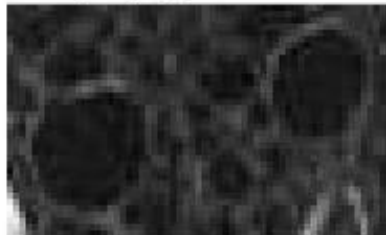
HoneyCombing=0.095



Consolidation=0.29



Epmphysema=0.19



GGO=0.24

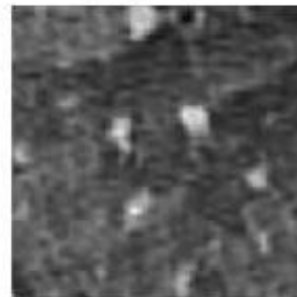


Figure 3.5 Sample image ROIs from different pathologies. Comparing Energy value on two sets of honey combing, consolidation, emphysema & GGO shows similar range of values. This feature is well descriptive for GGO (upper image:0.22; lower image:0.24)

Haralick feature 2: Contrast is evaluated as below according to Haralick when $|i - j| = n$

$$\sum_{n=0}^{L-1} n^2 \sum_{i=0}^{L-1} \sum_{j=0}^{L-1} \phi_{ij}$$

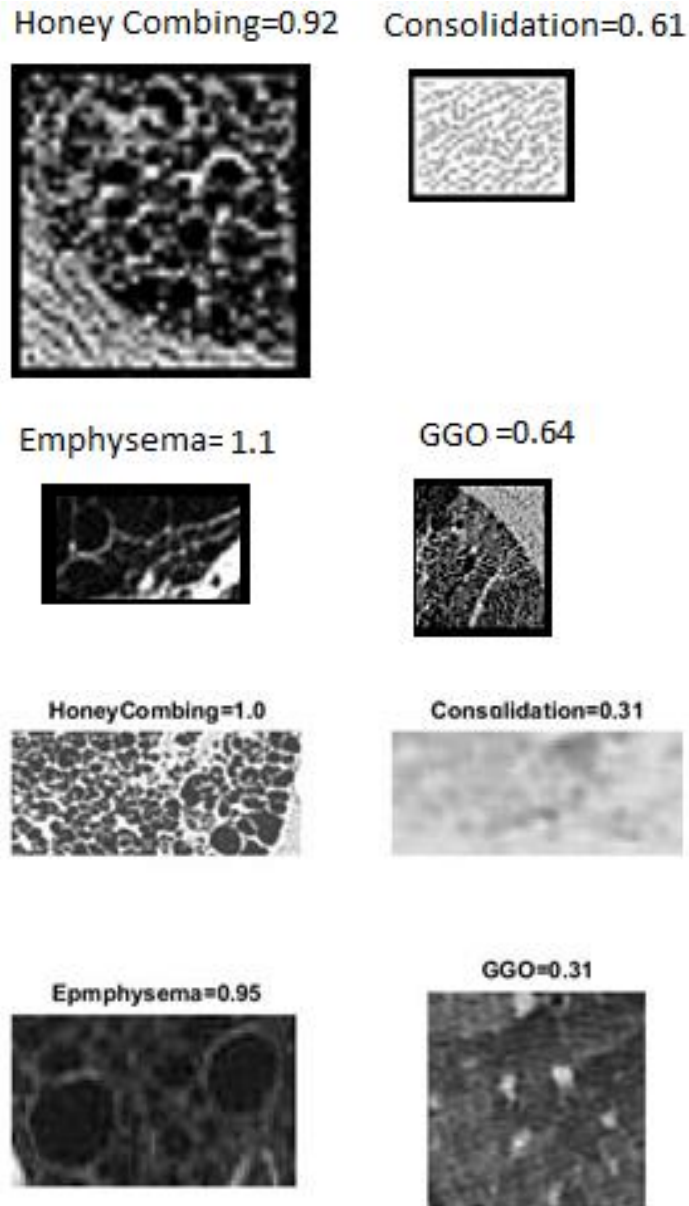
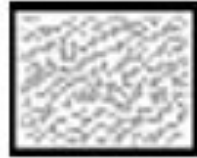
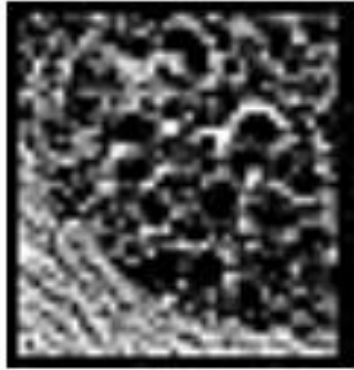


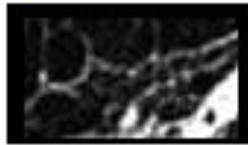
Figure 3.6 A comparison of Contrast values on two sets of honey combing, consolidation, emphysema & GGO shows similar values. Contrast feature is well descriptive for honey combing (upper image:0.92) and emphysema (upper image:1.1; Lower image:0.95)

Haralick Feature 3: Correlation = $\frac{\sum_{i=0}^{L-1} \sum_{j=0}^{L-1} ij \theta_{ij} - \mu_x \mu_y}{\sigma_x \sigma_y}$

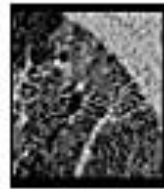
Honey Combing=0.31 Consolidation=0.304



Emphysema= 0.34



GGO = 0.601



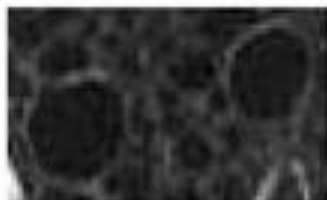
HoneyCombing=0.83



Consolidation=0.55



Epmphysema=0.55



GGO=0.8

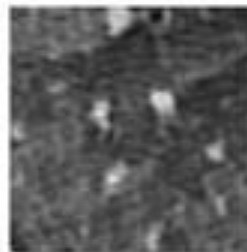


Figure 3.7 A comparison of Correlation values on two sets of honey combing, consolidation, emphysema & GGO shows similar values

Haralick Feature 4: Sum of Squares (variance) = $\sum_{i=0}^{L-1} \sum_{j=0}^{L-1} (i - \mu)^2 \phi_{ij}$

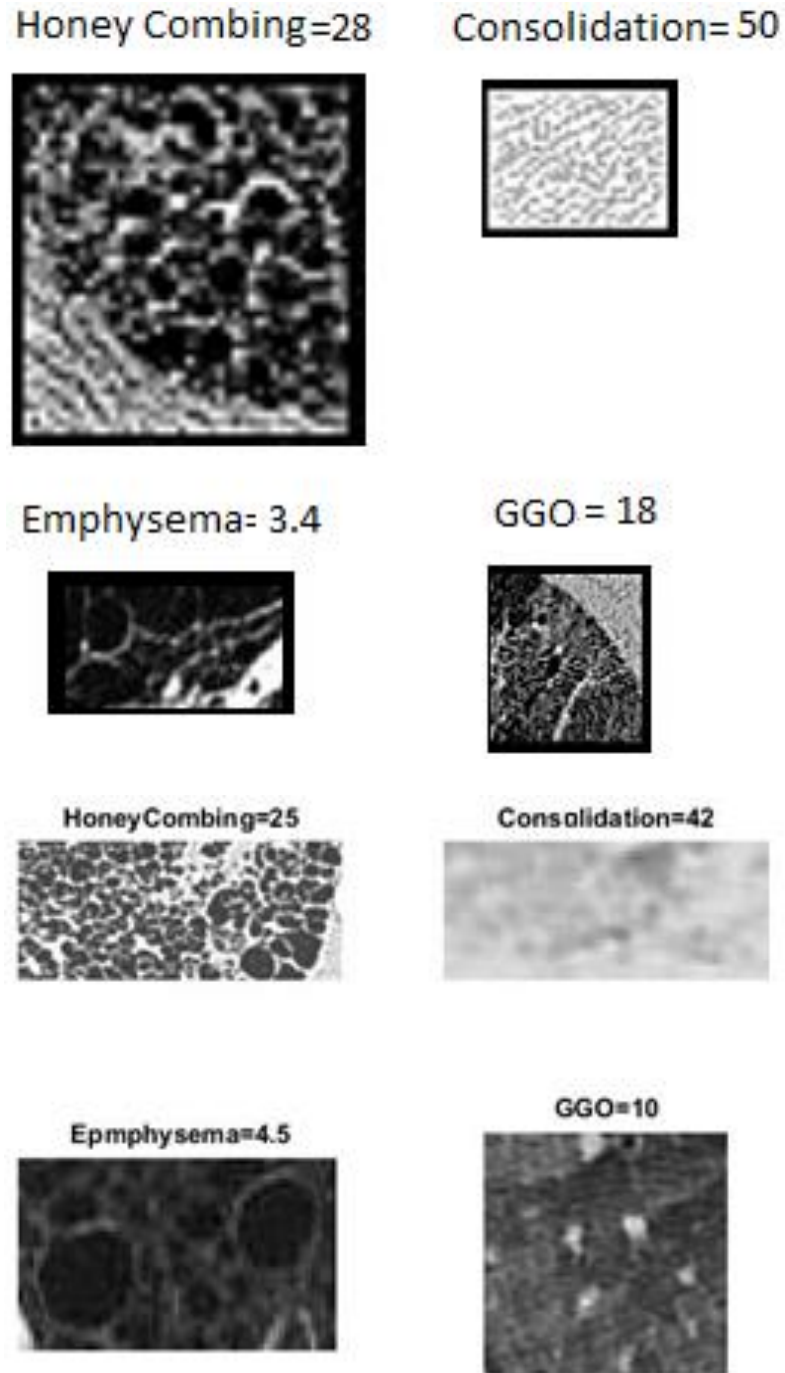
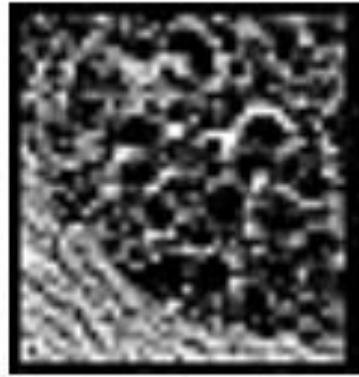


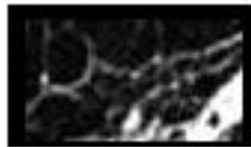
Figure 3.8 A comparison of Sum of squares variance values on two sets of honey combing, consolidation, emphysema & GGO. This feature works better for honey combing and emphysema as the results are in the same range

Haralick Feature 5: Inverse Difference Moment = $\sum_{i=0}^{L-1} \sum_{j=0}^{L-1} \left(\frac{1}{1+(i-j)^2} \right) \phi_{ij}$

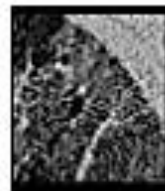
Honey Combing=0.89 Consolidation= 0.98



Emphysema= 0.99



GGO = 0.99



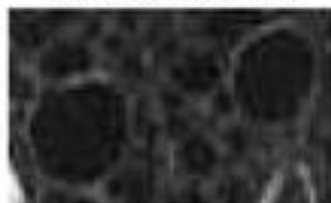
HoneyCombing=0.98



Consolidation=0.99



Epmphysema=0.98



GGO=0.99

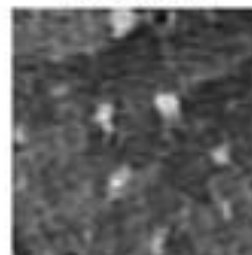


Figure 3.9 A comparison of Inverse Different Moment value on two sets of ROIs of honey combing, consolidation, emphysema & GGO shows similar range of values

Haralick Feature 6: Sum Average = $\sum_{i=2}^{2L}(i) \sum_{i=0}^{L-1} \sum_{j=0}^{L-1} \phi_{ij}$

When on last two sums: $|i - j| = i, i = 0, 1, \dots, L - 1$

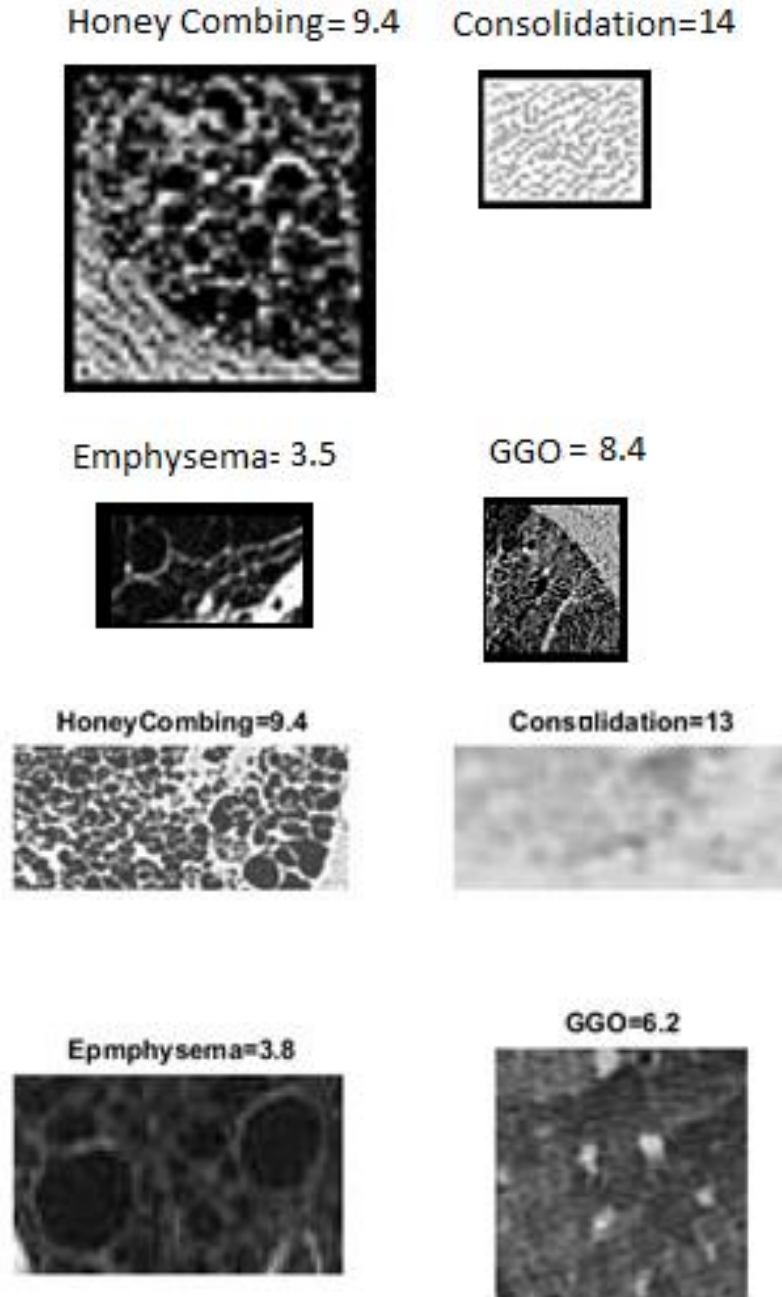
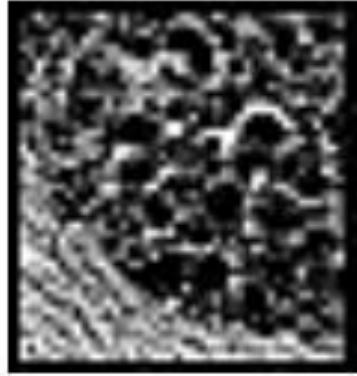


Figure 3.10 A comparison of Sum Average value on two sets of ROIs of honey combing, consolidation, emphysema & GGO shows similar range of values

Haralick Feature 7: Entropy = $-\sum_{i=0}^{L-1} \sum_{j=0}^{L-1} \phi_{ij} \log(\phi_{ij})$

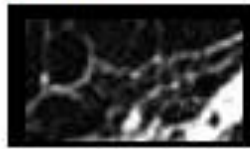
Honey Combing= 3.9



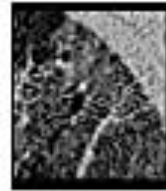
Consolidation= 2.3



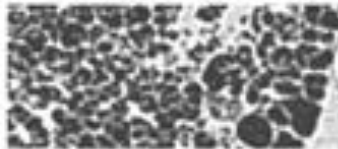
Emphysema= 1.5



GGO = 2



HoneyCombing=2.9



Consolidation=1.5



Epmphysema=2



GGO=1.8

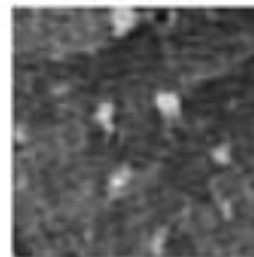


Figure 3.11 A comparison of Entropy values on two sets of ROIs of honey combing, consolidation, emphysema & GGO shows similar range of values

Haralick Feature 8: Sum Entropy =

$$-\sum_{i=2}^{2L} \sum_{i=0, |i-j|=i}^{L-1} \sum_{j=0, |i-j|=i}^{L-1} \phi_{ij} \log(\sum_{i=0}^{L-1} \sum_{j=0}^{L-1} \phi_{ij})$$

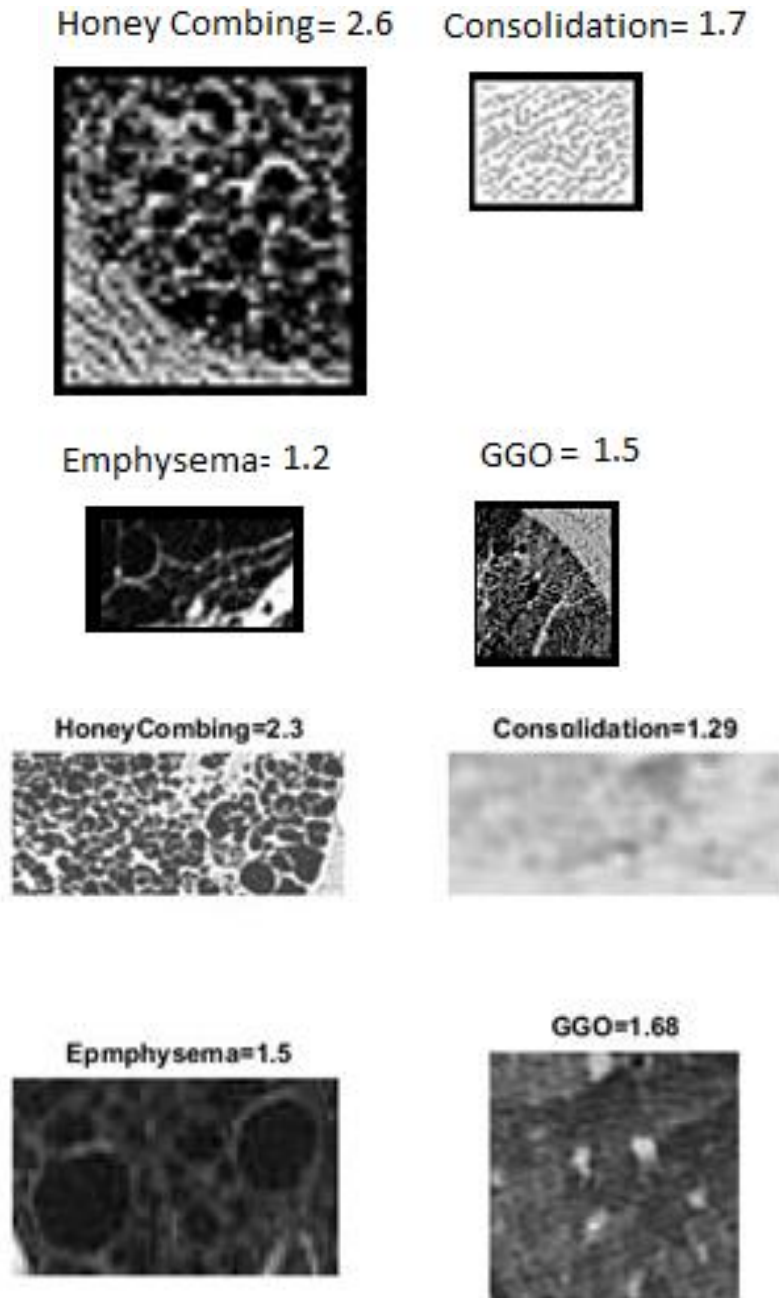
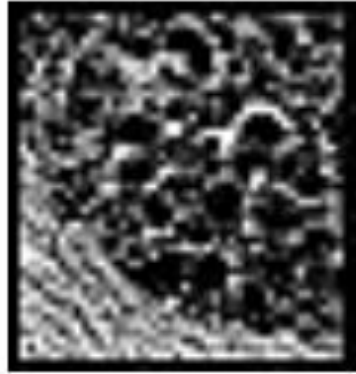


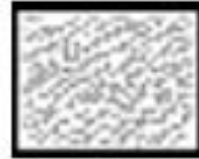
Figure 3.12 A comparison of Sum Entropy value on two sets of ROIs of honey combing, consolidation, emphysema & GGO shows similar range of values

Haralick Feature 9: Difference variance = $\sum_{|i-j|=0}^{L-1} (|i-j|)^2 \sum_{i=0}^{L-1} \sum_{j=0}^{L-1} \phi_{ij}$

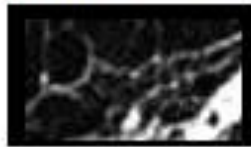
Honey Combing= 9.3



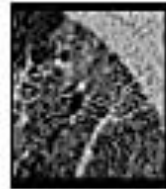
Consolidation= 1.1



Emphysema= 0.41



GGO = 0.64



HoneyCombing=1.08



Consolidation=0.31



Epmphysema=0.95



GGO=0.317

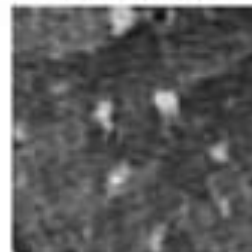


Figure 3.13 A comparison of Difference Variance on two sets of honey combing, consolidation, emphysema & GGO shows better results for consolidation as the range is much similar

Haralick Feature 10: Difference Entropy =

$$-\sum_{|i-j|=0}^{L-1} \sum_{i=0}^{L-1} \sum_{j=0}^{L-1} \phi_{ij} \log(\sum_{i=0}^{L-1} \sum_{j=0}^{L-1} \phi_{ij})$$

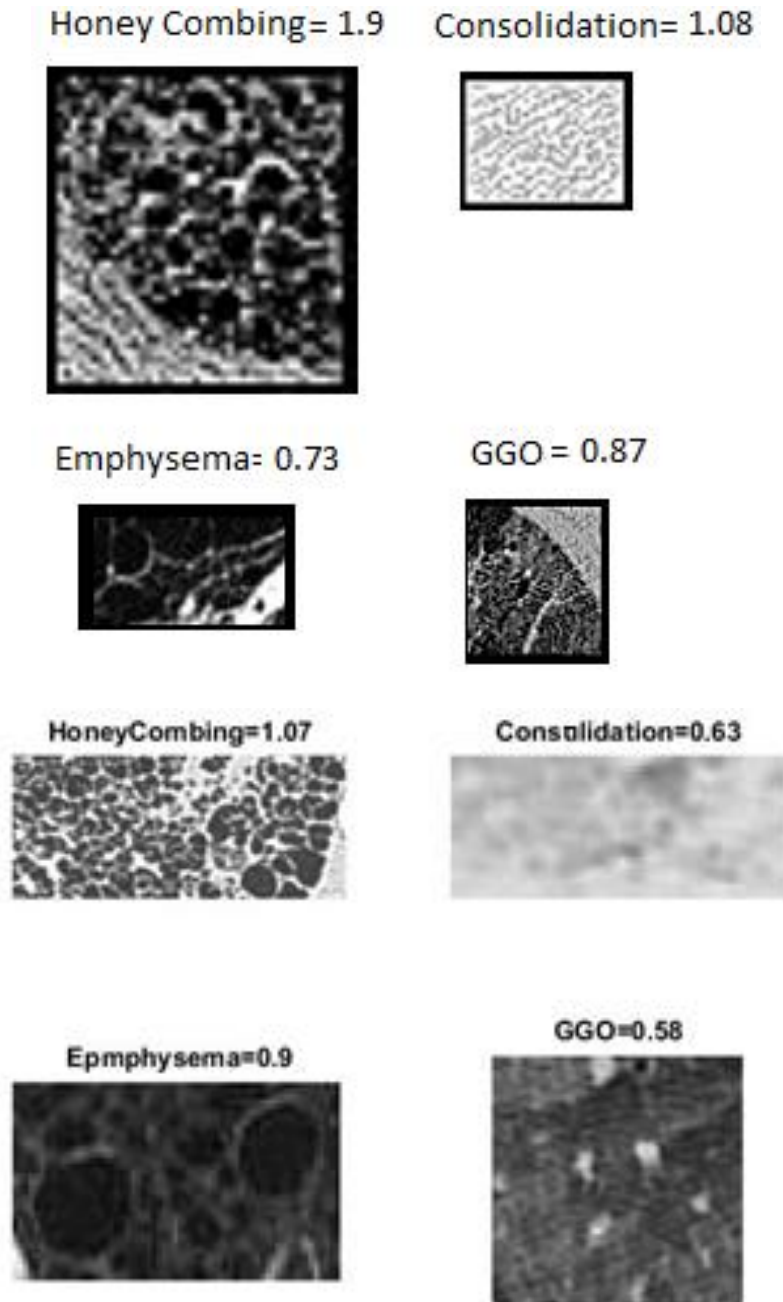


Figure 3.14 A comparison of Difference Entropy on two sets of ROIs of honey combing, consolidation, emphysema & GGO shows similar range of values

Haralick Feature 11: Sum Variance = $\sum_{i+j=0}^{2(L-1)} ((i + j) - \sum_{i+j=0}^{2(L-1)} (i +$

$$j) \sum_{i=0}^{L-1} \sum_{j=0}^{L-1} \phi_{ij})^2 \sum_{i=0}^{L-1} \sum_{j=0}^{L-1} \phi_{ij}$$

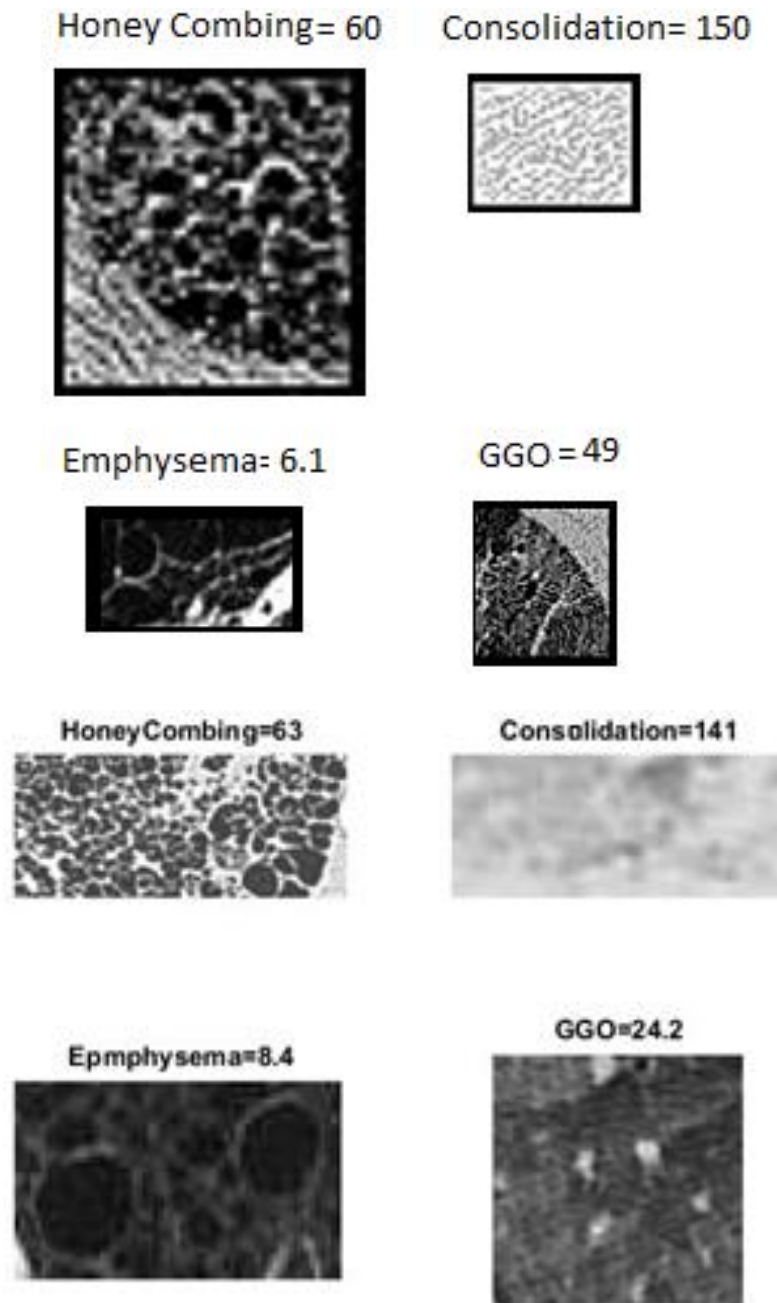
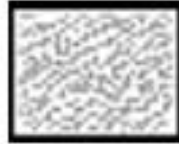
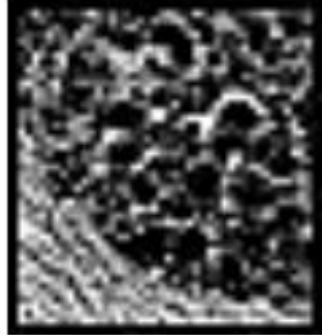


Figure 3.15 A comparison of Sum Variance on two sets of ROIs of honey combing, consolidation, emphysema & GGO

Haralick Feature 12: Information Measure of Correlation 1:

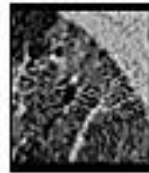
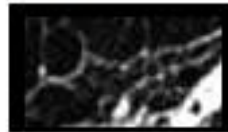
$$\frac{-\sum_{i=0}^{L-1} \sum_{j=0}^{L-1} \phi_{ij} \log(\phi_{ij}) - \sum_{i=0}^{L-1} \sum_{j=0}^{L-1} \phi_{ij} \log(\sum_{j=0}^{L-1} \phi_{ij} \sum_{i=0}^{L-1} \phi_{ij})}{\max\{\sum_{i=0}^{L-1} \sum_{j=0}^{L-1} \sum_{j=0}^{L-1} \phi_{ij} \log(\sum_{j=0}^{L-1} \phi_{ij}), \sum_{i=0}^{L-1} \sum_{j=0}^{L-1} \sum_{i=0}^{L-1} \phi_{ij} \log(\sum_{i=0}^{L-1} \phi_{ij})\}}$$

Honey Combing=0.034 Consolidation=-0.567



Emphysema=-0.088

GGO = -0.833



Honey Combing=-0.305

Consolidation=-0.203



Epmphysema=-0.138

GGO=-0.443

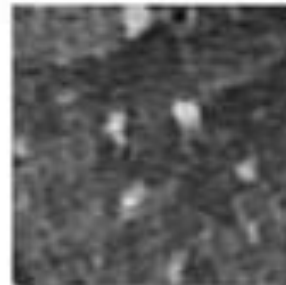
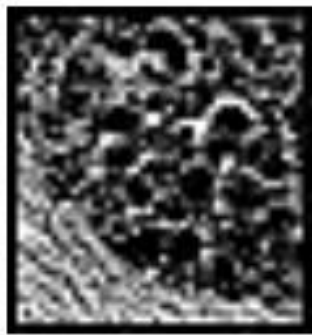


Figure 3.16 A comparison of Info. Measure of Correlation 1 on two sets of ROIs of honey combing, consolidation, emphysema & GGO

Haralick Feature 13: Information Measure of Correlation 2:

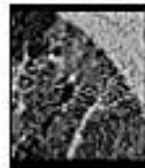
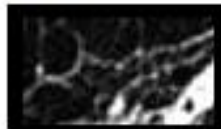
$$\left(1 - \exp \left[-2 \left(\sum_{i=0}^{L-1} \sum_{j=0}^{L-1} \sum_{k=0}^{L-1} \phi_{ij} \sum_{i=0}^{L-1} \phi_{ij} \log \left(\sum_{j=0}^{L-1} \phi_{ij} \sum_{i=0}^{L-1} \phi_{ij} \right) + \sum_{i=0}^{L-1} \sum_{j=0}^{L-1} \phi_{ij} \log(\phi_{ij}) \right) \right] \right)^{1/2}$$

Honey Combing=0.359 Consolidation=0.361



Emphysema= 0.369

GGO = 0.4



HoneyCombing=0.809

Consolidation=0.543



Epmphysema=0.513

GGO=0.81

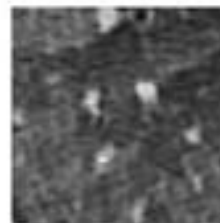
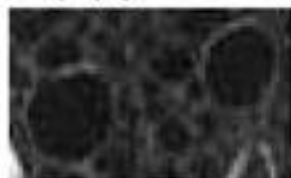


Figure 3.17 A comparison of Info. Measure of Correlation 2 on two sets of ROIs of honey combing, consolidation, emphysema & GGO shows similar range of values

E. Gabor Filter Analysis

Gabor filter is a sinusoidal function of frequency and orientation that is widely used for extracting texture features in frequency and spatial domain^{112,113}. In the spatial domain, a 2D Gabor filter is a Gaussian kernel function modulated by a sinewave function. It has been suggested that processing of images using Gabor filters is similar to the perception in the human visual system^{114,115}.

The Gabor filter is computed as follows¹¹⁶:

1. Fourier transform of the image ROI is calculated
2. The result is multiplied with the Gaussian function centered at different frequencies.
- 3 Inverse fast Fourier transform (IFFT) of each output of step 2 is computed

Using different frequencies and orientation, 2D Gabor filter is used to extract texture features from CT images of the lung.

$$G(x, y) = e^{-\frac{(x-x_0)^2}{2\sigma_x^2} - \frac{(y-y_0)^2}{2\sigma_y^2}} e^{j(\omega_{x_0}x + \omega_{y_0}y)}$$

Where $\omega_{x_0}x, \omega_{y_0}y$ are the maximum center frequencies responses in x and y directions; σ_x, σ_y are standard deviations in both directions and x, y are pixel positions in the image.

In our analysis we have chosen 18 orientations ($\Delta\theta = \frac{360}{20} = 18$). The centre of frequency f can be computed as

$$p_f = \frac{\omega_f + \omega_{f-1}}{2} = \frac{1}{2}(2^i\omega_0 - 2^{i-1}\omega_0) = 2^{i-1}.3\omega_0$$

For each ROI, a total of 72 Gabor filters (18 orientations and 4 frequencies) are computed as shown in figures 3.18 and 3.19. Applying these filters on a ROI results in filtered image

with enhanced edges of the same Gabor orientation. For instance, when orientation is 90° and 180° the edges on the horizontal and vertical directions will be enhanced based on four frequencies, consecutively.

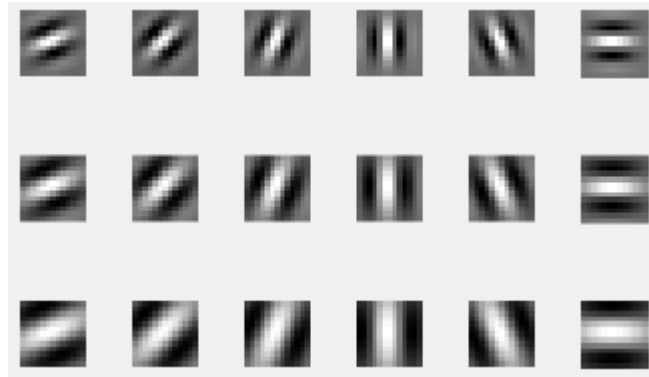


Figure 3.18 Eighteen orientations of Gabor filter, used for feature extraction; each differing from each other by 20 degrees

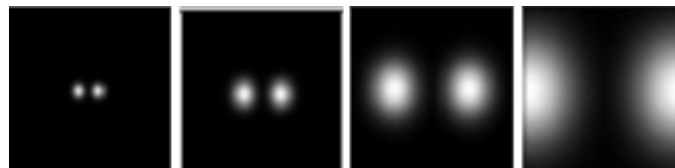


Figure 3.19 Four frequencies applied to each orientation for Gabor feature extraction

Inverse Fast Fourier Transform (IFFT), texture energy and transformed IFFT are the texture features extracted from Gabor filters applied to an image ROI. To extract these features first one computes the Fourier transform conversion, then convolves it based on Gabor filter and finally inverse the convolved image. This feature is assessed differently, compared to Haralick energy feature.

Fourier transform (FT) maps signals to their component frequencies; the discrete FT is computed as F , with variables p, q for an image of size $M \times N$

$$F(p, q) = \sum_{x=0}^{M-1} \sum_{y=0}^{N-1} f(x, y) e^{-2\pi j \left[\frac{px}{M} + \frac{qy}{N} \right]}$$

where $p = 0, 1, 2, \dots, M - 1$ and $q = 0, 1, 2, \dots, n - 1$ and $f(x, y)$ are pixel values

The result of convolution between FT of a lung CT image and Gabor filter can be computed by fast Fourier transform multiplication of two convolved images.

To inverse back the convolved image from a FT (with complex numbers), IFFT is required; which is used as a texture feature too. IFFT is calculated as

$$f(x, y) = \frac{1}{MN} \sum_{p=0}^{M-1} \sum_{q=0}^{N-1} F(p, q) e^{2\pi j \left[\frac{px}{M} + \frac{qy}{N} \right]}.$$

Extraction of texture energy is done by taking the positive signs of square of IFFT value.

Transformation of IFFT as the third texture feature, refers to the absolute value of IFFT which can be obtained by

$$\varphi(g) = \left| \frac{1 - e^{-2\alpha g}}{1 + e^{-2\alpha g}} \right|, \alpha = 2.5$$

where g is the gray value of IFFT image.

To obtain inverse FT images, following steps were followed:

1. Calculate FFT of the original ROI
2. Gabor filter is applied to the original image incorporating 18 filters
3. FFT of each Gabor filter in step 2 are calculated
4. Convolution of step 1 and step 3 is evaluated
5. IFFT of step 4 is performed
6. All IFFT's in step 5 are summed up

The classification results of each Gabor feature is demonstrated in section IV. This section will show, combination of these features yields in a better classification accuracy than using them separately.

F. Geometric Quantification based on Minkowski Functionals

Minkowski Functionals (MF) play a crucial role in integral geometry and analyzes spatial structure of a surface. Minkowski functions compute geometrically oriented features from 2-D images and provide a morphological assessment and descriptor of a ROI. There are three primary functions for a 2-D image that can be computed using MF: area, contour length and Euler characteristics. On a graph of connected dots where the lines does not intersect Euler characteristics is $V-E+F=2$. In this theory, V is the number of vertices (dots), E is the number of Edges (connections) and F is the number of regions (faces). For instance, with Euler characteristics one can distinguish a circle from a donut shape disk, where the first image has a hole and the other does not. In this section, computational analysis of MF is demonstrated. Appendix II provides more theoretical information^{121,122,123}.

MF can be used as texture features in medical image analysis for the segmentation and detection of pathology. These features are motion (translation and rotation) invariant, continuous and additive, however, spatial heterogeneity of structures cannot be assessed because two different images can have the same Functional values. Although such geometric quantification has the above drawback, it is a useful analytical tool for selected ROI's where shape detection is crucial. The differences between reticulation versus honeycombing and emphysema versus cyst are well detected using these features¹²³.

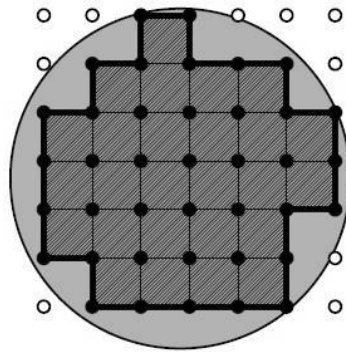


Figure 3.20 Measuring perimeter of a polygon with Minkowski Functionals

Calculating these features based on MF is not trivial. For instance, measuring the perimeter according to Figure 3.20 is not simply counting the number of pixels. It is based on the configuration of the pattern as well. Connected components in binary image also add up to the complexity of this type of measurement. A polygonal reconstruction is analysed by measuring perimeter through joining adjacent pixels and calculating the total length of edges. The perimeter of this disk is the perimeter of the square with the same diameter which may have up to 25% error.

To compute MF features^{121,122}, image is binarized and partitioned into overlapping patches of size 2×2 and then histograms are measured. Matrices below are patch possibilities, i.e. 4 adjacent pixels are all zeros, or ones, or one of them is 1 and so on; using local binary patterns. Different neighbourhood possibilities are shown with $Q_x, x = 1,2,3,4$ and D .

$$Q_0 = \begin{bmatrix} 0 & 0 \\ 0 & 0 \end{bmatrix}, Q_1 = \begin{bmatrix} 1 & 0 \\ 0 & 0 \end{bmatrix}, Q_2 = \begin{bmatrix} 1 & 1 \\ 0 & 0 \end{bmatrix}, Q_3 = \begin{bmatrix} 1 & 1 \\ 1 & 0 \end{bmatrix}, Q_4 = \begin{bmatrix} 1 & 1 \\ 1 & 1 \end{bmatrix}, Q_D = \begin{bmatrix} 1 & 0 \\ 0 & 1 \end{bmatrix}.$$

To find the area of a particular object which has texture differences, using above patches, one can identify active pixels in a 2×2 neighbourhood based on below assessment

$$Area = \frac{Q_1 + 2Q_2 + 2Q_D + 3Q_3 + 4Q_4}{4}.$$

In above formulas, Q_1 could have 3 more similar patches with 1 in each corner; 1 representing an active pixel in the binarized image. The reason for the coefficients beside the number of tiles is the number of active pixels. For instance to measure the area, Q_2 has a coefficient 2, meaning that if such patch is found, there were 2 pixels involved which should be added in the assessment. And the reason for division by zero for area is to take overlapping tiles into account.

MF count the number of active contours using above patches based on below formula

$$Contour Length = Q_1 + Q_2 + 2Q_D + Q_3$$

The number of active contour length for all patches is 1, however, Q_D has two, therefore a coefficient is used in above formula.

$$Q_D = \begin{bmatrix} 1 & 0 \\ 0 & 1 \end{bmatrix}.$$

As mentioned earlier, MF are biased. The reason is because of the process of transforming images to binary. The biased estimate of area and contour length is more obvious when a shape is discretized on a continuance shape like a circle on a grid.

To make these calculations less bias we use below formulas^{121,122}:

$$Area = \frac{1}{8}Q_1 + \frac{1}{4}Q_2 + \frac{1}{4}Q_D + \frac{7}{8}Q_3 + Q_4$$

$$Contour Length = Q_2 + \frac{1}{\sqrt{2}}(Q_1 + 2Q_D + Q_3).$$

Euler characteristics is a connectivity measurement based on the difference of connected components and the number of holes (faces). Non-overlapping vertices, edges and

polygonal faces will be reconstructed and approximated based on different types of connectivity; 4-neighbours and 8-neighbours. Euler characteristic is

$$E = \frac{1}{2\pi} \int k(x) dx$$

where $k(x)$ is the curvature. Convex polygonal reconstruction is based on 4 adjacency in 2D images which only takes horizontal and vertical neighbours. These cells are either a vertex, edge or a face, parallel to the direction of the grid. In Figure 3.21, a 3x3 neighbourhood of pixels is presented which is decomposed into tiles that are also presented in this figure. The numbers on the edges and vertices, demonstrate the number of tiles they belong to. For instance, the central pixel belongs to four tiles.

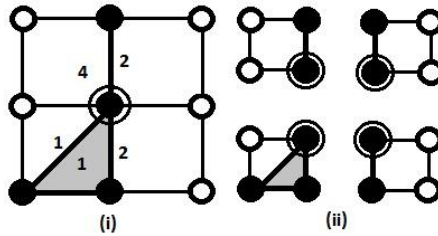


Figure 3.21 i) pixel neighbourhood of 3x3, ii) 4 tiles of 2x2

And Euler characteristics can be derived based on 4 or 8 neighbourhoods. The formulas are both biased, but in different directions, so it makes sense to take the average of the two

$$x^{(4)} = \frac{Q_1 + 2Q_D - Q_3}{4}$$

$$x^{(8)} = \frac{Q_1 - 2Q_D - Q_3}{4}$$

Less biased version of Euler characteristics would be

$$x = \frac{Q_1 - Q_3}{4}$$

Q_1 is the number of single pixels in 4 or 8 neighbourhoods, which contributes to the calculation of the number of pixels for an edge. Q_2 is also similar, but in the diagonal direction. However, we are not looking for X shape edge in either of our DLD patterns. It will make sense to add the pixels on diagonal when the neighbourhood is tight, but with 8 pixel neighbourhood it distracts the shape detection process towards a meaningless pattern. Omitting this patch from the final, less biased, version of Euler characteristics is for that reason. Q_3 Counts the number of vertices, or connective points in the binarized image, which is decremented from the number of faces and edges in Euler formula $E-V+F$. As an example, MF is calculated on CT image of the lung detected with honeycombing pattern in figure 3.22.



Figure 3.22 the selected areas on the lower lobe of both lungs show honeycombing

Figure 3.23 is a ROI taken from left lower lobe of the lung in figure 3.22. Area, contour length and Euler characteristic are calculated for this ROI.

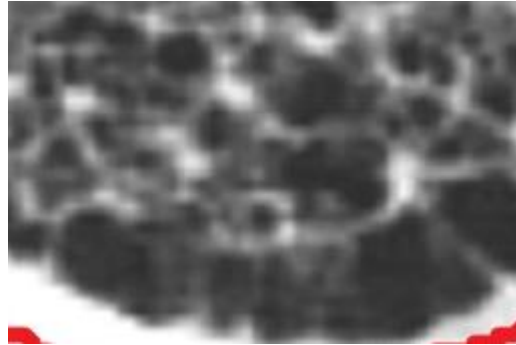


Figure 3.23 Honey combing ROI from a lower lobe left lung

First, the ROI is binarized to be able to assess MF. The binarization process is based on pixel value thresholding. To decide on the threshold, the mean gray level value is computed, which is 104 for this ROI. Second, one calculates the threshold based on 27% of the mean GLV which is evaluated experimentally. The binarized image is shown in figure 3.24.

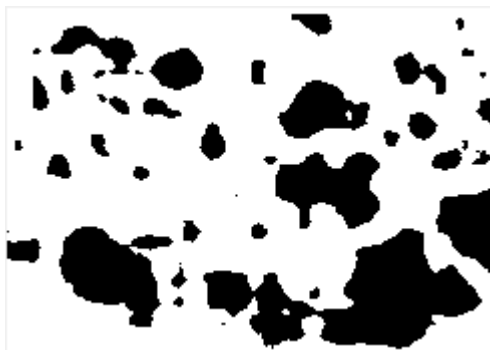


Figure 3.24 Binarized version of a honeycombing ROI

Now, based on the patches described earlier ($Q_0, Q_1, Q_2, Q_3, Q_4, Q_D$) area, contour length and Euler characteristics are evaluated.

III. Processing of Labelled CT Image Data and Training of the ANN

Pattern classification being the central theme of this thesis, algorithms for characterizing texture in ROIs from CT images of the lung were set up using features described in chapter

2. The ROIs were selected from each image. The number of classes affects the classification accuracy of any classifier. Ideally, features should be uncorrelated and information overlap between features is minimal. Large number of ROI's (in several hundreds) are needed for any classification project. For the backpropagation algorithm, presence of a large number of data points will sharpen and enhance class boundaries.

Classifiers based on support vector machine (SVM) and K-nearest neighbour algorithm are often used in CT image classification problems, especially those of DLD patterns. However, because they use distance functions to make a linear/non-linear relationships between data, classification accuracy is affected in a negative way; especially when the data set is as large as the one described in this thesis, especially with eleven classes involved. On the other hand, ANN is not limited to heterogeneity (it can have different scales), it can handle large amount of data with its underlying non-linear assessment of the relationships and it has shown higher performance with larger number of outputs (number of classes). For more information on ANN, SVM and k-Nearest, refer to Appendix III.

Training an ANN based on back-propagation technique requires several thousands of iterations so that class boundaries are adequately formed. There were 229 patients in the data sets whose CT images were available for analysis. From these images a total number of 1165 ROIs were extracted, which means, multiple ROI were extracted from each patient's data. The ANN was trained based on 1165 ROI's which approximately ran through 12550 iterations for training each combination of classes, with 1 hidden layer and 10 neurons.

Class	No. of Patients	No. of ROI's
Consolidation	19	112
Emphysema	27	150
GGO	42	230
Honey Combing	32	141
Cyst	18	82
Fibrosis	16	38
Nodularity	21	173
Reticulation	16	45
Scar	11	25
Tree-in-bud	7	19
Healthy	20	150
Total	229	1165

Table 3.1 Number of patients and ROI's per class

The ANN inputs are vectors of the size equal to the number of features extracted based on the methods described in each chapter and the output neurons are defined based on 10 DLD patterns and an output neuron specifically for healthy ROI's. Individual number of patients and ROI's for each pathology is listed in the Table 3.1.

Number of extracted features for each texture method are as follows: Tamura = 3; CLBP = 13; GLCM = 13; Haralick = 13; Gabor = 3; MF = 3.

Classification accuracy, specificity and sensitivities of texture methods and their combinations are provided for all features in chapter 3. Classification results in Chapter 3, 4 and 5 are based on leave-one-out method, and chapter 6 provides an additional validation method namely using 5-fold, to conclude the classification results obtained in the research presented in this thesis.

At the end of chapters 3, 4, 5 and 6 classification accuracy is presented through several tables with a format shown in Table 3.2.

Abnormality							
GGO	A ₁	A ₂	A ₃	A ₇		A ₁₂	
Consolidation				A ₈			A ₁₃
Scar				A ₁₁			
Cyst			A ₄	A ₉	A ₁₀	A ₁₅	
Emphysema							A ₂₂
Reticulation		A ₁₇					
HoneyCombing			A ₁₈				
Fibrosis		A ₁₉					
Nodularity			A ₂₀				
Tree in bud		A ₂₁					

Table 3.2 An example of ANN average classification accuracy for any general feature

The right most column (A₁₂-A₂₁) demonstrates average percentage classification accuracy for each DLD compared to a healthy lung. For instance A₁₂ is percentage classification accuracy when comparing GGO (row 1) with healthy lung. The A₁₃ is the percentage classification when healthy lung is compared to consolidation pathology. The A₁₄ is the percentage classification accuracy when healthy lung is compared to scars. In the next column of the table, A₁₁ is classification accuracy of cyst, emphysema, reticulation, honey combing, fibrosis and healthy lung. A₂ is classification accuracy of the first five patterns

and healthy lung. A_3 is the classification accuracy of GGO, consolidation, scar and healthy lung. A_1 is classification accuracy when all 10 patterns and healthy lung that were trained on ANN and classified based on leave-one-out (chapters 3, 4 and 5) or 5-fold cross methods (chapter 6). Classification accuracy could not be presented for every combination of lung diseases studied in this thesis and therefore, classification accuracies are provided for interesting combination of pathologies. A similar table is presented in each of the subsequent chapters.

IV. Classification Accuracy of Feature Sets Derived From Various Texture Analysis Methods

Tables 3.3 to 3.15 present results of comparing classification accuracy based on all texture features described thus far for each disease and their combinations. Although not mentioned, but it is implicit that, every column, either with one or more rows, considers classification accuracy for at least one DLD pattern and normal healthy lung ROI.

CT images of patients with DLD diseases have rich-characteristic patterns which differ from each other. However, a single feature extraction method is unlikely to yield the best set of features. In order to have an array of features which are rich with information, multiple feature generation methods have been incorporated in this thesis. It is also anticipated that a combination of these features will increase the accuracy of classification.

Table 3.3 demonstrates the classification accuracy based on leave-one-out method using only coarseness feature of Tamura. Coarseness is a well-defined feature for analysing most of the DLD patterns, but these pathologies are very complex for only one feature to produce high classification accuracy. Some of the patterns such as fibrosis, reticulation and

honeycombing are classified with a higher accuracy because inherent disease process have higher effect on the coarseness of the image. The reason classification accuracy of reticulation is higher than fibrosis and honeycombing is because, coarseness cannot identify the circular patterns of honeycombing pathology. Table 3.3 shows that scar is not well recognized by Tamura coarseness feature and yields the least classification accuracy at 37% while reticulation has the highest result at 67.4%.

Abnormality								
GGO	26.3%	35%	44%	48%		58%		
Consolidation							49.2%	
Scar							37%	
Cyst			60%	51%		65.1%		
Emphysema							59%	
Reticulation		34%	57%	56%	46%	67.4%		
HoneyCombing				57%		66.3%		
Fibrosis							66.9%	
Nodularity			53%					64.2%
Tree in bud								53.7%

Table 3.3 ANN average classification accuracy based on coarseness, Tamura texture method

Table 3.4 demonstrates classification accuracy of another Tamura feature Contrast. Contrast has lower classification accuracy compared to coarseness. However, the highest and lowest accuracies belong to the same classes (reticulation and scar) with this feature as well.

Abnormality							
GGO	22.2%	31%	41.3%	46.5%		55.2%	
Consolidation							47.1%
Scar							36.3%
Cyst			55.1%	48.8%		59.9%	
Emphysema						56.1%	
Reticulation		30%		56.2%	55.9%	44.2%	64.8%
HoneyCombing			56.1%		63%		
Fibrosis						63.6%	
Nodularity			52%			60%	
Tree in bud						50.4%	

Table 3.4 ANN average classification accuracy based on Tamura’s contrast feature

Table 3.5 shows classification accuracy of Tamura-directionality feature. The accuracy of this feature is lower than coarseness and contrast. The classification accuracy of eleven classes with directionality is 19.1% which is 7.2% and 3.1% less compared to coarseness and contrast features of Tamura, respectively.

Abnormality							
GGO	19.1%	23%	37.6%	43%		46.7%	
Consolidation							47.3%
Scar							27.2%
Cyst			51%	39.25%		49%	
Emphysema						50.2%	
Reticulation		25%		46.8%	49%	39.3%	56.2%
HoneyCombing			49.6%		55%		
Fibrosis						56.6%	
Nodularity			41.5%			41%	
Tree in bud						44%	

Table 3.5 ANN average classification accuracy based on directionality, Tamura texture method

Abnormality								
GGO	27.8%	42%	55%	70.98%		80.45%		
Consolidation							81%	
Scar					59.6%		72.3%	
Cyst			61%			41%	78%	
Emphysema				79%				
Reticulation		37%	46.7%	62.2%		63%	80%	
HoneyCombing							41%	80.2%
Fibrosis								80.25%
Nodularity			49.75%					72.9%
Tree in bud								71.1%

Table 3.6 ANN average classification accuracy based on all three Tamura texture features shows better results compared to when only one of the features were used

The combination of Tamura features demonstrated in table 3.6 shows an increase in classification accuracy of any number of pathological patterns. The highest accuracy classification accuracy pertains to images from patients with consolidation pathology (81%) and the lowest classification accuracy belongs to images from patients with scar at 72%.

Table 3.7 demonstrates classification accuracy of CLBP using ANN. The classification accuracies of each combination of classes is comparable to individual Tamura features. But the combination of Tamura features provides a higher classification accuracy. The lowest accuracy when classifying two classes with all Tamura features is 71.1%. However, for the same class (Tree in Bud), CLBP's accuracy is 59%, and the lowest accuracy belongs to scar with 38.9%.

Abnormality								
GGO	22%	29%	39%	44%		56.3%		
Consolidation							46.8%	
Scar							38.9%	
Cyst		31%	49%	43.5%		39.4%	59%	
Emphysema							61.3%	
Reticulation				58%			62.8%	
HoneyCombing					54.9%		63%	
Fibrosis							63.8%	
Nodularity			44%					68.8%
Tree in bud								59%

Table 3.7 ANN average classification accuracy based on Compound Local Binary Pattern (CLBP) algorithm

Table 3.8 shows classification accuracy of GLCM features. The accuracy of this method is higher than GLCM, but slightly lower than combined Tamura features. When classifying eleven classes, GLCM’s accuracy is 1.6% higher than CLBP, and 4.2% less than Tamura. The lowest classification accuracies with this method belong to tree in bud and scar with about 67%.

Abnormality								
GGO	23.6%	38%	53%	68%		72.3%		
Consolidation							73.1%	
Scar							67.7%	
Cyst		35%	58%	57%		37%	74.2%	
Emphysema							75.9%	
Reticulation				58%			72.8%	
HoneyCombing					60%		76%	
Fibrosis							74%	
Nodularity			47%					71%
Tree in bud								67%

Table 3.8 ANN average classification accuracy based on Gray Level Co-Occurrence Matrix (GLCM) shows better results compared to single Tamura features

Table 3.9 demonstrates classification accuracies of different combination of classes using all Haralick features. The results shows the highest accuracy among all other features, with any number of classes involved. The classification of eleven classes is 2% higher than Tamura features.

Abnormality						
GGO	29.8%	44%	57%	72.98%		82.45%
Consolidation				60.6%	83%	
Scar			74.3%			
Cyst			63%		80%	
Emphysema				81%		
Reticulation		39%	48.7%	64.2%	44%	81.3%
HoneyCombing				65%		81%
Fibrosis			51.75%	80%		
Nodularity				74.9%		
Tree in bud				73.1%		

Table 3.9 ANN average classification accuracy based on all thirteen Haralick texture features shows highest classification compared to all other methods

Tables 3.10 to 3.11, demonstrate individual classification accuracies of each Gabor filter features (IFFT, energy and transformed IFFT). Table 3.12 shows the classification results when all these features are combined. As experienced with Haralick and Tamura, it is expected that their combination will increase the accuracy.

Abnormality						
GGO	17.5%	24%	34.6%	40%		48%
Consolidation				35%	40.4%	
Scar			30.9%			
Cyst			36%		56%	
Emphysema		53.2%				
Reticulation		22%	35%	48.7%	26%	58.7%
HoneyCombing				40.9%		58.8%

Fibrosis						58.1%
Nodularity			40%			53.3%
Tree in bud						44%

Table 3.10 ANN average classification accuracy based on IFFT, Gabor filter method

Abnormality								
GGO	15.7%	22%	31%	37%	23%	45%		
Consolidation							37.6%	
Scar						28%		
Cyst			33%	32%			51.6%	
Emphysema								48.9%
Reticulation		21%		34%	43%		52.4%	
HoneyCombing						37%		51.2%
Fibrosis							51.9%	
Nodularity				35%				50.2%
Tree in bud								42.4%

Table 3.11 ANN classification accuracy based on texture energy feature using Gabor filter

Abnormality								
GGO	18.9%	27%	37%	41%	28.2%	50.2%		
Consolidation							43%	
Scar						34.4%		
Cyst			40%	38%			57%	
Emphysema								53.9%
Reticulation		26%		39%	50%		59.8%	
HoneyCombing						47%		60.3%
Fibrosis							60.1%	
Nodularity				45%				56%
Tree in bud								49.4%

Table 3.12 ANN average classification accuracy based on transformed IFFT, Gabor filter method

Table 3.13 shows the classification accuracy of IFFT, energy and transformed IFFT features based on Gabor filter and validated based on leave-one-out method. The

combination of these features has higher classification accuracy than any individual Gabor features.

Abnormality							
GGO	26.3%	37%	48%	50%		59.9%	
Consolidation							57.6%
Scar					44%	49.8%	
Cyst			50%			65.2%	
Emphysema						64.6%	
Reticulation		39%	47%	56%	39%		70.4%
HoneyCombing							72%
Fibrosis				57%			69.9%
Nodularity							60.7%
Tree in bud				52%			55%

Table 3.13 ANN average classification accuracy based on all three Gabor filter texture features shows higher classification results than when only one of the feature was used

Table 3.14 demonstrates classification results based on the MF described in this chapter. The highest classification accuracy for two classes using MF is 51.1%. the lowest rests are associated with scar and consolidation.

Abnormality							
GGO	14.2%	20.7%	29%	35%		44.2%	
Consolidation							36.9%
Scar					31.8%	26.4%	
Cyst			32%			44.2%	
Emphysema						50.9%	
Reticulation		19.8%	33%	41%	29%		51.1%
HoneyCombing							49.9%
Fibrosis				35%			48%
Nodularity							49.3%
Tree in bud				34%			41%

Table 3.14 ANN average classification accuracy based on Minkowski’s geometric Functionals

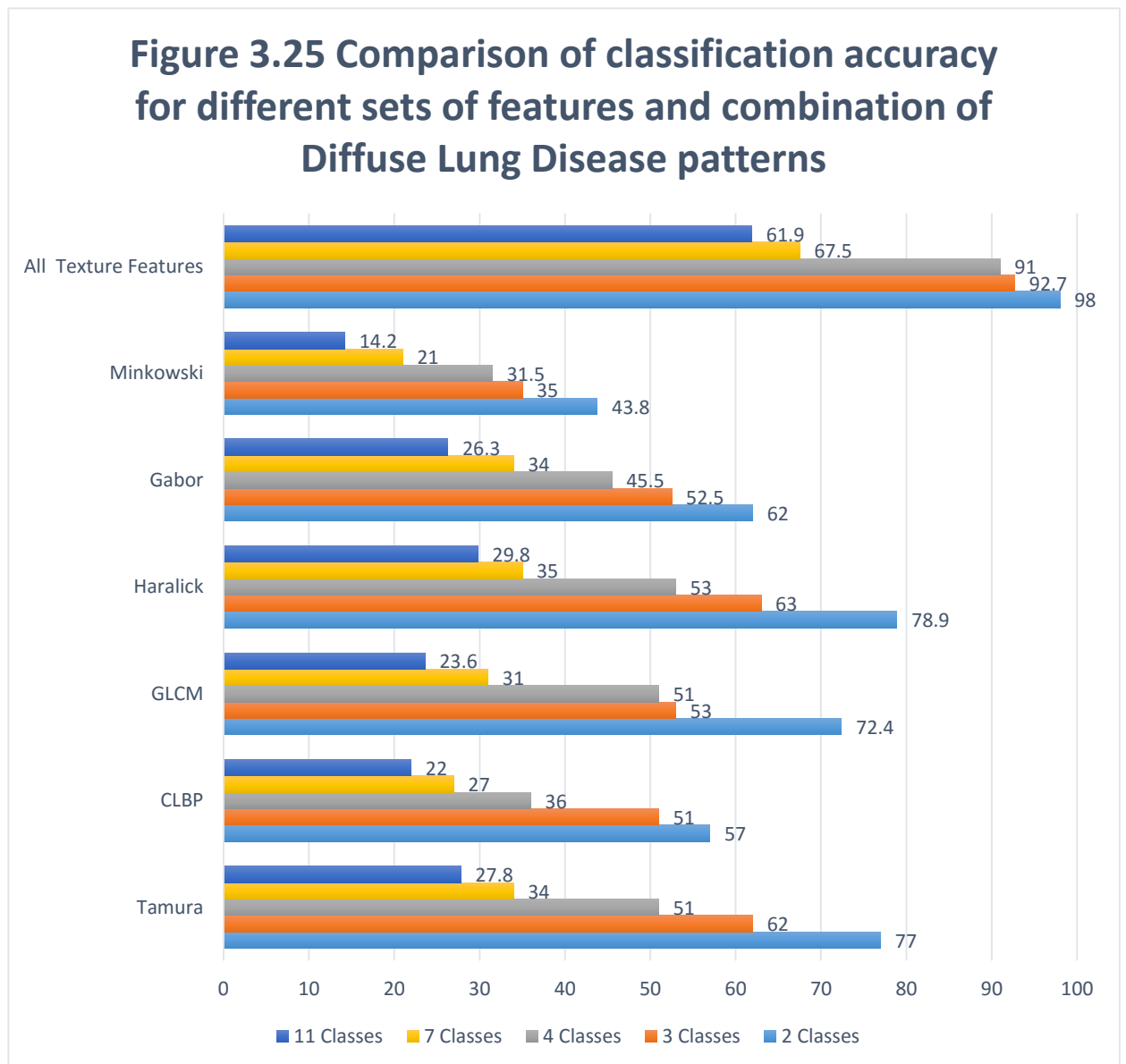
Abnormality								
GGO	61.9%	77.6%	90.5%	93.3%		98.2%		
Consolidation							99.1%	
Scar								
Cyst			90.2%			97.8%		
Emphysema				93.1%			98.2%	
Reticulation		74%	94%	95%	83.7%		99.9%	
HoneyCombing						99.9%		
Fibrosis				91%				
Nodularity								94%
Tree in bud				92.9%				

Table 3.15 ANN average classification accuracy based on all texture features

All texture features demonstrated in this chapter are combined in table 3.15 to show average classification accuracy based on different combination of irregularities. Training with a set of uncorrelated well descriptive features results in higher accuracy. Especially when number of classes is higher. The effect of feature combination is more vivid. Classification accuracies approach a 100% for most classes when compared to healthy lung; except tree in bud, nodularity, scar and cyst; which are still over 94%. The reason these classes showed lower accuracy is because of the lower number of ROI's available for classification. And in the case of nodularity, the complexity of differentiating between nodules and blood vessels with texture methods may have resulted a lower accuracy. To be able to compare blood vessels with nodules, the algorithm must be able to trace the location of the ROI among the higher and lower cross sectional images of the lung. If there is a continuity, the bright spot is due to a vessel. The methods presented in this thesis has focused on feature extraction rather than segmentation.

V. Results

Figure 3.25 shows classification accuracies for multiple texture features. The classification accuracy drops when the number of classes increases irrespective of features used. Features with the least accuracy at the time of classifying only two classes, had the lowest accuracy among other features when more classes were involved.



According to this bar graph, Haralick features are the most useful statistical descriptors of all features, resulting in an accuracy of 78.9% for two classes and 63% for three classes. Results based on Tamura features are closely behind at 77% and 62 percent for two and three classes respectively. The accuracy drops below 50% especially when more than four classes are present in each method. The least descriptive of all features is due to Minkowski functionals.

The order of the highest to lowest accuracies for texture features are as follows: Haralick, Tamura, GLCM, Gabor, CLBP and MF. The accuracies for any number of classes is higher with the strongest features, however, with 7 classes. Both Tamura and Gabor had the same accuracy of 34% with 4 classes. Also Tamura and GLCM had the same average accuracy of 51%.

When all features are combined the highest accuracy of classification is achieved (98% for two classes, 92% for three and 61.9% for eleven classes).

The specificity and sensitivity of all texture features in the presence of two, three and eleven classes were evaluated and results are demonstrated in Table 3.16.

Validation	Two classes	Three Classes	Eleven classes
<i>Specificity</i>	97.95%	90%	78.9%
<i>Sensitivity</i>	98%	94%	71.6%

Table 3.16 Specificity and sensitivity of all Texture features based on 2, 3 and 11 classes

Although classes were known so far in analysis provided above and leave-one-out method was used to evaluate the accuracy, chapter 6 will demonstrates analysis based 5-fold validation.

VI. Chapter Summary

This chapter provide a detailed description and formulae developed by Tamura, CBLP, GLCM, Haralick, Gabor and Minkowski Functionals to investigate and extract features from DLD patterns of CT images of the lung. The process of extracting these features has been illustrated using several sample CT images. Values extracted based on each method are listed and compared with a number of different patterns. Training and classification accuracies using a combination of features classified through ANN are presented. Classification accuracies are presented for ten different pathologies/classes using ANN based on texture features and several combinations. Accuracies, specificity and sensitivity are also provided based on the combination of these features. Our results show that the accuracy increases when all texture features are combined for any number of classes.

To conclude, combined texture features yield the highest accuracy of classification and Minkowski Functionals yields the lowest classification accuracy. Features based on Haralick, Tamura and GLCM descriptors have proven to be most effective features. The classification accuracy is reduced when the number of classes increases. These results are similar to the state-of-the art when comparing up to 6 classes. In addition, texture features of various kinds permit classification of 10 disease categories, with normal image data from healthy adults being a separate class.

CHAPTER 4

CLASSIFICATION OF CT IMAGES OF THE LUNG USING FRACTIONAL DIMENSIONAL ANALYSIS

I.	Introduction	101
II.	Mathematical preliminaries.....	101
A.	Segmentation-based Fractal Texture Analysis	105
B.	Box Counting Algorithm	107
C.	Fractal Dimension Semi Variance Feature extraction Technique	108
III.	Accuracy of Classification of CT Image of The Lung Based on Fractal Features 110	
IV.	Classification Accuracies of The Combination of Texture and Fractal Features .	113
V.	Results	114
VI.	Chapter Summary.....	116

I. Introduction

In chapter 2, a descriptive approach to fractal analysis has been provided. In practice, many types of biomedical images are generated due to self-similar structures, and fractal analysis can characterise such images. In order to obtain relevant features from fractal analysis, a mathematical and theoretical framework is presented in this chapter.

Statistical texture analysis of CT images of the lung characterizes the gray level distribution within the images, quite well. However, fractal based image processing has proved to be useful in advancing the field of automated image analysis. In this chapter fractal dimensional analysis is performed based on three methods and their extracted features will be added to texture features discussed in the previous chapter. Since fractal information about an image is not necessarily correlated with statistical nature of the image, it could improve the classification results.

II. Mathematical preliminaries

To have a better description of dimension, consider a line with a unit length, according to figure 4.1. If it gets tripled, its size becomes $3^1 = 3$. For a square with the same length size, tripling it, will result in a bigger square; $3^2 = 9$. Tripling a cube generates a cube with square size $3^3 = 27$. This pattern satisfies $X = A^d$, where X is the number of objects, A is the scaling factor and d is the dimension¹²⁵.

The resulting shapes are similar in these cases but when changing the scale of a circle or cone, the shape would have been different because one cannot make a bigger circle that is made up of circles.

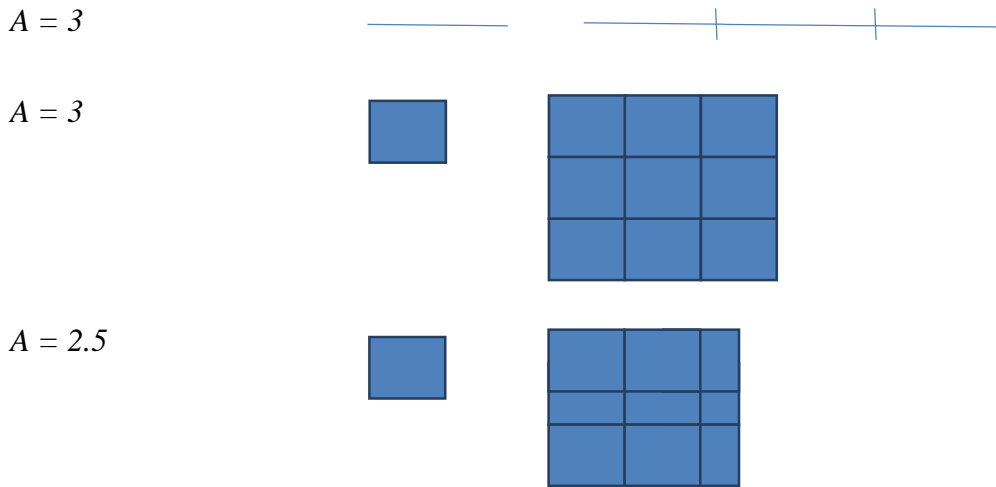


Figure 4.1 The line and the first square are made up of scales equal to 3 and the last square's scaling factor is 2.5

Dimension remained an integer, but what if $d = \frac{\log x}{\log A}$ in the above equation was not an integer? Koch's snowflakes¹²⁵ are examples of a figure with a non-integer dimension. Beginning with an equilateral triangle, and adding an equilateral triangle to each side of it to make a length of $4/3$, we will end up with a shape depicted below that has an infinite boundary length, and an area of $\frac{\sqrt{3}}{4} + \frac{\sqrt{3}}{4} \left(\frac{1}{3} + \frac{4}{3^3} + \frac{4^2}{3^5} + \dots \right) = 2\sqrt{3}/5$.

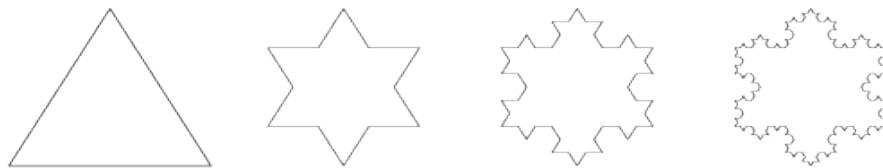


Figure 4.2 Koch's snowflakes

Since the length of each side is increasing by $4/3$ that means we get four components ($X=4$) and the scaling factor is $A=3$, which results¹²⁵ in $d = \frac{\log 4}{\log 3} = 1.26$. Objects with fractional dimensions were first named as fractals by Mandelbrot^{126,127,128}. Mandelbrot introduced the concept of a fractional dimension that increased the complexity of the process which

produced the image. Such complexity, he argued, is due to endless repetition or self-similarity¹²⁷. Subsequently, the term 'fractals' was assigned to objects, including images that are produced by endless self-similarity. When the surface or the image has a rough surface resulting in rich texture, the FD is higher too.

With fractals one can measure natural shapes and make calculations that can be applied to any form such as a waveform or an image. We can get microscopic information out of medical images using fractal dimensions, without having a detailed human visual representation. Fractal dimensions have proven to be helpful in order to extract useful information from medical images^{129,130,131,132}.

Adding a third dimension to a 2D image by elevating the surface based on pixel intensity, one can analyse a rugged surface that is well described by Mandelbrot's fractal dimension of natural images. Fractional Brownian motion (fBm) model has been often use to generate a fractal description of the intensive variations. In this section properties of fractional Brownian motion and how they lead to computation of the dimension are described. Much of the information provided below is given in greater detail by Mandelbrot¹²⁷.

Consider fBm as a Gaussian process, $B^H = \{B_t^H, t \geq 0\}$ that is self-similar and has stationary increments based on Hurst index, $H \in (0,1)$; with mean zero and covariance function given by:

$$\mathbb{E}(B_t^H B_s^H) = R_H(t, s) = \frac{1}{2}(S^{2H} + t^{2H} - |t - s|^{2H}).$$

Self-similarity is described by the same probability distribution of any constant $\alpha > 0$ in $\{\alpha^{-H}B_{at}^H, t \geq 0\}$ and $\{B_t^H, t \geq 0\}$. The covariance function with the increment of the process between $[s, t]$ has normal distribution with zero mean and variance

$$\mathbb{E}((B_t^H - B_s^H)^2) = |t - s|^{2H}.$$

So stationary increments for any $k \geq 1, k \in \mathbb{N}$ is given by¹²⁷:

$$\mathbb{E}((B_t^H - B_s^H)^{2k}) = \frac{(2k)!}{k!2^k} |t - s|^{2Hk}.$$

The fractal dimension, scaling, power spectrum, area and intensity differences are closely related.

When an object can at least be captured in n dimensions, where $n \in \mathbb{N}$, $N(\varepsilon)$ is the number of n -dimensional spheres that capture the object with diameter of ε , one would have a Hausdorff dimension given by D ; if $N(\varepsilon) = \left(\frac{1}{\varepsilon}\right)^D, \varepsilon \rightarrow 0$. If D is fractional, then it is a fractal dimension.

A normalized Brownian feature vector was used for classification, demonstrating intensity differences at different scales and to detect edges, images were transformed by calculating fractal dimension^{127,133}.

Although the fractional dimension of two images could be the same but obviously their textures could be different. Lacunarity of the FD, calculates the amount of space fractals fill. Inhomogeneous images and coarse fractals have higher lacunarity while dense fractals have a lower one.

Among many fractal dimension methods, segmented based fractal texture analysis (SFTA), box counting and semi-variance FD features are often used in the literature along with

texture quantification for higher accuracy results¹³⁴. The section below demonstrates these methods in detail on several DLD patterns and the classification results are discussed. The combination of these fractal features and texture features presented in chapter 3 are demonstrated in detail to show classification accuracy enhancement.

A. Segmentation-based Fractal Texture Analysis

In this section, feature extraction based on segmentation and fractal texture analysis is demonstrated¹³⁴. First one computes a set of thresholds from Otsu's algorithm which take a thresholding range into account as demonstrated in figure below. Otsu's algorithm chooses the threshold to minimize the intraclass variance of the thresholded pixels¹³⁴.

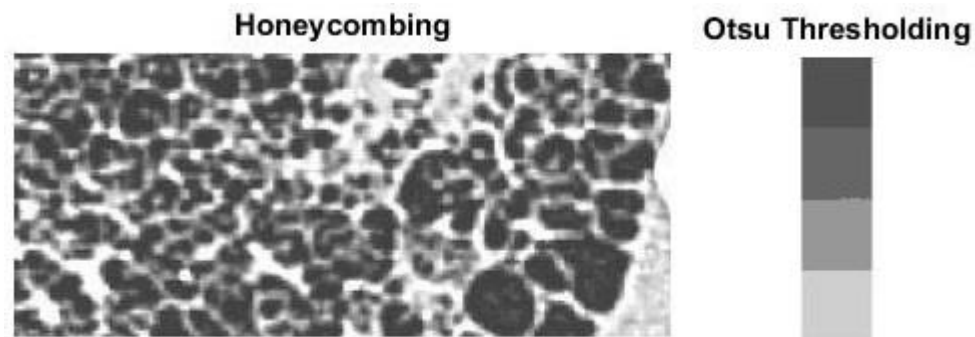


Figure 4.3 A ROI identified with honey combing and Otsu's thresholding ranges

Then we decompose the image into a set of binary images by choosing a pair of thresholds and incorporate 2-threshold segmentation

$$I_{bin}(x, y) = \begin{cases} 1 & \text{if } \text{Min}\{\text{Threshold}\} < I(x, y) < \text{Max}\{\text{Threshold}\} \\ 0 & \text{otherwise} \end{cases}$$

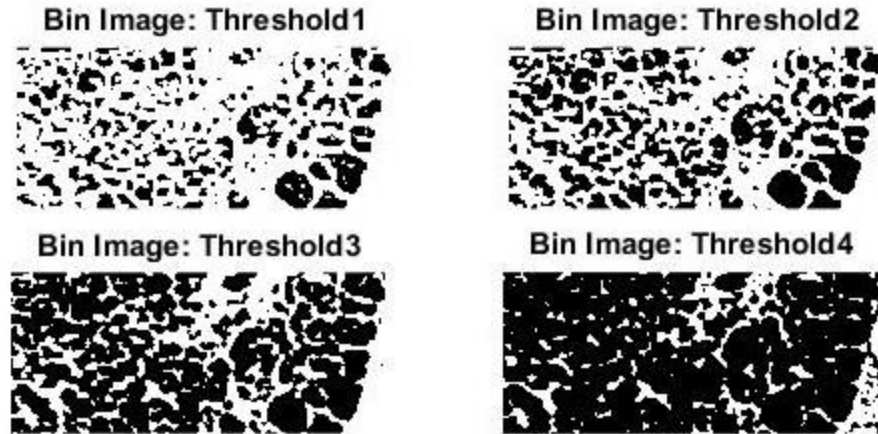


Figure 4.4 Image binarization based on Otsu's thresholds

The number of these binary images would be twice the maximum gray level value of the image. Based on the binary images, a feature vector of image size, mean GLV and fractal dimension is computed.

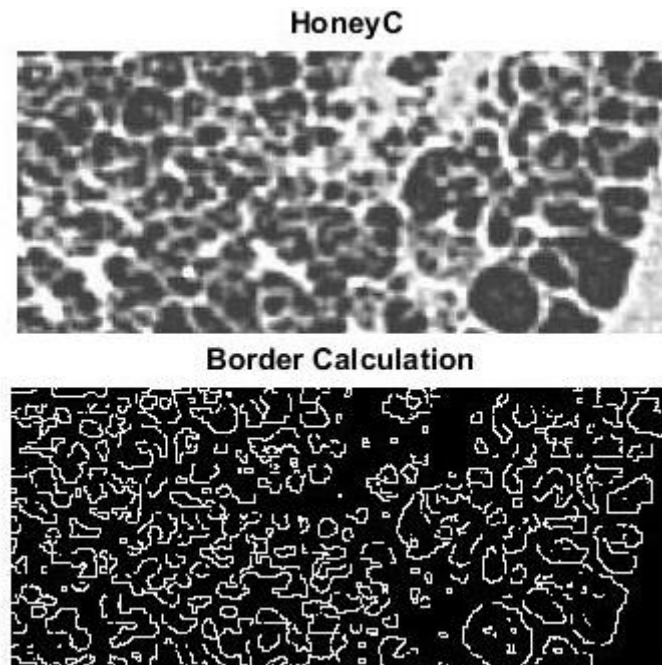


Figure 4.5 Segmented borders are used for FD calculation based on box counting

The fractal dimension for region boundaries is calculated as

$$\Delta(x, y) = \begin{cases} 1 & \text{if } \exists(x', y') \in N_8[(x, y)]: I_b(x', y') = 0 \text{ and } I_b(x, y) = 0 \\ 0 & \text{otherwise} \end{cases}$$

Where N_8 is the set of neighbouring pixels in vertical, horizontal and diagonal directions of pixel (x, y) . $\Delta(x, y)$ will be 1, if the pixel in corresponding binary image is 1 and has at least one neighbour with value 0. FD is calculated based on box counting technique with border length of one pixel.

B. Box Counting Algorithm

The box counting algorithm, often known as brute force method is useful in analyzing FD of natural shapes where repetitive pattern is not clearly seen. It has a good analytical record for calculating fractal dimension when the resolution is low, by capturing the object in squares^{129,130,132}.

To calculate FD of an image, one sets up grids of two different sizes and the comparison of the different number of boxes containing each grid would result in dimension assessment.

$$FD_{bc} = \frac{\log(\text{Number of boxes where pixels of the pattern is present inside them})}{\log\left(\frac{1}{\text{Number of boxes contained within the gride}}\right)}$$

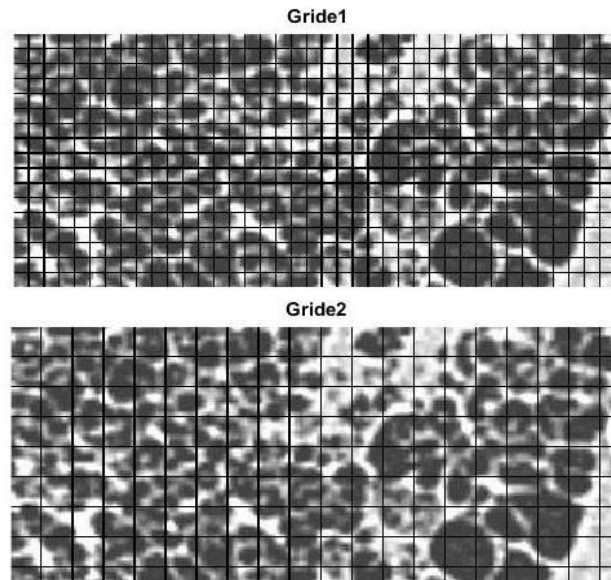


Figure 4.6 Dividing the number of contained Grids results in FD

Grid size is 1000 multiplied by, the size of ROI in the vertical and horizontal directions.

The smaller the boxes, the shape associated with the pattern is better detected.

C. Fractal Dimension Semi Variance Feature extraction Technique

Fractal dimensions can be a directionality descriptor when it is assessed in both vertical and horizontal directions with semi variance method. A semi variance algorithm is incorporated in horizontal and vertical directions to define the summation of pixel values in a specific displacement in each direction. The fractal dimension is evaluated as linear slope of the plots of the \log of semi variance as a function of displacement.

$$f_x = \log\left(\frac{1}{2n(h)}\right) \sum_{i=1}^{n(h)} (p(x_i + h) - p(x_i))^2$$

Where $n(h)$ is the number of paired data at distance h which are 5 pixels in our case; $p(x_i + h) - p(x_i)$ is pixel value displacement.

Figure 4.7 demonstrate FD semi variance feature values in horizontal and vertical directions for two sets of honey combing, consolidation, emphysema and GGO for comparison. The range for these values are very close to each other, therefore when these features are used alone, classification accuracy would be very low. However, it will be shown at the end of this chapter that the combination of these features with texture quantification will demonstrate an increase in classification accuracy.

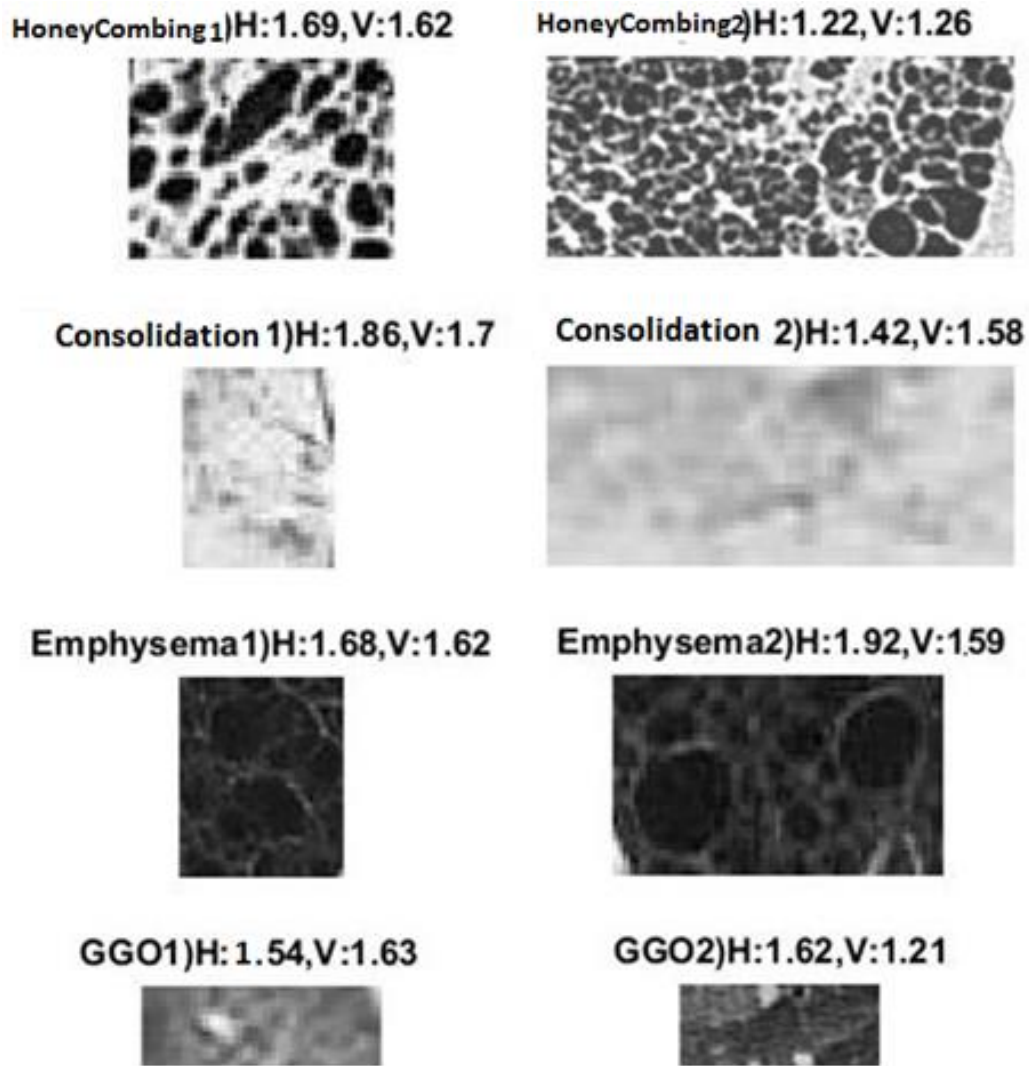


Figure 4.7 Horizontal (H:) and vertical (V:) FDSV results on two pairs of honeycombing, consolidation, emphysema and GGO

III. Accuracy of Classification of CT Image of The Lung Based on Fractal Features

Fractal dimension plays a noticeable role in lung quantification and classification. Since fractal parameters are obtained from a computation which is vastly different from that of statistics of the region of interest and are independent set of features. Theoretically, fractals are calculated for a pattern that has unlimited number of repetitions. But in medical images, such is not the case since every measure from pixel count to gray level values are finite, including the repeated structure within the image. However, these features are helpful in increasing classification accuracy when the number of classes grow, as documented below. From tables 4.1 to 4.5, one can find out the effectiveness of these features when comparing a diffuse lung disease pattern with a healthy lung and also when we compare them with a bigger number of classes.

The number of patients, ROI, diseases and ANN setup are the same, as in Chapter 3. The feature vector size of fractal dimension analysis is 29; box counting produces 3 features, SFTA (segmented based fractal texture analysis) generates 24 features and FD Semi-variance results in 2 features.

Tables 4.1 to 4.5 demonstrate classification accuracy based on the features derived from fractal methods described in this chapter and the validation is based on leave-one-out method. The results are compared with the combination of texture features at the end of this chapter.

Abnormality							
GGO	12.7%	21%	28%	32%		43.2%	
Consolidation				32%			45.4%
Scar			34%	31%		42.5%	
Cyst				31%			47.7%
Emphysema				31%			
Reticulation		24%	37%	46%	36%	52.9%	
HoneyCombing				47%			51.3%
Fibrosis			47%		51.6%		
Nodularity			35%			48.2%	
Tree in bud			35%		47.1%		

Table 4.1 ANN average classification accuracy based on SFTA feature analysis

Abnormality							
GGO	11.25%	20.1%	27%	30.6%		41%	
Consolidation				30.6%			44.1%
Scar			32%	29%		41.5%	
Cyst				29%			46.6%
Emphysema				29%			
Reticulation		23.8%	35.6%	45%	35%	50.7%	
HoneyCombing				46%			51.3%
Fibrosis			46%		50.5%		
Nodularity			34.7%			48.9%	
Tree in bud			34.7%		47.4%		

Table 4.2 ANN average classification accuracy based on box counting feature analysis

Abnormality						
GGO	10.3%	19%	27%	30%		42.9%
Consolidation				30%		
Scar			31.5%	28%		40.5%
Cyst		28%		46.6%		
Emphysema		28%			46.9%	
Reticulation		21%	34%	45%		34%

HoneyCombing					45.5%		50.9%
Fibrosis							50.7%
Nodularity			34%				47.1%
Tree in bud							46%

Table 4.3 ANN classification accuracy based on FD semi-variance analysis

Abnormality									
GGO	19.7%	31%	39%	51%			58%		
Consolidation								57%	
Scar								51%	
Cyst				51%	39%			58%	
Emphysema								57%	
Reticulation		33%		40%	48%	39%		59%	
HoneyCombing							45%		51%
Fibrosis									52%
Nodularity					52%				59%
Tree in bud									56%

Table 4.4 ANN classification accuracy based on all Fractal Dimension features in the present chapter

Fractal features are not good descriptors in medical image quantification of the lung parenchyma. However a combination of these features provides better classification from 2-11 classes. The highest classification accuracy when all fractal features were combined is 19.7 for eleven classes (table 4.4). These results can be used in conjunction with other features, as seen below.

Although fractal dimensions are not sufficiently descriptive and cannot be used as stand-alone features for classification of DLD patterns, the next section will present results of combining fractal features with texture features, on the classification accuracy.

IV. Classification Accuracies of The Combination of Texture and Fractal Features

Table 4.5 demonstrates classification accuracy of all DLD patterns based on the combination of texture features described in chapter 3 with fractal dimension feature demonstrated in this chapter. Comparing the results with table 3.15 and figure 3.25 one can conclude that adding fractal dimension features slightly increases classification accuracy of irregular radiological patterns of the lung, especially when the number of classes increases.

Abnormality						
GGO	62.5%	77.8%	91%	93.9%		99.2%
Consolidation						99.4%
Scar						97.8%
Cyst	74.3%		94.4%	91%		98.3%
Emphysema						99%
Reticulation				95.5%	83.9%	99.9%
HoneyCombing				91.7%		99.9%
Fibrosis						99.9%
Nodularity						96.3%
Tree in bud						97%

Table 4.5 ANN classification accuracy based on all FD and all texture features

Although there is a slight accuracy increase in training the ANN, by combining fractal features with texture methods, but this higher accuracy is of interest, especially because the increase in accuracy is consistent with higher number of classes, except when considers 11 classes.

V. Results

Classification results are provided in figure 4.8 based on the combination of features in this chapter and all the features in chapter 4, on different number of classes. Since learning accuracy has increased based on this merge, classification performance has also taken advantage of it. Features generated by fractal analysis alone, are not sufficient to classify ROIs from various diseases of the lung. It can be observed that the classification accuracy is less than 60% even with two classes. A combination of features from fractal and statistical texture analysis increases the accuracy.

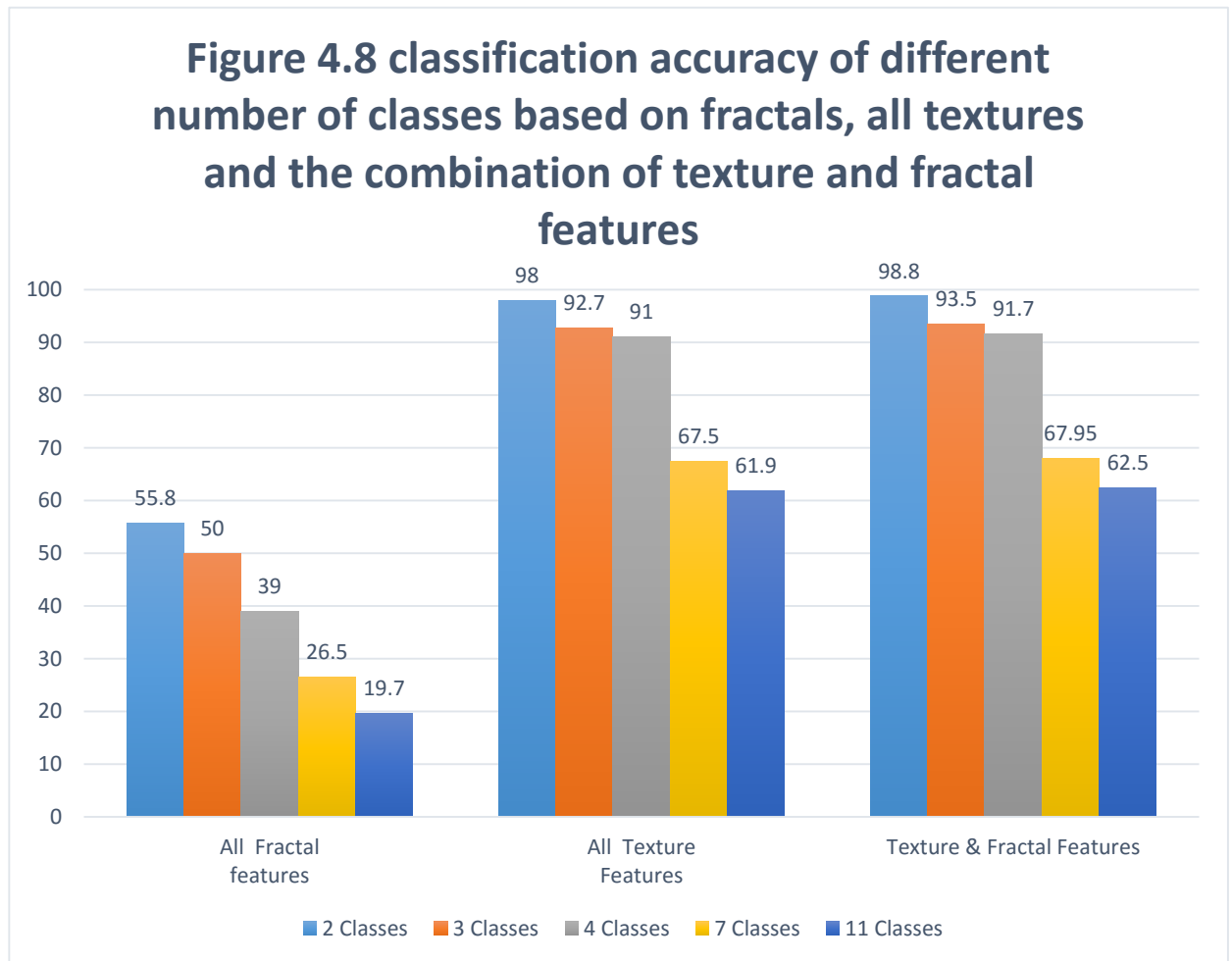


Figure 4.8 shows classification accuracy drops when the number of classes increases for any combination of methods. According to this bar graph, less than a percent of accuracy was added to the classification performance when fractal features were included in the quantification. Although such increase in classification accuracy is negligible when classification is measured for two or three classes, may be useful in the presence of images from 11 classes and when a larger database of patients is available.

Although FD provides scaled features, it is naturally a shape detector underneath, as per its theoretical basis. Fractal analysis is not merely a dimension finding exercise. It has the capability of narrowing down the basic structure of the whole picture. For instance, when analysing a mountain with fractal methods, one can see the basic shape is similar to a triangle, because if one populates the objects with triangles of different sizes and angles one arrives at a mountain shaped figure. If one takes the same behaviour on honey combing patterns for instance, by segmentation-based fractal analysis using box counting method, one can see that all gray level pixels fade away and only the boundaries remain. When a grid is applied to the ROI, each square containing a part of that pathological pattern would be counted toward box counting analysis. Therefore, boxes that remain for counting, have the same formation as the disease pattern. Such characteristics do not look descriptive when examined alone, but becomes meaningful when other statistical measures are added for training an ANN. It is postulated that such quantification is consistent with image structure, resulting in better classification accuracy in the presence of increasing number of classes.

One can therefore conclude that, classification of CT images is not feasible using only fractal analysis, but when combined with texture features, they may help identify irregular patterns of DLD with high accuracy.

VI. Chapter Summary

In this chapter, algorithms for segmentation based fractal analysis, box counting and FD semi variance method were analysed. These methods were applied to DLD images and classification results were analyzed.

Training and classification accuracy based on features derived from FD analysis demonstrated poor results. However, combining them with previously described texture features slightly increases classification accuracy from 98% to 98.8% when classifying 2 classes. The classification accuracy slightly but consistently increased for increasing number of classes when features derived from FD analysis were combined with Haralick based texture features.

CHAPTER 5

SCALE INVARIANT FEATURE TRANSFORM FOR CLASSIFICATION OF CT IMAGES OF THE LUNG

I. Introduction.....	118
II. SIFT Methodology and Algorithm description.....	118
A. Edge and Corner versus SIFT Interest Point.....	120
B. SIFT Transformation Using Gaussian Filter.....	123
C. Edge Detection Based on Scale-Space.....	125
1. Detecting Interest Points Using Zero Crossing Method.....	126
2. Identifying Interesting Points Using Interval tree.....	129
D. Potential key-Point Identification Using Laplacian of Gaussian or Difference of Gaussian.....	130
E. Eliminating Outliers Using Taylor Series and Hessian Matrix.....	135
F. Evaluation of Key-Point Orientation and Descriptor Vector.....	137
III. Processing of Labelled CT Image Data and Training of the ANN Algorithm.....	139
IV. Results of Classification of CT images of the lung Based on SIFT Features.....	140
VI. Accuracy of Classification Based on A Combination of SIFT and Texture and Fractal Features.....	143
VII. Results.....	144
VIII. Chapter Summary.....	146

I. Introduction

An important phase of medical image processing is to characterize the image with well-defined features. In the previous chapters of the thesis, various feature selection and classification methodologies were discussed, based on well descriptive texture statistics and fractal analysis methods. To be able to identify objects in real world applications, one naturally looks for features that are not blocked by the surrounding objects. Not only do selected features have to detect unique objects, they preferably have to be invariant to illumination and 3D projective transformations. While several thousands of features can be extracted from an image, the computational overhead is prohibitive, especially if such features do not have distinctive characteristics and do not contribute to the classification task in a meaningful way.

This chapter introduces a unique approach toward extracting features with characteristics different in nature from texture and fractal quantification of lung images; this novel technique is called scale invariant feature transform (SIFT), which is gaining acceptance as a method of feature selection in medical imaging. In the following sections, the specific application of SIFT to CT image of the lung containing DLD patterns for classification problem is presented.

II. SIFT Methodology and Algorithm description

The scale invariant feature transform, called SIFT in short, was developed by Dr. David Lowe^{62,135}. SIFT is a feature selection method that can find interesting points regardless of different depth or scale. Since the depth of penetration and resolution varies between different optical and/or imaging techniques, SIFT is useful for comparing different images

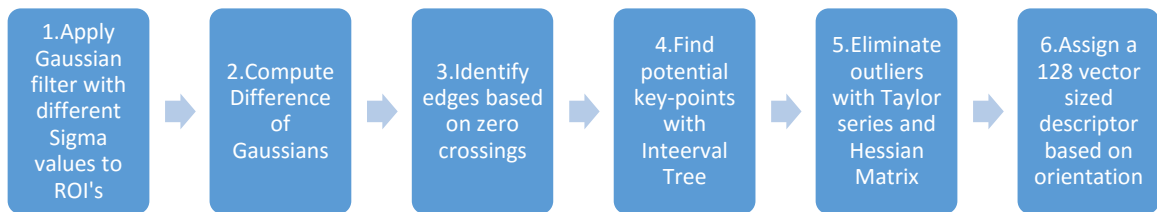
created by different sources of images. SIFT is also rotation invariant. The SIFT method is affine to rotation, 3D viewpoint and it is not sensitive to noise or illumination¹³⁵. SIFT is very often used for facial recognition and for identifying objects in different representations of a scene (rotated, with noise, different depth and so on)^{136,137,138,139,140}. Furthermore, SIFT is a local feature extraction technique implying that one analyzes pixels that are close to each other. It is also relevant to mention that with SIFT one does not make a judgment based on global features such as a histogram, which incorporates information from all pixels within the image. SIFT generates a large number of interesting points and descriptors which enables one to detect objects better. SIFT preserves points, straight lines and planes since it involves Gaussian operation which is known to preserve transformations, often termed as an affine transform.

In brief, SIFT operations involve following steps¹³⁵:

1. Scale space peak selection: potential features are detected
2. Localizing Key-points: identify Key-point locations, having excluded least descriptive points
3. Assign orientation to each Key-points
4. Key-point descriptor: Generate a high dimensional vector describing Key-points

The SIFT takes advantage of Gaussian transformation to mask a ROI, based on several scales (sigma values) on different octaves (image size). Laplacian of Gaussian (LoG) or Difference of Gaussian (DoG) is then computed. Based on the zero crossing technique, edges are identified. Using an interval tree, stable edges are picked as interesting points. Each interesting point is compared with its neighbours, within its scale and the higher and

the lower scale. If the interesting point is an extrema, compared to its neighbours, then it is chosen as a potential key-point. SIFT does not use edges as key-points, and if the potential key-points are on edges, they will be eliminated using Taylor series and the Hessian matrix. At this point, key-points are identified which are the features of ROI. SIFT's strength is in having a descriptor for each feature, which is assessed using central derivatives, gradient magnitude and directions. The orientation and magnitude are computed for each key-point, and the dominant orientation is chosen. Then an eight bin histogram for each 4x4 region within 16x16 neighbourhood of the key-point is calculated to generate a 128 vector size descriptor or a feature vector. Below diagram demonstrates the steps sequentially.



A. Edge and Corner versus SIFT Interest Point

Harris detector is one of the well known edge detectors in image processing but lacks the specificity of the SIFT, which generates key-points. SIFT generated key-points are based on extrema identified through LoG and scale space, while edge detectors only identify a key-point which has an outstanding gray level difference with its neighbours, for instance in a ROI selected from a CT images of the long.

Because, SIFT key-points are evaluated in a different way compared to edge and corner identification, we first clarify what is meant by edges generated by Harris detector¹⁴¹.

Consider the image shown in Figure 5.1. Suppose, one wants to detect the red corner shown in Figure 5.1 with Harris detector for instance:

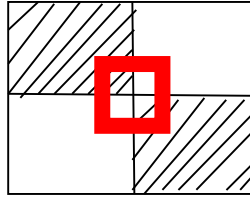


Figure 5.1. Corner and edge detection based on Harris detector

Calculating gradient of this image (directional changes in intensity) over the red window size in horizontal and vertical directions will result in a corner, if both values are large. If one of the horizontal or vertical values is large and the other is small then it is identified as an edge.

$$\sum (g_x)^2, \quad \sum (g_y)^2$$

g Represents the image and the sum is over the red area. But if the horizontal or vertical gradients are not significant, it can be rotated back to a well pronounced image by using Eigen value decomposition

$$H = \begin{bmatrix} \sum g_x^2 & \sum g_x g_y \\ \sum g_x g_y & \sum g_y^2 \end{bmatrix}.$$

This will generate two Eigen values and if both values are large, then a corner is detected and if one of the values is large and the other value is small, then an edge is identified. This method is applied to every pixel in the image and the local maximum of the result is assessed for both Eigen values, which gives us Harris corner/edge detector.

In the above definition, Eigen values are defined as follows: Consider a matrix A which has a dimension $N \times N$. Scalar λ is an Eigen value of A if there is a non-zero vector x such that $Ax = \lambda x$. This vector is called and Eigen vector of A corresponding to λ . If λ is an

Eigen value of A , and x is an Eigen vector belonging to λ , then any non-zero multiplication of x is still an Eigen vector.

Figure 5.2 demonstrates CT image of the chest with honeycombing DLD pattern, where corners are detected with Harris algorithm (and identified by green +).

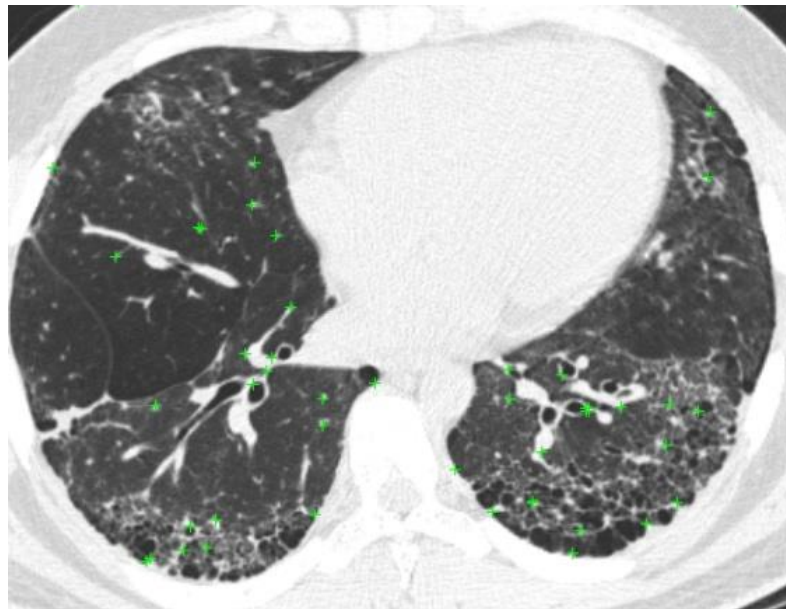


Figure 5.2. Corners detected with Harris algorithm (green +)

There are several other edge and corner detection methods in the literature. It is illustrative to examine some of them. Figure 5.3 represents a sample of edge detection methods applied to a CT image of a lung identified with cystic ROI, using Prewitt¹⁴⁴, Canny¹⁴³ and Zero Crossing edge detection methods. Zero crossing can identify edges on scale space which is why it was chosen for SIFT analysis in this thesis¹³⁵.

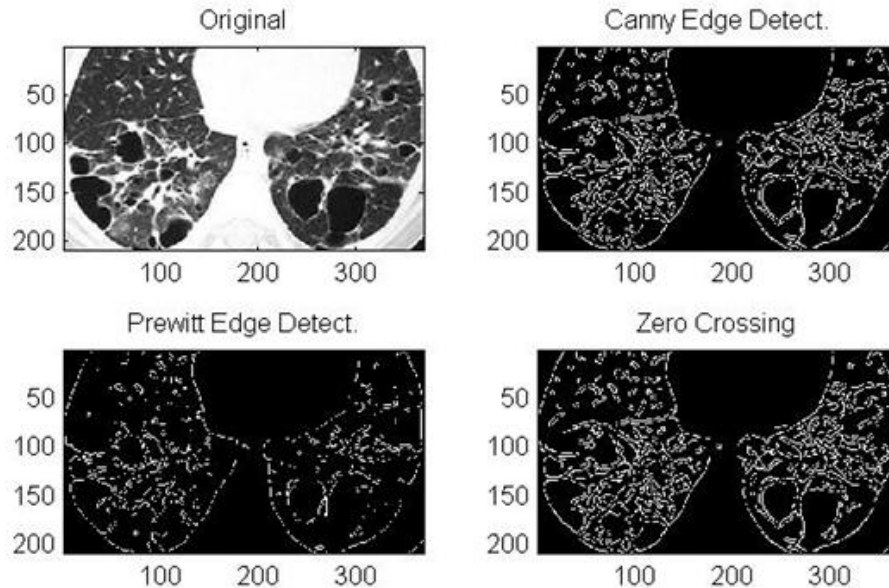


Figure 5.3. Evaluation of edge detection using Canny, Prewitt and zero-crossing algorithms

B. SIFT Transformation Using Gaussian Filter

In this section details of the SIFT algorithm are presented. The computation of SIFT is based on the Gaussian filter which is applied to the ROI. When applying the Gaussian filter, Laplacian and smoothing, the size of sigma (standard deviation), often referred to as the width of the mask is determined by the scale of the image. Identifying a proper sigma value for any analysis is crucial, and there are no specific guidelines in the literature. Therefore, sigma values are often arrived at empirically, depending on the richness of the grey levels present in the image. With scale space a whole spectrum (continuum) of scales are used. Then using zero crossing detector, described earlier, edges are identified.

For an image $f(x, y)$ the Gaussian scale space representation is

$$g(x, y; \sigma) = \frac{1}{2\pi\sigma} e^{-\frac{x^2+y^2}{2\sigma}}$$

When $\sigma = 0$ image representation is $g(x, y; 0)$, the image is unchanged. As the sigma grows the image becomes blurry. Not all low pass filters can generate images that produces images which span different scale space. Therefore the Gaussian filter is used, because it generates images which are consistent with scale space axioms. In other words, when going from fine to finer scale, a completely new structure is not created which is the definition of affine transform, and an important characteristic of SIFT. Figure 5.4 shows an application of Gaussian filter with different sigma values on an image of lung identified with regions containing cysts.

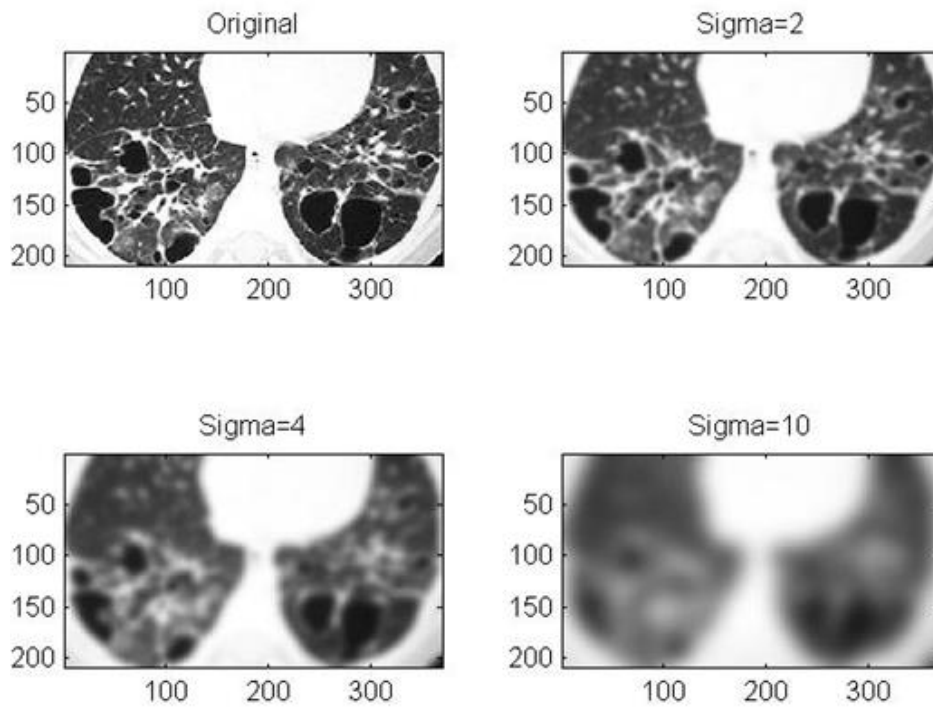


Figure 5.4. A Chest CT image with Gaussian filter applied at different sigma values

Figure 5.5 shows the effect of different filters on a CT image with cystic regions. Laplacian filter can demonstrates the edges better than Gaussian and Laplacian of Gaussian (LoG),

but SIFT method is interested in the analysis of images based on different scales. Later in this chapter it is shown that LoG is the same as difference of Gaussian.

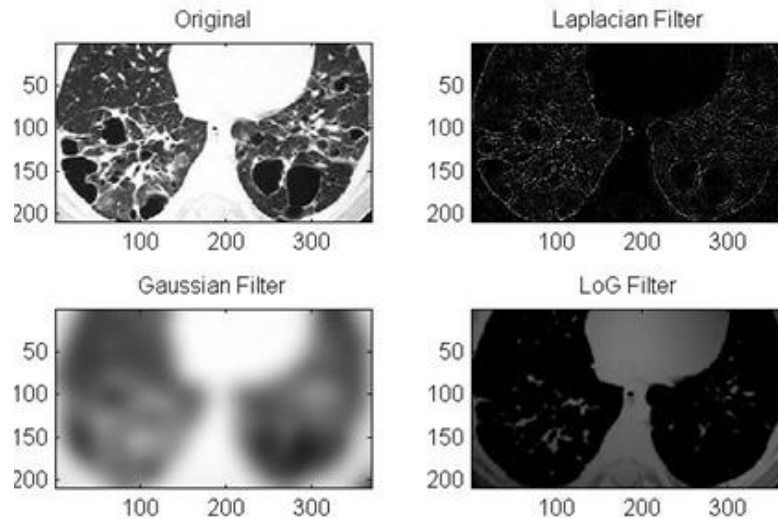


Figure 5.5. Effect of different filters on a CT image of the lung Identified with Cysts

C. Edge Detection Based on Scale-Space

The motivation for scale space is that objects may have different structures at different scales. For instance, lung images can be analysed in scale of centimeters for honeycombing, while nodularity is analysed at finer scales. Often one does not have knowledge of the scale of objects in a ROI. The SIFT provides a very useful capability to study images at different scales, since the scale space is preserved.

Finding edges is a critical technique in image processing of CT images described in this thesis, and is performed using a gradient filter during SIFT analysis. The gradient filters locate pixels with rapid changes of intensities or pixels with discontinuities, which results in edges or boundaries. Laplacian for example, seeks out points in frequency domain where digital signal of the point passes through a pre-set zero value (places where Laplace changes sign from negative to positive for instance) and marks it as a potential candidate for an

edge. Edges are locations in an image around which intensity changes rapidly. When the signal has passes through the zero intensity it is called zero crossing.

1. **Detecting Interest Points Using Zero Crossing Method**

Zero crossing is generated from Laplacian of Gaussian (LoG) filters and is affected by the size of sigma to a large extent. The more an image is smoothed, fewer zero crossings are found¹⁴⁵. Primary objective of the zero crossing detector is to identify edges and eliminate them. Zero crossing can also be found at locations where intensity gradient starts increasing or decreasing, which may not always represent an edge¹³⁵.

While increasing the value of sigma, edges begin to disappear. Figure 5.6 shows CT of a patient image with honeycombing pathology processed with different sigma values to demonstrate how edges fade away while the scale increases. Zero crossing filter demonstrates a smoother image (fewer number of edges) when sigma value is higher. For instance, one can find more zero crossings (edges) with $\sigma = 0.003$ than with $\sigma = 0.005$. At $\sigma = 0$ all zero crossing are detected.

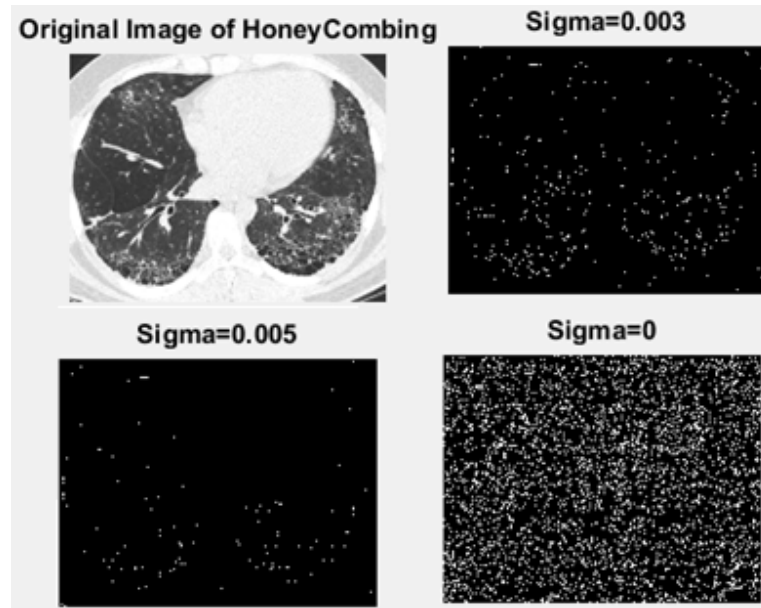


Figure 5.6. Edges tend to fade away while sigma value of the Gaussian filter increases

In order to illustrate zero crossings, its application on a randomly generated 1-D (one dimensional) signal, which is randomly generated, is shown in Figure 5.7. It is sequentially smoothed using a Gaussian function with different sigma values as depicted (on the y-axes on the left side). As one can see, by increasing sigma value, the signal becomes smoother and represents progressively less information. On the right of the figure 5.7, one can see zero crossing at different scales. At lower scales one can observe increasing number of zero crossings. These points represent changes in a 1-D signal and edges in 2-D (two dimensional) images. When the scale increases, zero crossings diminish. There are arches representing zero crossing that are closed in higher scales and open at the bottom. This means, at lower scales there are more edges and as the scale increases, a combination of those edges (arches) will present an edge. When the arch is closed and disappears at higher

scales, that edge cannot be represented at that scale level any more due to smoothing. That is how smoothing using various Gaussian filter with increasing sigma will disregard edges.

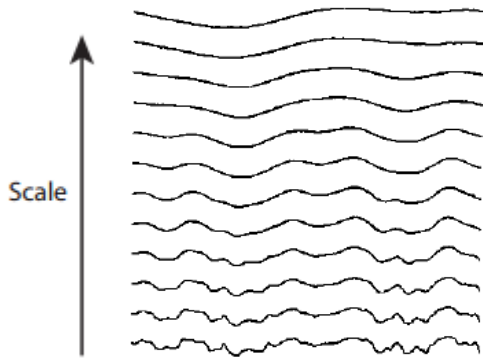


Figure 5.7 (a)

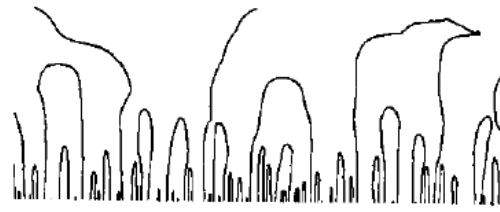


Figure 5.7 (b)

Figure 5.7. (a) Signal representation at different scales (b) Zero-crossings of the same signal¹³⁵

Figure 5.8 shows an original CT image of a patient with emphysema. The threshold is set to 0.15 for zero crossing (a large jump over zero crossing is an edge). Zero-crossing with different standard deviations is demonstrated in figure 5.8.

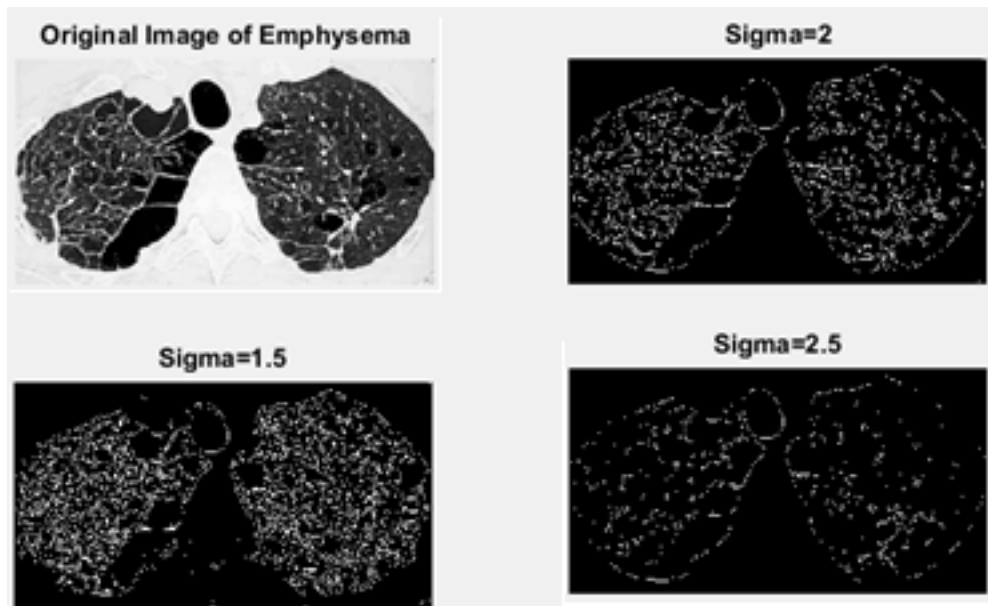


Figure 5.8. Zero crossing representation of an image with different sigma values

2. Identifying Interesting Points Using Interval tree

Zero-crossings are evaluated in scale space at different scales and are prepared for subsequent analysis. To clean up the scale-space resulting from zero-crossings, an interval tree, where interval being considered increases successively, is created. Such a process is shown in the figure 5.9 and 5.10. Each rectangle represents changes (node) in a specific interval.

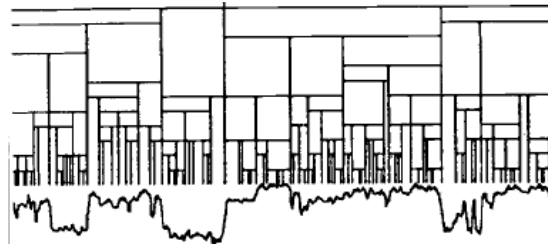


Figure 5.9. Rectangular representation of scale-space¹³⁵

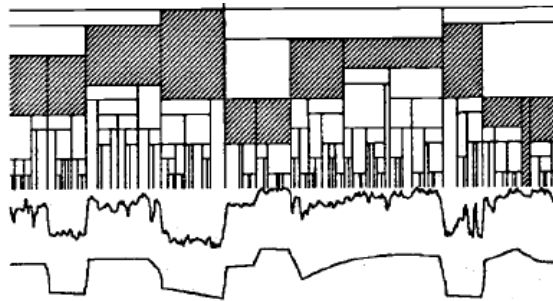


Figure 5.10. The shaded rectangles represent the smoothed signal¹³⁵

Figures 5.9 and 5.10 show, while going from top to lower down in these images, each parent node is divided to child nodes. Stability of a node is based on scale range over which the node is alive in that interval. To end up with a stable result or well smoothed signal, nodes which are less stable than those of their parents are removed.

The process of choosing stable edges in a 1-D signal explained above, can be extended to 2-D images and serves as the basis for SIFT detector is local maxima in scale space of LoG.

D. Potential key-Point Identification Using Laplacian of Gaussian or Difference of Gaussian

To decide if a point on an image is an interesting point, zero-crossing and interval tree were used so far based on a Gaussian filter applied to an image with different sigma values. To generate these blurred images, Lowe used three sigma values per octave, because based on his analysis, that number of scales would give the highest repeatability characteristic¹³⁵. Meaning that, if a point of interest is found in an image within any scale of Gaussian filter, it can also be found in other scales and octaves as well. Based on his analysis, more scales would not contribute to this characteristic.

The initial sigma value is 1.6, based on Lowe's stability assessment and it will be multiplied by $\sqrt{2}$ for the next scale. These values were based on the experience of analyzing a variety of images and for covering as much scale as possible, by Lowe¹³⁵.

Each octave is a different size of the image. So, the first octave has the original ROI size, and the second octave one is half the size in x and y directions. So the first image in second octave will be twice as blurred, compared with the same sigma value applied to the first image in the first octave. When the Gaussian transformation of these images were evaluated, LoG is assessed to localize potential key-points. LoG is the same as DoG which will be demonstrated later in this section. Figure 5.11 represents Gaussian scale space in different octaves and also demonstrates a visual assessment of difference of Gaussian of images at different scales.

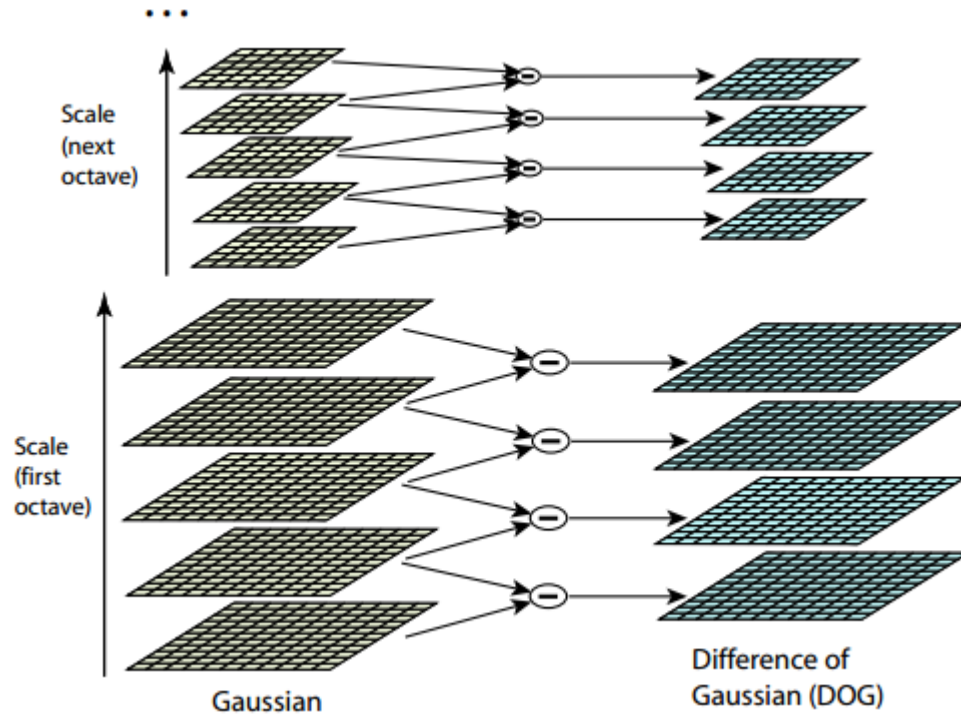


Figure 5.11. Scale space representation of Gaussian filter on different octaves and DoG¹³⁵

To assess interesting points generated from zero-crossing, a neighboring region of 3x3 pixels surrounding that point of interest in the LoG representation of the image will be compared to the same region with a higher scale and a lower scale. So there will be 27 points and the center point is the one, about which a decision will be made. If the point of interest is an extrema (minima or maxima) of all 26 points, then that is a potential SIFT Key-point¹³⁵. Figure 5.12 is a representation of extrema assessment among 26 neighbours.

The function for Laplacian of Gaussian is

$$LoG(x, y) = -\frac{1}{\pi\sigma^4} \left[1 - \frac{x^2 + y^2}{2\sigma^2} \right] e^{-\frac{x^2 + y^2}{2\sigma^2}}$$

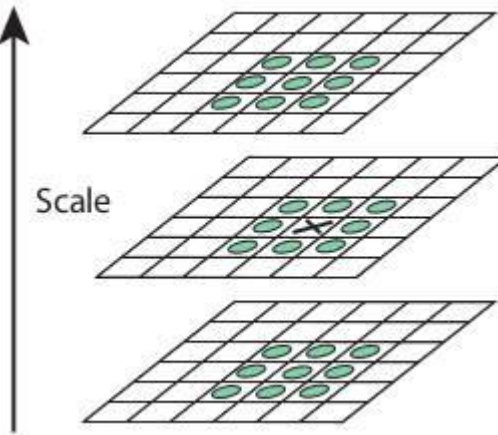


Figure 5.12. Finding potential Key-point on the basis of lower and upper scale comparison¹³⁵

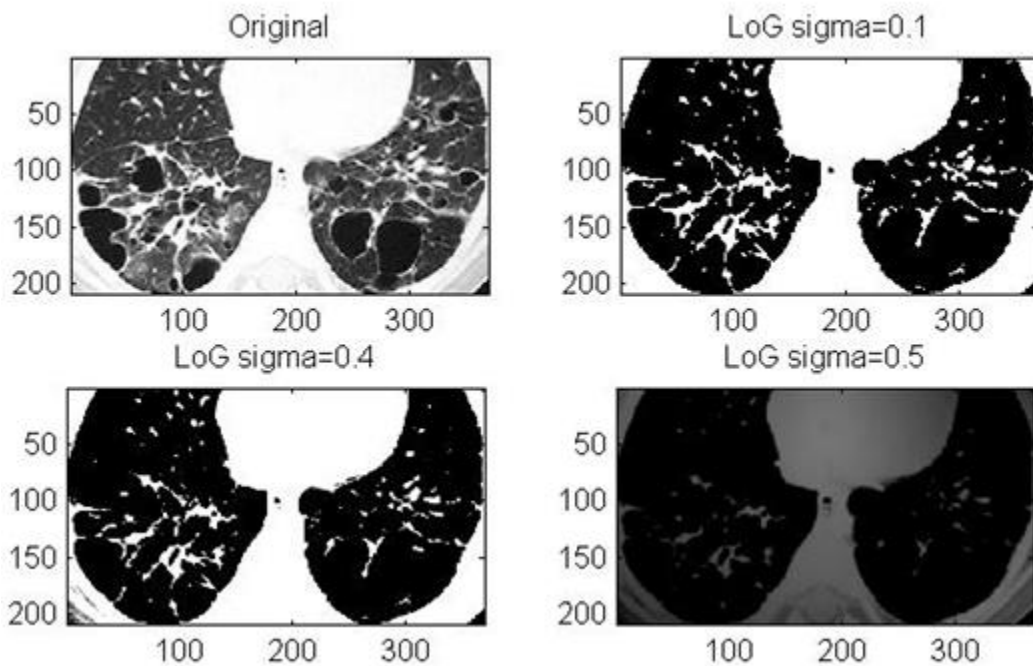


Figure 5.13. LoG of the same image at different scales shows how an image gets blurred by preserving the sub-structure

An efficient way of comparing these images at different scales is to find the difference of Gaussian of an image at two different scales, which is the approximation of LoG¹³⁵. Differences at every scale are calculated and as the scale goes higher, the image gets more blurred. This approximation is based on the heat transfer^{135,142} equation where derivative

of Gaussian with respect to sigma is equal to Laplacian of Gaussian (with respect to x and y) multiplied by sigma

$$\frac{\partial G}{\partial \sigma} = \sigma \Delta^2 G.$$

From this equation it can be shown that LoG is an approximation of difference of Gaussians. The heat equation can show the difference of Gaussian with respect to three variables x, y and σ

$$\sigma \Delta^2 G = \frac{\partial G}{\partial \sigma} = \frac{G(x, y, k\sigma) - G(x, y, \sigma)}{k\sigma - \sigma}$$

$$G(x, y, k\sigma) - G(x, y, \sigma) \approx (k-1) \sigma^2 \Delta^2 G$$

So, difference of Gaussian with different sigma is an approximation of LoG.

Figure 5.14 is a representation of an image with a Gaussian filtered image with two different sigma values and the difference is shown. The sigma value of the original image is Zero.

After applying different scales to the image ($k\sigma, k^2\sigma, k^3\sigma, \dots$) the image is sub-sampled by taking every other row and column (one fourth of the original resolution). And then different scales for generating LoG ($k^2\sigma, k^3\sigma, \dots$) is applied. The impact of filtering with $k^2\sigma$ at the next octave will be twice as much, since the resolution is lower¹³⁵.

So far, SIFT potential key-points are found based on the extrema found in DoG of scale space, but the outliers should be eliminated so that there are only well-defined key-points, a step discussed in the next section.

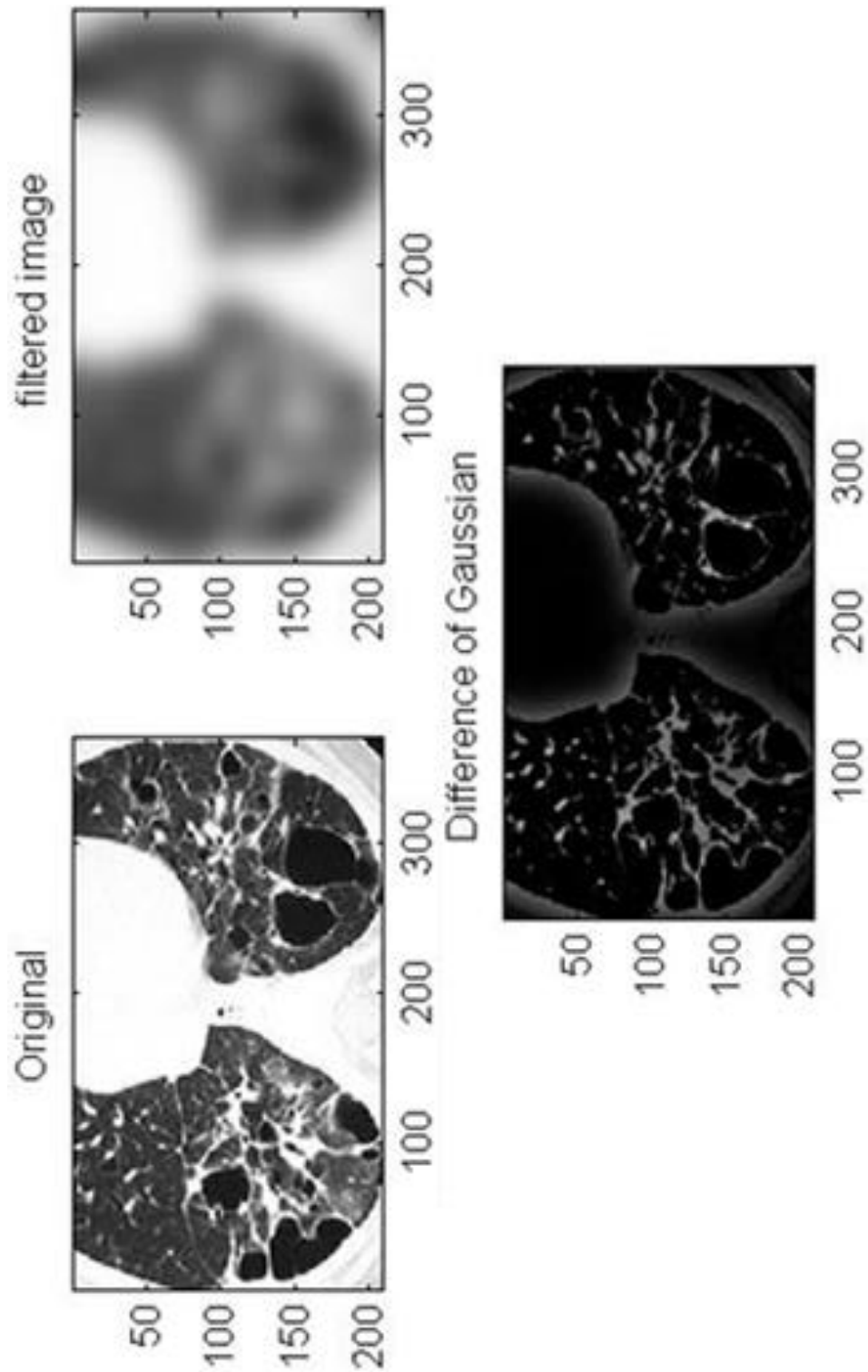


Figure 5.14. Top left corner: represents original image with sigma=0; Top right corner: represents Gaussian of the original image with sigma 10; The last image: represents the LoG or DoG

E. Eliminating Outliers Using Taylor Series and Hessian Matrix

At this point one can, localize best points by location and scale (x, y and σ). Due to low contrast or because candidates are along edges, Taylor series is used to eliminate those points¹³⁵. In general, Taylor series of a function, $f(x)$, is expressed as:

$$f(x) = \sum_{n=0}^{\infty} f^{(n)}(a) \left(\frac{(x-a)^n}{n!} \right).$$

In this equation the same function is applied to $D(X)$

$$D(X) = D + \frac{\partial D^T}{\partial X} + \frac{1}{2} X^T \frac{\partial^2 D}{\partial X^2}.$$

Approximation of a function is assessed with Taylor series and therefore, noise can be eliminated and outliers will be avoided (key-points are identified from potential candidates).

In this equation, if D is a function of three variables $X = (x, y, \sigma)^T$, the approximation (extrema) of Taylor series for this scale space is found at

$$\hat{X} = - \frac{\partial^2 D^{-1} \partial D}{\partial X^2}.$$

If X is the extrema and the value is above the threshold of 0.03, the point will be kept, otherwise removed.

Another step towards outlier rejection is to remove interesting points on edges¹³⁵, because they are not considered sufficiently interesting Key-points for the SIF based analysis. To perform such an operation, DoG is assumed to be a surface and principal curvature (PC) is computed. PC will be very low along the edge and very high across it. Then a Hessian matrix is computed over D which is based on its second derivative over x, y and xy

$$H = \begin{bmatrix} D_{xx} & D_{xy} \\ D_{xy} & D_{yy} \end{bmatrix}.$$

To remove these outliers the trace and determinant of this matrix is calculated:

$$Tr(H) = D_{xx} + D_{yy} = \lambda_1 + \lambda_2$$

$$Det(H) = D_{xx}D_{yy} - (D_{xy})^2 = \lambda_1\lambda_2$$

where λ is an Eigen value and therefore, the sum of Eigen values are equal to the trace and their product is equal to the determinant of this matrix. The ratio of this result is evaluated.

$$\frac{Tr(H)^2}{Det(H)} = \frac{(r+1)^2}{r} \quad \text{where, } r = \frac{\lambda_1}{\lambda_2}$$

If r which is the ratio of two Eigen values is greater than 10 then, those points will be removed.

In figure 5.15, you can see a CT image of lung identified with honeycombing. On the left of figure 5.15 below, one can find all the potential key-points with local maxima, and on the right of figure 5.15 one can find the final set of key-points, having edges and outliers eliminated.

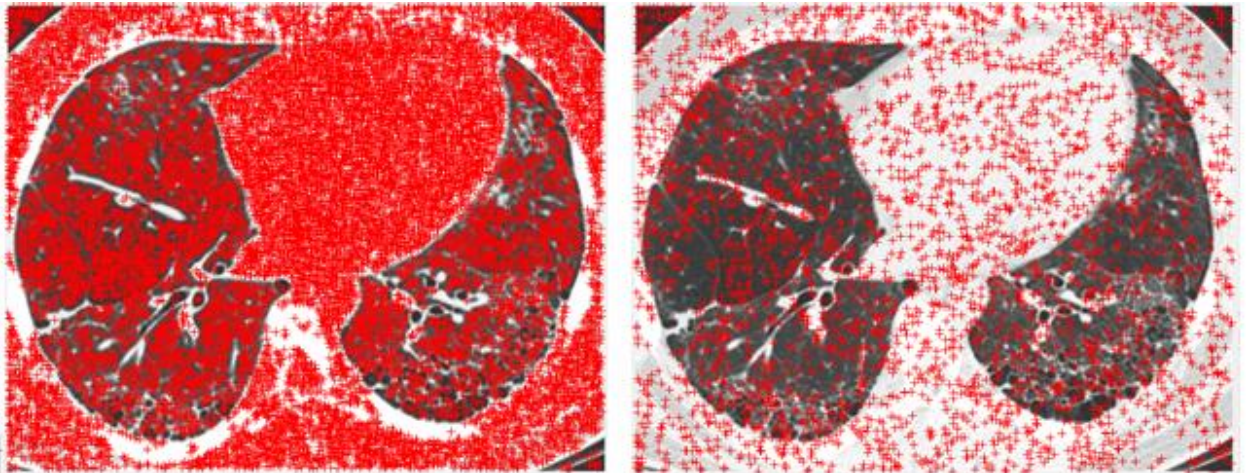


Figure 5.15. Potential key points based on local maxima (left) and Key-points (right) with red +

F. Evaluation of Key-Point Orientation and Descriptor Vector

At this point, finding the orientation of key points is of interest, which allows rotation invariance characteristic, because all orientations can be rotated around a dominating orientation and get aligned with it. For this purpose, central derivatives, gradient magnitude and direction L (smoothed image) are calculated¹³⁵, which is the smoothed image at location y . The magnitude is calculate based on the squared summation of x and y derivatives.

$$m(x, y) = \sqrt{\left((L(x+1, y) - L(x-1, y))^2 + (L(x, y+1) - L(x, y-1))^2 \right)}$$

And the direction is based on the tangent of x and y derivatives.

$$\theta(x, y) = \tan^{-1} \left(\frac{L(x, y+1) - L(x, y-1)}{L(x+1, y) - L(x-1, y)} \right).$$

Then a weighted direction histogram in a 16x16 neighborhood of a key-point is created. In a histogram which is usually shown in terms of a bar graph, the data goes on x axes and the frequency or the number of repetition of them goes along the y axes. This histogram has 8 bins. The weights are based on the gradient magnitude in every 4x4 region of the 16x16 neighbourhood; the larger the magnitude of a particular bin the more it affects the direction¹³⁵. Consider Figure 5.16 which shows direction of a 4X4 region. The composite direction is shown in Figure 5.17

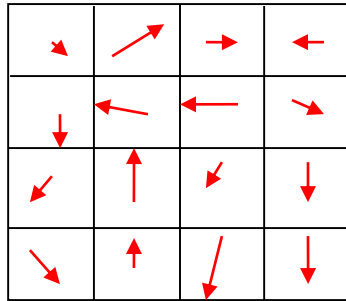


Figure 5.16. Weighted direction histogram in a Key-point neighborhood

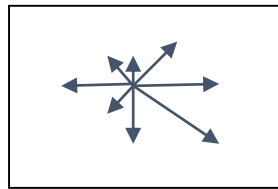


Figure 5.17. Weighted direction histogram in a Key-point neighborhood

If there are multiple directions, the highest peak and any other peak which is 80% of the peak is taken into consideration. Usually there is only one peak to choose in a weighted direction histogram.

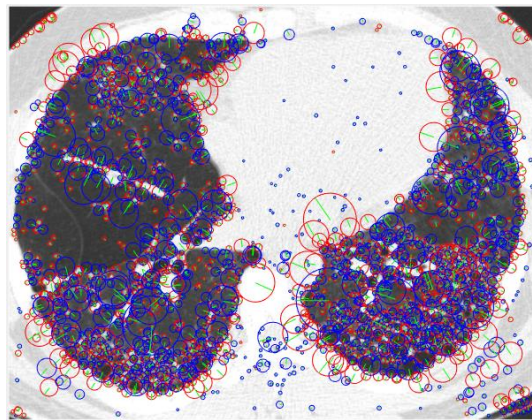


Figure 5.18. Maxima (red) & minima (blue) interesting Key-points and their direction (green)

At this stage, interesting points (blue and red circles) are extracted and SIFT based descriptors are going to be assessed for each interesting point. The weighted direction is

demonstrated by the size of the circles and the green arrow, in figure 5.18. Since the intensity value is sensitive to illumination and noise, gradient orientations were used as descriptors. Because gradient orientations analyze changes, they will not vary a lot and are more stable, comparing to absolute intensity values.

To extract descriptors, a 16x16 neighborhood is assessed (weighted direction histogram) which creates 16 histograms (4x4 regions in the neighbourhood). Since each histogram has 8 bins (eight directions) and there are 16 of them, 128 features are created, which together are called SIFT descriptors. Assigning these values to a vector and normalizing them, a feature vector is created for each ROI.

III. Processing of Labelled CT Image Data and Training of the ANN

Algorithm

Having set up algorithms for characterizing features in CT images of the lung, an ANN based classifier for assigning ROI of an image to a particular class, based on back-propagation algorithm was developed (Appendix III). The number of classes affects the classification accuracy of any classifier. Ideally, features would be uncorrelated and information overlap between features is minimal. Large number of ROI's preferably, in hundreds if not thousands of labelled samples should be available. For the backpropagation ANN algorithm, large number of data, labelled with specific classes, will help sharpen class boundaries. A leave-one-out method was employed for measuring the classification accuracy. In the literature, SVM and K-nearest are often used in classification assessments of DLD patterns. However, both of these classifiers use distance functions and features discussed in this thesis go beyond distance metrics, and because they are not limited by

heterogeneity and can have different scales, ANN was preferred. For more information on ANN, K-Nearest and SVM, refer to Appendix III. Training an ANN based on back-propagation technique requires several thousands of iterations so that class boundaries are adequately formed. There were 229 patients in the data sets whose CT images were available for analysis. From these images a total number of 1165 ROIs were extracted. The ANN was trained based on 1165 patterns which approximately ran through 12550 iterations for training each combination of classes, with 10 neurons of one hidden layer. ANN inputs are vectors of the size equal to the number of features extracted based on the methods described in each chapter and the output neurons are defined based on 10 DLD of patterns and an output neuron specifically for healthy ROI's. Individual number of patients and ROI's for each pathology is listed in the Table 3.1.

IV. Results of Classification of CT images of the lung Based on SIFT

Features

SIFT descriptors, which is a 128 feature vector, are extracted from each ROI and used for training an ANN. Figure 5.1 shows classification accuracy based of scale invariant feature transform method. The classification accuracy based on SIFT features is higher than those obtained from classifier using texture features. Since SIFT analysis has never been used before on DLD patterns with eleven pathologies involved, the training and classification results in this chapter shows that SIFT based analysis can assist with quantitative assessment during diagnosis of specific ROI's in radiology.

Training results using SIFT are comparable to those obtained by classifier that uses a combination of texture and fractal features together. ANN provided an accuracy of 99.99%

for two classes of pathological conditions, except for nodularity and healthy lung which is 94%. The reason classification of CT images containing nodular regions did not reach the accuracy of other DLD patterns is because it identifies blood vessels in a healthy lung as nodules; if the resolution is very poor and the size matches a nodularity ROI. Although ANN was trained over several thousand iterations, classification based on SIFT features frequently reached average classification accuracy of 98% or higher, with three classes, included the ROI of a healthy lung.

Abnormality						
GGO	71%	87%	96%	98%		99.1%
Consolidation						100%
Scar						99%
Cyst			92%	97%		99.3%
Emphysema						100%
Reticulation	88%		97%	98%	88%	100%
HoneyCombing				98%		100%
Fibrosis					100%	
Nodularity			98%			94%
Tree in bud						100%

Table 5.1 ANN classification accuracy based on SIFT features

Having an ANN that yields a high level of accuracy is shown in the table 5.1, is an affirmation of the concept that SIFT analysis generates features with non-overlapping and complementary characteristics with Haralick texture features and those based on Fractal analysis.

V. Results of Classification of CT images of the lung using SIFT and Texture Features

As described in the previous section, SIFT features have shown promising results for training an ANN to classify ROIs of a variety of DLD patterns. Since texture features are the most widely used features in the literature for classifying CT images and yield high accuracy of classification, one could combine them with features obtained from SIFT. Therefore, it is conceivable that an ANN trained on a combination of SIFT and Haralick texture features can provide a more accurate learning paradigm when multiple classes are involved. Such a study, evaluating classification accuracy was conducted on the dataset of 1150 ROIs from CT images collected in our laboratory.

Abnormality						
GGO	86.2%	93.8%	99.9%	99.9%		99.9%
Consolidation				99.9%		99.9%
Scar			99.9%	99.9%		99.9%
Cyst				99.9%		99.9%
Emphysema	94.3%		99.9%	99.9%		99.9%
Reticulation				99.9%	99.9%	95.1%
HoneyCombing			99.9%	99.9%		99.9%
Fibrosis				99.9%		99.9%
Nodularity			99.9%	99.9%		99.9%
Tree in bud				99.9%		99.9%

Table 5.2 ANN classification accuracy based on SIFT and all texture features

Table 5.2 shows classification accuracies of an ANN trained with a combination of SIFT and Haralick texture features. Although results are slightly reduced with the increase in the number of classes, the accuracy of classification has increased significantly for a

combination of classes compared to texture features. The uniqueness in these results lies in the accuracy and also in the number of classes being studied.

The combination of features has especially affected the classification accuracy when reticulation, honey combing and fibrosis are involved. Differentiating these patterns with texture Haralick based features alone has 10% to 15% less accuracy. And for the first time, comparing two DLD classes and a normal lung together had a higher accuracy in comparison with classification accuracy of each class with a normal lung in the case of nodularity.

VI. Accuracy of Classification Based on A Combination of SIFT and Texture and Fractal Features

Fractal analysis proved to be useful in increasing the training and classification accuracy of NN when added to all texture features. Table 5.3, demonstrates the performance improvement when texture and fractal features are coupled with SIFT features.

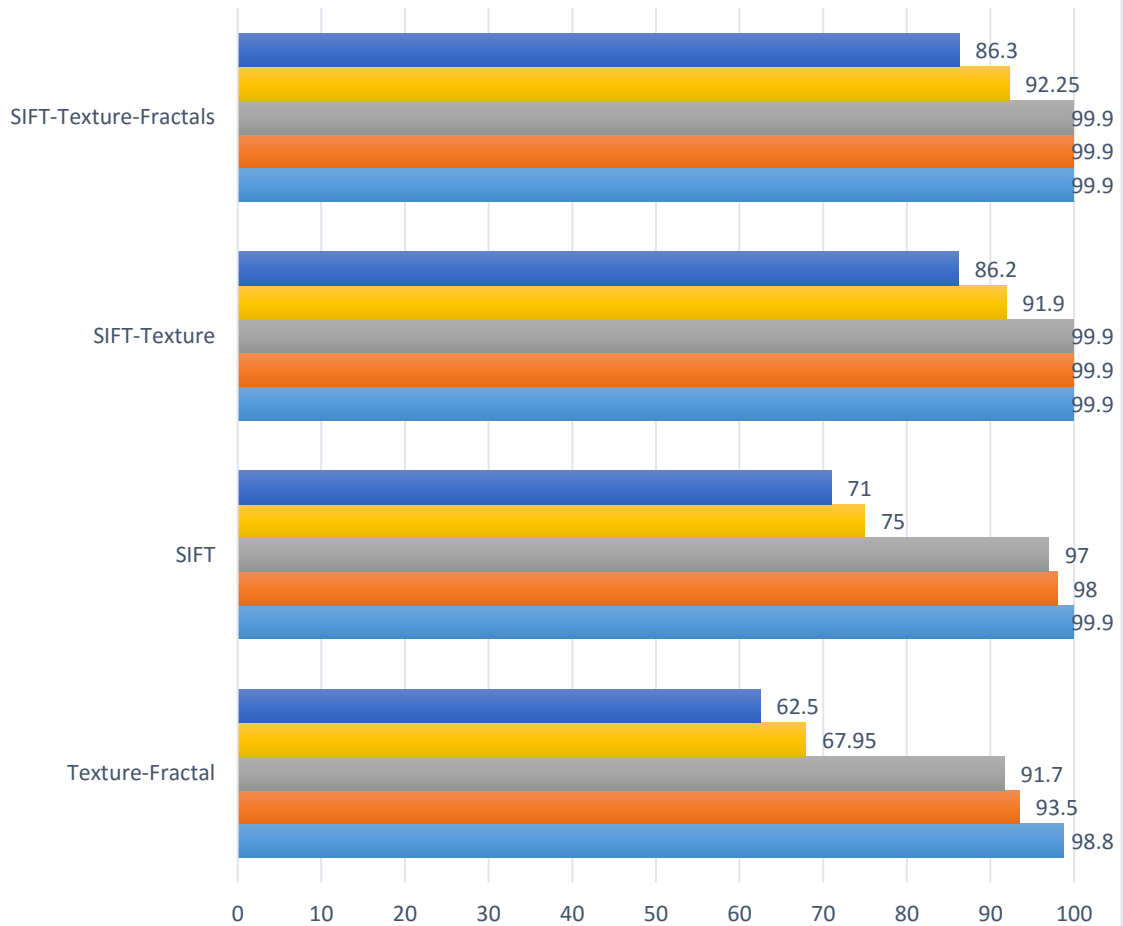
Abnormality						
GGO	86.3%	93.9%	99.9%	99.9%		99.9%
Consolidation				99.9%		99.9%
Scar			99.9%	99.9%		99.9%
Cyst				99.9%		99.9%
Emphysema	94.6%		99.9%	99.9%		99.9%
Reticulation				99.9%	99.9%	95.3%
HoneyCombing			99.9%	99.9%		99.9%
Fibrosis				99.9%	99.9%	99.9%
Nodularity			99.9%	99.9%		99.9%
Tree in bud				99.9%		99.9%

Table 5.3 Accuracy of ANN classification of CT lung images using SIFT, for texture and features from fractal description of the image

VII. Results

Classification accuracies are relatively high when SIFT based features are incorporated in the feature set, along with Haralick texture based features (according to tables 5.2 and 3.9). Pattern recognition strategies for classifying DLD patterns obtained from CT images of the lung have been studied using texture quantification methods, for more than a decade and the attention toward a method that is scale and rotation invariant is of significant usefulness and is the primary topic of this chapter. With findings reported in this chapter, it is worth noting that a professional radiologist could employ features generated by both SIFT and texture into consideration. To better identify an irregular pattern, not only the appearance and surface changes matters to professional eyes, but zooming in and out and analyzing changes could be useful. Besides, these images and features thereof may be identified as being pathological when examined from various angles. SIFT also minimizes illumination and noise effects during feature extraction. SIFT features are not identified through texture analysis, therefore their combination with other features described in chapter 2-4, perhaps provides additional knowledge and may enhance the classification accuracy. Thus, in summary, SIFT along with texture analysis provides a set of features with high specificity. Texture features may not be needed to classify a ROI when up to 4 classes are involved, but in many CT images of the lung, several irregular patterns are present and an ANN that can classify as many 10 pathologies compared to healthy lung which is likely to be more favourably viewed by radiologists.

Figure 5.19 Comparison of the classification accuracy of the combination of features in chapters 3, 4 and 5 for different number of classes



	Texture-Fractal	SIFT	SIFT-Texture	SIFT-Texture-Fractals
■ 11 Classes	62.5	71	86.2	86.3
■ 7 Classes	67.95	75	91.9	92.25
■ 4 Classes	91.7	97	99.9	99.9
■ 3 Classes	93.5	98	99.9	99.9
■ 2 Classes	98.8	99.9	99.9	99.9

■ 11 Classes ■ 7 Classes ■ 4 Classes ■ 3 Classes ■ 2 Classes

From Figure 5.19 one can conclude that classification accuracy increases when both statistical texture and scale invariant features are combined, for classification. SIFT features and statistical texture features provide the highest accuracy for increasing number of classes, with 99.9% accuracy for up to 4 classes, which includes the healthy lung as a distinct class.

When SIFT features are combined with the features from Haralick texture and fractal analysis, classification accuracy of all 11 classes becomes about 10% more accurate than classification accuracy of 7 classes when SIFT is not included.

VIII. Chapter Summary

This chapter presented the SIFT feature extraction method, step by step through a flow chart, a detailed description of the algorithm and by demonstrating the results of performing SIFT on several images with DLD patterns. Our results show that the 128 feature vector, resulting from the SIFT method yields features that are more descriptive in terms of their ability to separate images of different pathologies than all texture and fractal methods combined. Training and classification accuracies become significantly higher when features from SIFT are used. Furthermore, when features derived from SIFT are combined with features derived from texture and fractal analysis, classification accuracies become significantly higher than those reported in any previous research in this field. Classification accuracy of combined features is nearly 100% for a combination of images from four pathological conditions. When CT images from 11 classes, which includes images from healthy subjects as a class, the accuracy of classification is 86.3%. To conclude, SIFT features contain sufficient discriminatory power for classifying up to 3 pathological classes

and the healthy lung, but the combination of features derived from SIFT and from Haralick based texture descriptors, results in a high level of performance.

CHAPTER 6

CLASSIFICATION ACCURACY OF TEXTURE, FRACTAL AND SIFT METHODOLOGIES USING 5-FOLD CROSS VALIDATION ON ANN

I. Introduction	149
II. 5-Fold Cross Validation Technique	149
III. Classification Accuracy Based on Texture Features	152
IV. Classification Accuracy Based on Fractal and Texture Features	162
V. Classification Accuracy Based on SIFT, Texture and Fractal Features	164
VI. Comparison of Classification Accuracy of Leave-one-out and 5-Fold Cross validation	167
VII. Chapter Summary	170

I. Introduction

The classification of ROIs obtained from CT lung images thus far in this thesis, have been based on features derived primarily from texture, fractal and SIFT methods. Leave-one-out (L1) method was used for evaluating how various classes of features performed and how effective they were in classification. In the present chapter, a 5-fold cross (5F) validation technique is used to develop a practical evaluation of the features using multiple strategies described in chapters 2-5, for classification of CT images with DLD patterns. Such a procedure helps to highlight features which are statistically with high specificity and provides greater confidence in various features.

II. 5-Fold Cross Validation Technique

In n-fold cross validation described in this chapter, one divides all image patterns (ROI's in the present research) into n number of groups. For each iteration of classification, only $\frac{1}{n}$ of the data is used for testing and the rest is used for training the classifier¹⁴⁹. Through such procedure, classifiers developed for the research reported in the thesis take advantage of using features extracted from all ROI's and test results will not depend only on a particular set of data. In theory, L1 cross validation provides the highest classification accuracy if the extracted features are sufficiently specific, but such a method is not always practical. The time used for testing and classifying with 5-fold is more than leave-one-out, and the difference depends on the number of inputs (ROI's). For instance if 50 ROI's are available for classification, in each ANN learning iteration, 40 ROI's are used for 5-fold, but there will be 5 testing iterations. However, for L1 method 49 ROIs are used for evaluation. For testing purpose, leave-one-out and 5-fold use 1 and 10 ROI's, respectively.

Since the number of patients and ROI's (1165 regions of interest for 11 pattern classes including the healthy lung) were limited in this study, the right number of cross validation had to be determined to match all patterns. For some DLD patterns such as Tree in Bud, Scar and Fibrosis there were only 19, 25 and 38 ROI's respectively, while there were 250 ROI's for GGO and 150 ROI's for Emphysema. Many researchers use 10-fold validation¹⁴⁹, but since the research reported in this thesis did not have access to blinded data, a 5-fold cross validation technique was used at each iteration.

Figure 6.1, demonstrates the process of setting up iterations for training ANN based classifiers. The blue area is the proportion of the data used for training and the orange area is the proportion (80%) of the test data. For the leave-one-out, only one ROI is randomly chosen for testing, but in case of 5-fold cross validation, 20% of ROI's of each class is assigned for the testing purpose and is not used for designing the classifier. For the 5-fold evaluation, the data is randomly partitioned into 5 subsamples. The cross-validation process is then repeated 5 times, with each of the subsamples used exactly once as the validation data. The classification accuracy from all five iterations from each round of testing is then averaged.

The advantage of 5F method over repeated random sub-sampling leave-one-out method is that all observations are used for both training and validation, and each observation is used for validation exactly once. However, leave-one-out method chooses a sample test case randomly, therefore, validation may not use all observations.

As with other validation methods, cross validation also has limitations. The limitation is quite serious when the validation and training sets are from different populations. For

instance, suppose we are interested in validating a model that predicts the risk of a patient being diagnosed with a certain disease. If the training data sets are confined to studies based on male candidates and our individual in question is a female, then cross validation may not provide a correct estimate. Other factors such as age, ethnicity work environment and other factors can also affect the model validation. However, for the present dissertation, the training and testing sets are from the same sample/population and results will not be affected by the above limitations.

The learning process, which includes the training of an ANN does not use testing data to compute probabilities, therefore, the system does not have a *apriori* knowledge of the data generation. At each iteration, only training sets are used, and then based on the testing set, classification accuracy is assessed and averaged over the results of each iteration.



Figure 6.1 The 5-fold Cross validation for classification assessment; each row represents an iteration. Blue areas are the training sets and orange area is the testing set

Another validation technique is to randomly leave 30% of data out, for instance. But using only 70% of the data to design the classifier can lead to a classifier with diminished accuracy.

III. Classification Accuracy Based on Texture Features

Classification results presented in Table 6.1 are based on 5-fold cross validation method. These tables were generated in a manner similar to that described in chapter 3. However 5F validation technique was used in the present context. With 5-fold cross validation method the performance and accuracy is very similar to leave-one-out method with fewer classes involved for classification and when the features are combined. These results suggest that extracted features can characterize each ROI of each class to a high degree of accuracy that increasing the size of the test data set does not affect results reported in this thesis significantly.

Tables 6.1 to 6.2 provides descriptions, comparing the results obtained in chapters 3, 4 or 5 with leave-one-out method. The entries of accuracy along the X-axis of the table represents the percentage accuracy of classification.

Table 6.1 demonstrates classification accuracy based on 5-fold cross validation for Tamura's coarseness feature. Using the leave-one-out, classification accuracy has dropped by 4.5% when classifying two classes. The result has affected classification of all eleven patterns by a 50% decrease (compared to with table 3.3, figures 3.25 and 6.1).

Abnormality							
GGO	13.3%	22%	34%	41%		53%	
Consolidation							44.43%
Scar							
Cyst			39%	37%		58.15%	
Emphysema							54.2%
Reticulation							
HoneyCombing		18%	22%	51%	29%	62%	
Fibrosis				42%			59.6%
Nodularity			38%			59%	
Tree in bud							40.3%

Table 6.1 ANN average classification accuracy based on Tamura’s coarseness feature

Table 6.2 demonstrates classification accuracy based on 5-fold cross validation for Tamura’s contrast feature. Classification results have decreased from an average of 53% for three classes to 44%. And, classification accuracy of eleven classes has fallen from 22.2% to 12.7% with leave-one-out and 5-fold cross validation, respectively (compared to table 3.4, figures 3.25 and 6.1).

Abnormality							
GGO	12.7%	20%	32%	39%		51.5%	
Consolidation							43.3%
Scar							
Cyst			38%	35%		55.1%	
Emphysema							52.7%
Reticulation							
HoneyCombing		17%	19%	48%	27%	60.5%	
Fibrosis				41%			53%
Nodularity			37%			57.7%	
Tree in bud							42.1%

Table 6.2 ANN average classification accuracy based on contrast; a Tamura texture feature

Table 6.3 demonstrates classification accuracy based on 5-fold cross validation for Tamura’s directionality feature. Classification accuracy of five and eleven classes has dropped by 10% comparing to leave-one-out method (comparing with table 3.5, figures 3.25 and 6.1).

Abnormality							
GGO	10.1%	16%	26%	33%		43.7%	
Consolidation				26%			44.3%
Scar			29%	26%		20%	
Cyst				26%			46%
Emphysema				26%			47.2%
Reticulation		15%	16%	41%	35%	53.2%	
HoneyCombing				35%		52%	
Fibrosis			16%		35%		49.6%
Nodularity			32%		35%		38%
Tree in bud			32%		35%		39%

Table 6.3 ANN average classification accuracy based on directionality; a Tamura texture Feature

Table 6.4 demonstrates classification accuracy based on 5-fold cross validation when all Tamura features were combined. It is expected that the accuracy should decrease with 5-fold validation, but it is interesting that for combined features the difference with leave-one-out is at its minimum. Accuracy of classification for eleven classes has dropped (comparing with table 3.6, figures 3.25 and 6.1) by about 6% and for two classes, the difference is at 5%. One can conclude that in general, there is no perfect feature from any kind of feature extraction method. Only a combination of multiple features provides higher accuracy of classification.

Abnormality								
GGO	22%	38%	50%	67%		78%		
Consolidation							79%	
Scar							58%	
Cyst			59%	54%		38%	76%	
Emphysema							77%	
Reticulation		34%	41%	60%			78%	
HoneyCombing						61%	78%	
Fibrosis							65%	
Nodularity			47%					70%
Tree in bud								61%

Table 6.4 ANN average classification accuracy based on all three Tamura texture features shows better results compared to when only one of the features were used

Table 6.5 demonstrates classification accuracy based on 5-fold cross validation of CLBP. Although classification accuracy using CLBP is less than combined Tamura features, but the effect of 5-fold cross validation was less. With eleven classes, there is a difference of only 3% in the accuracy of classification when compared to leave-one-out method (comparable to table 3.7, figures 3.25 and 6.1).

Abnormality								
GGO	19%	26%	37%	43%		54.3%		
Consolidation							44.8%	
Scar							36.9%	
Cyst			46%	41%		37%	57%	
Emphysema							59.3%	
Reticulation		28%	39%	57%			60.8%	
HoneyCombing						52%	61%	
Fibrosis							58.8%	
Nodularity			42%					66.8%
Tree in bud								54%

Table 6.5 ANN average classification accuracy based on CLBP

Table 6.6 demonstrates classification accuracy based on 5-fold cross validation of GLCM. Classification accuracy of GLCM is higher than CLBP with any validation method, but GLCM had 3.6% decrease when classifying eleven classes with 5-fold validation (comparable to table 3.8).

Abnormality						
GGO	20%	37%	52%	67%		70%
Consolidation				71%		
Scar			56%		36%	
Cyst			57%	72%		
Emphysema				73%		
Reticulation		34%	43%	57%	59%	70%
HoneyCombing				74%		
Fibrosis			62%			
Nodularity			46%			69%
Tree in bud						58%

Table 6.6 ANN average classification accuracy based on GLCM shows better results compared to single Tamura features

Table 6.7 demonstrates classification accuracy based on 5-fold cross validation of all Haralick features. These features have provided the highest accuracy among any number of classes both with leave-one-out and 5-fold validation (comparable to table 3.9, figures 3.25 and 6.1). There is a decrease in accuracy by 3.8%, when comparing leave-one-out and 5-fold methods on eleven classes and there is only 1% difference when comparing other 7 classes.

Abnormality														
GGO	26%	41%	55%	69%		79%								
Consolidation				41%	58%		41%							
Scar			60%			63%		78%						
Cyst									46%	62%	79%			
Emphysema			40%	49%	63%	68%								
Reticulation		41%					63%	72%						
HoneyCombing									41%	63%	59%			
Fibrosis												41%	63%	59%
Nodularity														
Tree in bud			41%	63%	59%									

Table 6.7 ANN average classification accuracy based on all thirteen Haralick texture features shows best classification results among all other methods

Table 6.8 demonstrates classification accuracy based on 5-fold cross validation of all Gabor features (IFFT, energy and transformed IFFT). Classification accuracy is lower with 5-fold validation in this method too. Average decrease is less than 4% for two classes. And accuracy of classification is about 3% less for eleven classes with 5-fold method. (Comparable to table 3.13, figures 3.25 and 6.1)

Abnormality														
GGO	22.5%	34%	45%	48%		57%								
Consolidation				34%	42%		37%							
Scar			46%			51%		62%						
Cyst									44%	52%	63%			
Emphysema			35%	44%	51%	56%								
Reticulation		37%					51%	58%						
HoneyCombing									37%	51%	50%			
Fibrosis												37%	51%	50%
Nodularity														
Tree in bud			37%	51%	50%									

Table 6.8 ANN average classification accuracy based on all three Gabor filter texture features shows better results than when only one of the features were used

Table 6.9 demonstrates classification accuracy based on 5-fold cross validation of Minkowski Functionals (MF). The classification accuracy is at its lowest when it comes to MF features. But one can observe that, the decrease in validation from leave-one-out to 5-fold method is at its lowest too (comparable to table 3.14, figures 3.25 and 6.1). This means that, although MF are not very descriptive, especially when it comes to classifying patterns where shapes are not of importance, but they do play an effective role in classification. This effect is clearly visible when all features are combined. For instance, honey combing and emphysema has the highest accuracy, because their morphological characteristics can be identified by MF.

Abnormality							
GGO	13.2%	19.7%	28%	34%		43%	
Consolidation							35%
Scar					30.8%	25%	
Cyst			31%			43%	
Emphysema						49%	
Reticulation		18.8%		40%	21%		50%
HoneyCombing					32%		
Fibrosis				34%		40%	
Nodularity				33%			48%
Tree in bud							35%

Table 6.9 Average accuracy of classification for Minkowski geometric Functionals

Average classification accuracies for all texture features are combined in table 6.10 for different combinations of DLD patterns. Similar to the leave-one-out, 5-fold cross validation also demonstrates considerable increase in the accuracy when all texture features are combined for classification of ROIs. These results lead to the conclusion that, each feature captures a unique characteristic of the image and combination of features obtained

through multiple methods provides improved accuracy. An example from face recognition is that, we can identify a face by eyes, nose, fore-head, chin or chick and combining these features will give a more complete definition of the face. The same is applied for lung DLD patterns. To know about the directionality, coarseness, contrast or MF of a ROI are useful pieces information, and their combination results in a more complete quantification.

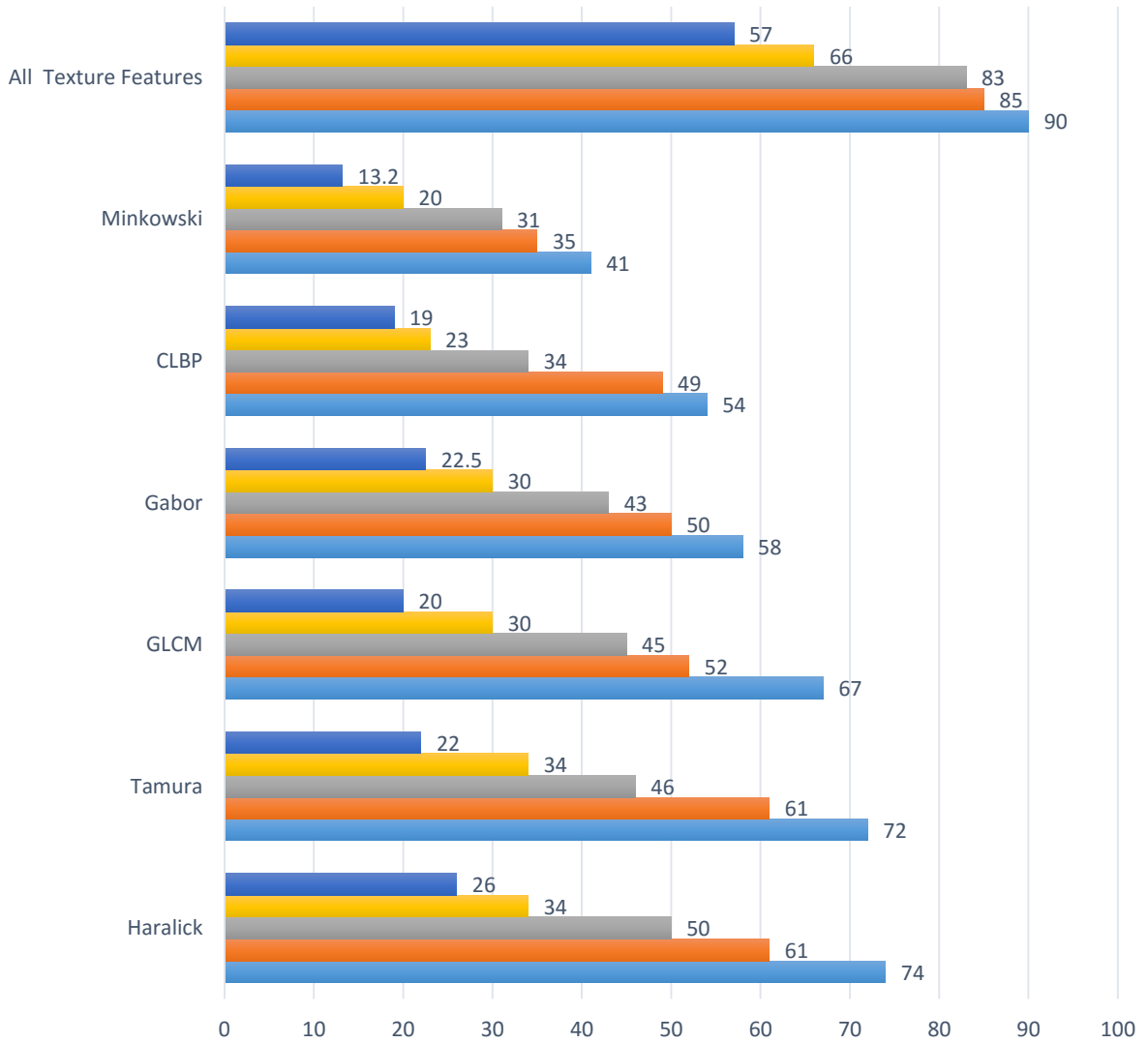
Abnormality							
GGO	57%	70%	87%	91%		95%	
Consolidation							96%
Scar							
Cyst			90%	89%		94%	
Emphysema							96%
Reticulation		63%	72%	82%	80%	97%	
HoneyCombing				77%			98%
Fibrosis						85%	
Nodularity			83%				89%
Tree in bud						77%	

Table 6.10 ANN average classification accuracy based on all texture features shows a well-trained ANN ready for classification

The number of ROI for scar, fibrosis and tree in bud are much less compared to other patterns. Therefore, during 5-fold validation which uses only 80% data for design of classifiers and allows 20% of that data for testing, it affects the training process of ANN and provides lower classification accuracy. Most classes had 2% to 6% decrease when classifying two classes. In addition, the accuracy for scar, fibrosis and tree-in-bud patterns has dropped considerably more, due to a smaller number of ROIs in these classes, as shown in table 3.1. Tables 6.1 to 6.10 are summarized in Figure 6.1. Classification accuracies with 5-fold cross validation are generally lower than that for leave-one-out method but the accuracies of each feature and their combination are similar to that due to leave-one-out

method. This becomes clearer when one is interested in analysing the most descriptive features, effects of combining the features or the usefulness of the features in quantifying DLD patterns of the lung. Figure 6.1 demonstrates classification results based on Haralick, Tamura, GLCM, Gabor, CLBP, MF and the combination of these features which are assessed based on 5F validation technique. The results are comparable to Figure 3.25.

Figure 6.1. Classification Accuracy of Texture Features based on 5-fold Cross validation on ANN



	Haralick	Tamura	GLCM	Gabor	CLBP	Minkowski	All Texture Features
■ 11 Classes	26	22	20	22.5	19	13.2	57
■ 7 Classes	34	34	30	30	23	20	66
■ 4 Classes	50	46	45	43	34	31	83
■ 3 Classes	61	61	52	50	49	35	85
■ 2 Classes	74	72	67	58	54	41	90

■ 11 Classes ■ 7 Classes ■ 4 Classes ■ 3 Classes ■ 2 Classes

IV. CLASSIFICATION ACCURACY BASED ON FRACTAL AND TEXTURE FEATURES

Table 6.11 demonstrates classification accuracy of fractal features based on 5-fold cross validation on ANN for different number of classes, compared with healthy ROI's of the lung.

Abnormality								
GGO	14.5%	23%	34%	38%		43%		
Consolidation						46%		
Scar					29%	41%		
Cyst			31%			48%		
Emphysema						47%		
Reticulation	19%	19%	19%	31%	37%	52%		
HoneyCombing						29%	48%	
Fibrosis								43%
Nodularity								49%
Tree in bud								41%

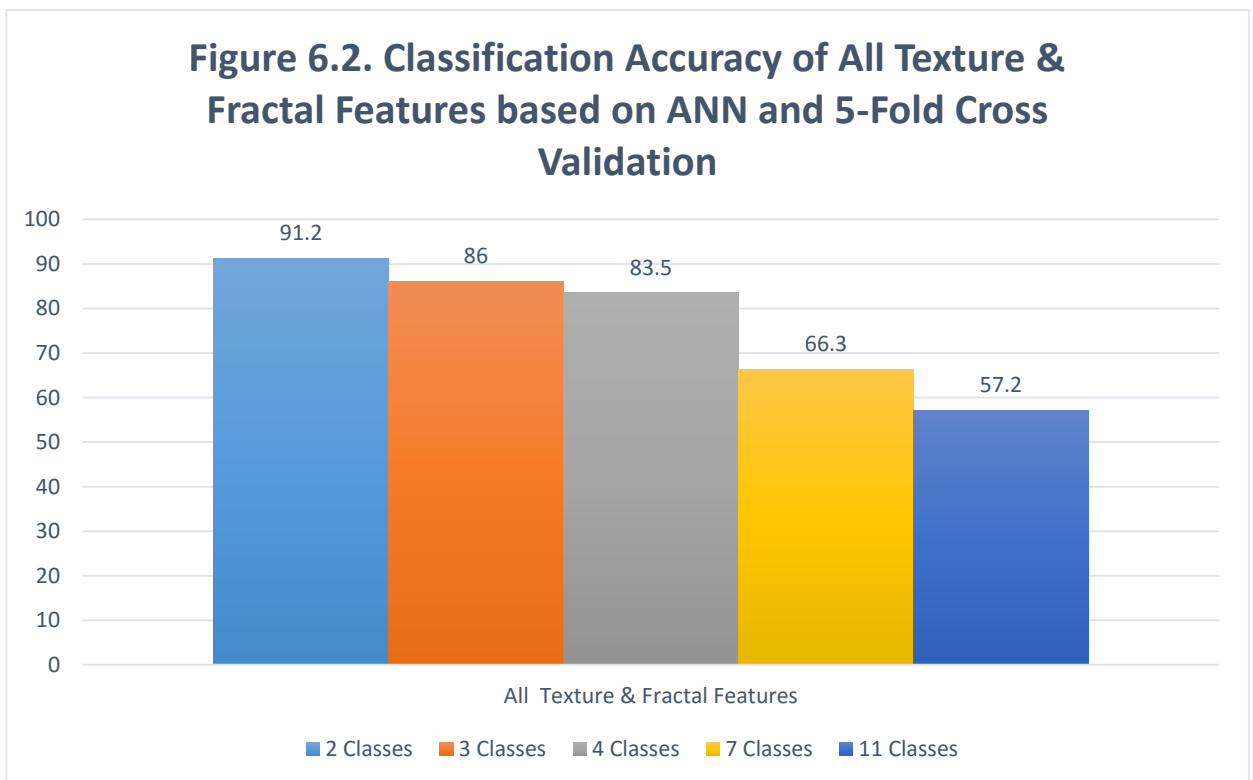
Table 6.11. ANN classification accuracy based on all Fractal Dimension features

Table 6.12 shows the classification accuracy of fractal and texture features combined. The accuracy of classifying two classes when comparing 5-fold with leave-one-out methods are 91.2 and 98.8 percent, respectively. The accuracy has dropped from 93.5% for three classes to 86%, and from 62.5 to 57.2 for eleven classes (Comparable to table 4.5, figures 4.8 and 6.2).

Abnormality						
GGO	57.2%	71%	87.4%	91.5%		96.2%
Consolidation				97.1%		
Scar			89.4%		80.2%	95.3%
Cyst			90.5%			
Emphysema	63.3%	72.3%	82.5%	80.2%		98%
Reticulation				98%		
HoneyCombing			77.6%	98.7%		
Fibrosis				86%		
Nodularity			83.7%		90.2%	
Tree in bud			79%			

Table 6.12. ANN classification accuracy based on all FD and all Texture features

Classification results are provided in figure 6.2 based on the combination of features in chapter 3 and 4 on different number of classes and 5-fold cross validation on ANN. Figure 6.2 is comparable to Figure 4.8.



V. Classification Accuracy Based on SIFT, Texture and Fractal Features

Table 6.13 demonstrates classification accuracy of SIFT based on 5F on ANN. The accuracy for eleven classes has decreased by 3%, and the results for two classes were 99.9% and 98% with leave-one-out and 5-fold cross validation, respectively (comparable with table 5.1, figures 5.19 and 6.3).

Abnormality							
GGO	68%	82%	94%	97%		98%	
Consolidation				97%			
Scar				95%			
Cyst			91.2%	96.3%		99%	
Emphysema				98%			
Reticulation		81%	95%	97.1%	86%	98%	
HoneyCombing				97%		97%	
Fibrosis				96%			95%
Nodularity							96%
Tree in bud							93%

Table 6.13. ANN classification accuracy based on SIFT features using 5-fold cross validation

Table 6.14 shows 16% increase in classification accuracy when combining SIFT with texture features, even with 5-fold cross validation (compared to table 5.2, figures 5.19 and 6.3). There is a decrease of 1.2% from leave-one-out to 5-fold cross validation when classifying two classes with texture and SIFT on ANN.

Abnormality								
GGO	84%	92%	97.4%	97.6%		99%		
Consolidation						98%		
Scar							96.3%	
Cyst			96.8%	97.9%		90.5%	99.9%	
Emphysema				99%				
Reticulation		93%	95.2%	97.9%			99.9%	
HoneyCombing				97.4%		99.9%		
Fibrosis							99.9%	
Nodularity			97.7%					98%
Tree in bud								95%

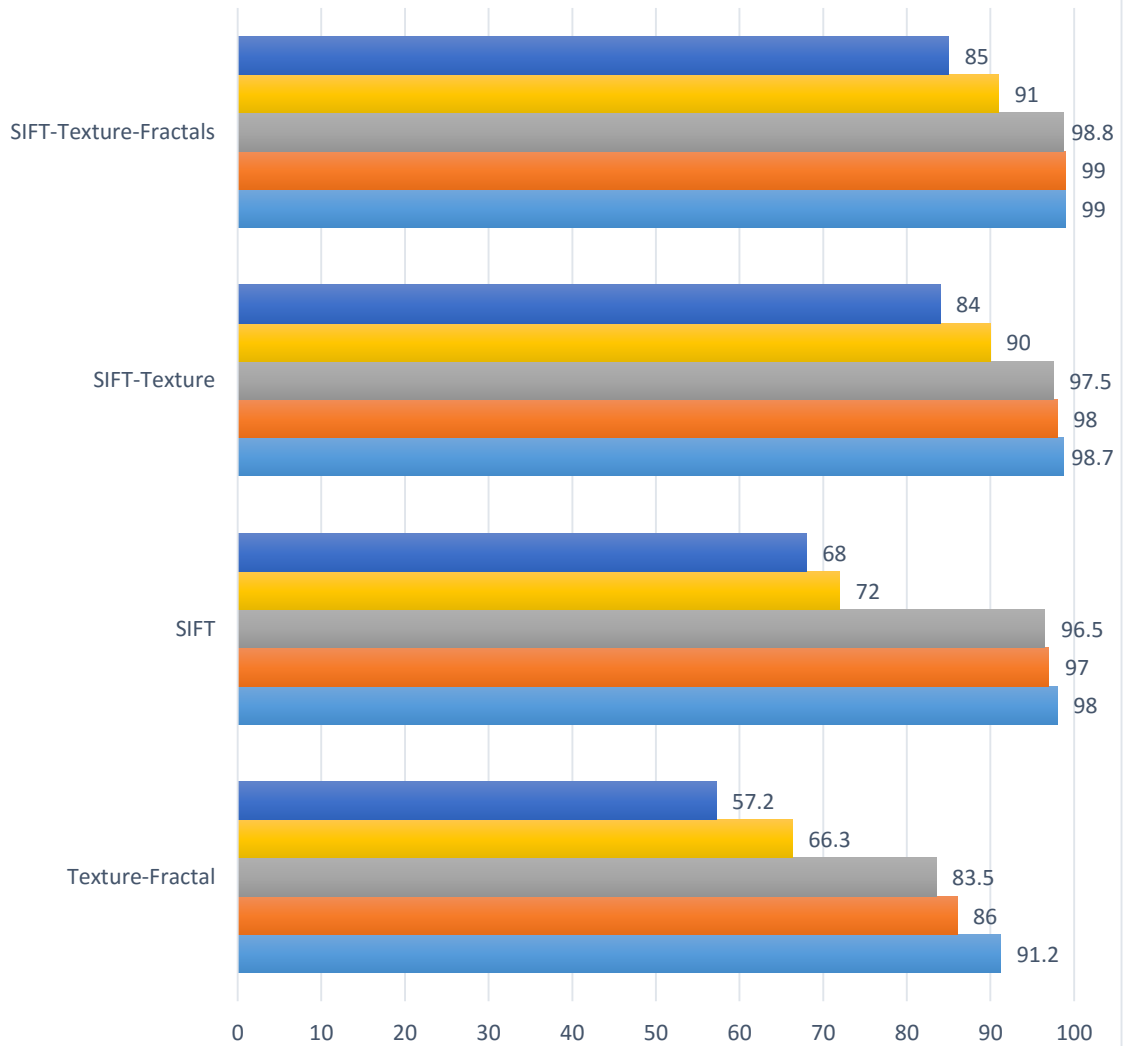
Table 6.14. ANN classification accuracy based on SIFT and all texture features

Table 6.15 shows classification accuracy has increased further with the addition of fractal features along with SIFT and all texture features. There an increase of at least 1% on any combination of classes with 5-fold cross validation (comparable to table 5.3, figures 5.19 and 6.3).

Abnormality								
GGO	85%	93%	98%	98.3%		99.3%		
Consolidation						98.3%		
Scar							96.7%	
Cyst			97.5%	98%		91%	99.9%	
Emphysema				99.5%				
Reticulation		94%	96%	99%			99.9%	
HoneyCombing				99%		99.9%		
Fibrosis							99.9%	
Nodularity			98.1%					98.6%
Tree in bud								95.5%

Table 6.15. ANN classification accuracy based on SIFT, all texture and FD features

Figure 6.3. Comparison of Classification Accuracy of All Texture, Fractal and SIFT features Based on 5-Fold Cross validation on ANN



	Texture-Fractal	SIFT	SIFT-Texture	SIFT-Texture-Fractals
■ 11 Classes	57.2	68	84	85
■ 7 Classes	66.3	72	90	91
■ 4 Classes	83.5	96.5	97.5	98.8
■ 3 Classes	86	97	98	99
■ 2 Classes	91.2	98	98.7	99

■ 11 Classes ■ 7 Classes ■ 4 Classes ■ 3 Classes ■ 2 Classes

VI. Comparison of Classification Accuracy of Leave-one-out and 5-Fold

Cross validation

Throughout chapter 6, we have demonstrated the classification accuracy of each texture, fractal, SIFT features and their combinations based on 5-fold cross validation on ANN for different number of classes. These results are compared for each feature set with those obtained for leave-one-out method, demonstrated throughout chapters 3, 4 and 5.

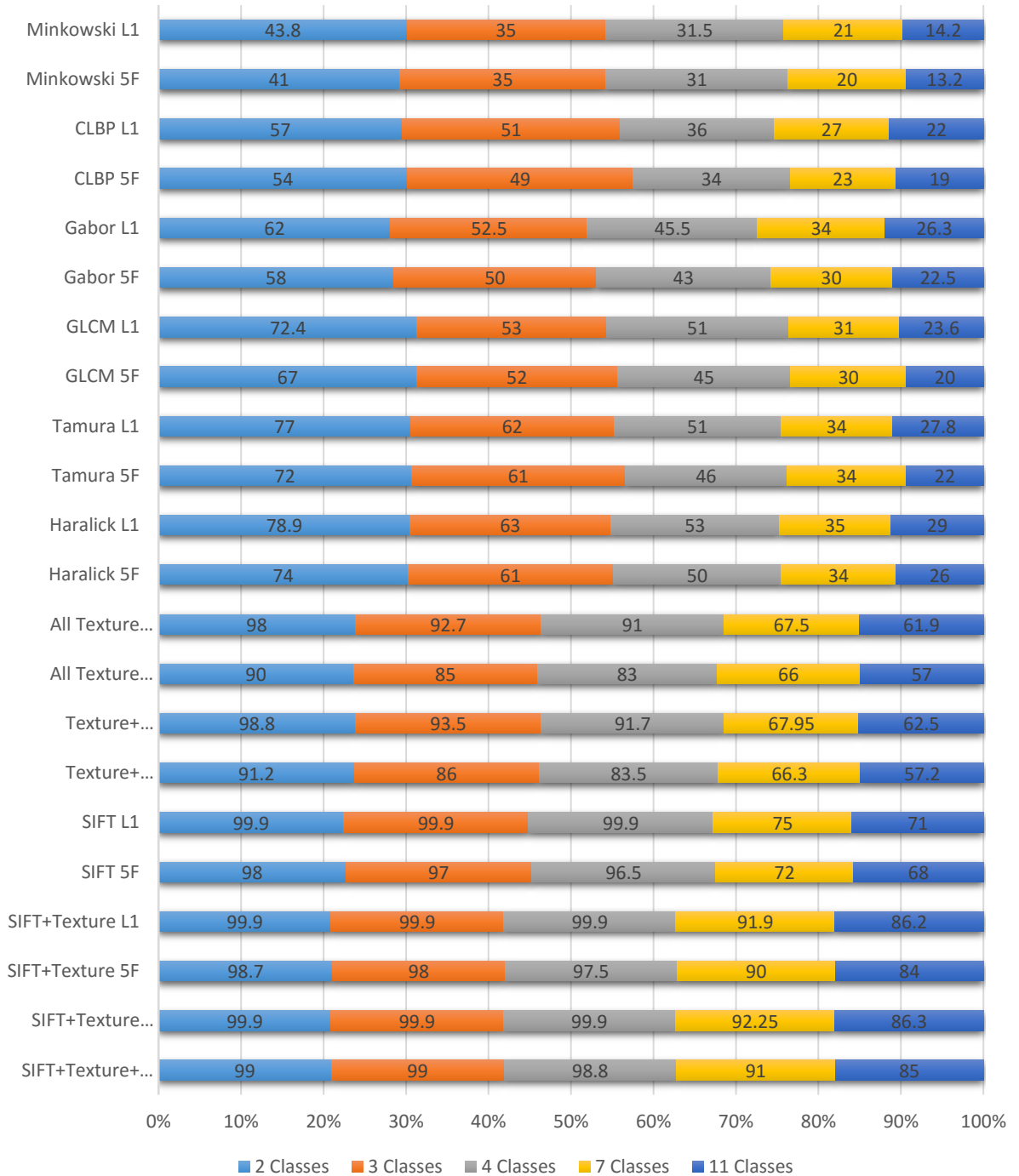
Figure 6.4 summarizes results of comparing classification for various classes of features described in chapters 3 to 6 so that they can be assessed and visualized in one place.

This figure shows a uniform decrease in classification accuracies, when 5-fold cross validation is compared with leave-one-out method. Such a result is to be expected because when the ANN is trained, it will create the relationships and learning patterns based on fewer number of ROI's and therefore fewer number of data points.

Also, testing such a model generated based on this learning process is more rigid when compared to leave-one-out, and consequently ANN using 5F results in a lower accuracy. However, the descriptiveness of each feature and their combination is still useful, because the accuracy is relatively high (99% for 2 classes). Classification accuracy for any combination of classes up to seven classes is higher than 91%, and for eleven classes it is 85%. The accuracy for up to three classes is 99% which demonstrates a reasonably accurate quantification of texture within the ROI.

In figure 6.4 L1 refers to classification accuracies to leave-one-out and 5F refers to classification accuracies to 5-fold cross validation methods. Classification results of 2, 3, 4, 7 and 11 classes are demonstrated for both types of validations. These results suggest that the accuracy decreases with increased number of classes, due to the fact that the class boundaries become more complex with more number of classes.

Figure 6.4. Comparison of Classification Accuracy of All Texture, Fractal and SIFT features Based on 5-Fold Cross validation and leave-One-Out Methods on ANN



VII. Support Vector Machine Classification Results on SIFT

Several laboratories have provided DLD classification assessment based on different number of classes using SVM. In order to provide a classification accuracies between ANN and SVM for SIFT features from all the ROI’s, we ran our data through SVM.

Abnormality			
GGO	91%	95.7%	97.3%
Consolidation			96.8%
Scar			93%
Cyst	91%		98.7%
Emphysema			98%
Reticulation	93.9%	96.4%	97%
HoneyCombing			96.6%
Fibrosis		96.5%	95.5%
Nodularity	95%		95%
Tree in bud			91.2%

Table 6.16. SVM classification accuracy based on SIFT features using 5-fold cross validation

Table 6.16 demonstrates classification accuracy of all DLD patterns based on SIFT features using an SVM classifier. The results are similar to those of the ANN classifier when comparing similar number of classes.

VIII. Chapter Summary

In the present chapter classification accuracy of ten DLD patterns were evaluated based on 5-fold cross (5F) validation of ANN using features from texture, fractal dimension, SIFT and a combination of all features. These results were compared with leave-one-out (L1) method. Classification accuracy is relatively high for both methods when smaller number of classes are present for classification and progressively decreases when more classes are added.

Classification accuracy of texture features are assessed based on the combination of multiple feature extraction methods, whereby features derived from Haralick, Tamura and GLCM algorithms have the highest classification results, and Gabor, CLBP and MF features are less useful for both types of validations. Classification accuracy of texture features drops from 98% to 90% for two classes when assessed with L1 and 5F respectively, however there was only a 3% decrease when comparing eleven classes, for all texture features combined.

Classification accuracy of SIFT features are also lower with 5F compared with L1 but the results are consistently increasing when comparing individual features and their combinations. With 5F, accuracy of eleven classes increased from 68% with SIFT features to 84% with SIFT and texture features combined and to 85% percent when fractal features were added to the SIFT and texture features combination.

CHAPTER 7

SUMMARY AND CONCLUSIONS

I. Introduction	172
II. Research Summary and Conclusion.....	172
III. Contributions	179
IV. Future Work	180

I. Introduction

The research on classification accuracy of feature extraction, from regions of CT images identified with patterns of diffuse lung diseases, led this thesis towards the use of scale invariant feature transform and several texture and fractal features.

Chapter 1, described the problem statement, motivations and limitations of this work. Chapter 2, provided a background of the state of the art, methods and features that other researchers have studied and also the applications, and accuracies in the field of lung quantification was demonstrated. Chapter 3, described and incorporated the most useful texture features based on the state of the art. Chapter 4, described the underlying advantage of using fractal analysis and morphological features. Chapter 5, demonstrated scale invariant feature transform as a unique feature invariant to scale in identifying DLD patterns. And finally chapter 6, used 5-fold cross validation for the assessment of every feature and their combinations that were demonstrated in chapters 3, 4 and 5 to overcome the lack of blind data testing.

This chapter summarises the results that are provided in detail in previous chapters and conclude with the contributions and possible future works.

II. Research Summary and Conclusion

This section summarises ANN classification accuracies achieved with leave-one-out and 5-fold cross validation techniques based on texture, fractal, SIFT and combinations of these features.

DLD patterns are irregular regions of the lung parenchyma which can be identified on CT images. The ten pathological patterns in consultation with an experienced chest radiologists

and which are used in this research are: consolidation, cyst, emphysema, fibrosis, GGO, honey combing, nodularity, reticulation, scar and tree-in-bud. Classification accuracies of combination of these classes, including healthy lung are provided with radiologist's diagnosis as the gold standard.

The number of patients used for this study are 229, whose CT scans were made available by the radiological screening room following confirmed diagnosis. From these, 1165 ROI's of ten DLD patterns and healthy lung were extracted by an expert radiologist at St. Joseph's Hospital, Hamilton, Canada.

ANN is the classifier of choice because the relationships created based on the feed forward algorithm provide fair classification accuracy on large data sets with eleven disease states to be classified. The classifier uses ten neurons in the hidden layer, eleven neuron on the output and 50 input neurons for all texture and fractal features, plus, the number of SIFT key-points extracted from each ROI which depends on the image; but each key-point has a 128 vector size descriptor.

The most powerful texture features demonstrated in chapter 3 are ordered from the strongest to the weakest as: Haralick, Tamura, gray level co-occurrence matrix, Gabor, compound local binary pattern and Minkowski Functionals. A combination of these features results in higher accuracy than using them individually because several aspects of the patterns characteristics are quantified. Haralick features are the most descriptive of all (78.9% for two classes and 63 for three classes), while results based on Tamura features follows closely by 77 and 62 percent for two and three classes respectively. The accuracy drops below 50% especially when more than four classes are present in each method. The

least descriptive of all features is generated by Minkowski Functionals, perhaps due to the fact that texture has a higher influence than morphological based features, on the final classification results. The order of the highest to lowest accuracies for texture features are as follows: Haralick, Tamura, GLCM, Gabor, CLBP and MF. The accuracies for any number of classes is higher with the strongest features, however, with 7 classes, Tamura and Gabor had the same accuracy of 34% (figure 3.25); with 4 classes, Tamura and GLCM had the same average accuracy of 51%. When all features are combined the highest accuracy of classification is achieved (98% for two classes, 92% for three and 61.9% for eleven classes).

Chapter 4, describe and demonstrates fractal dimension (FD) analysis on several DLD patterns. These features are extracted based on: FD semi variance, box counting and segmentation based fractal analysis. Although FD provides scaled features, it is a natural shape detector underneath, as it is theoretically expected. Fractal analysis is not just a dimension value but it also narrows down the basic structure of the whole picture to a descriptor. However, quantification of CT images is not feasible only with fractal analysis, but when combined with texture features, they can contribute relevant information towards identification of irregular patterns with a higher accuracy. Combining features from FD analysis with all texture features slightly increases classification accuracy from 98% to 98.8% when classifying 2 classes, and from 61.9 to 62.5 percent for eleven classes.

Chapter 5 described and demonstrated the SIFT feature extraction algorithm and its application to several DLD patterns. The SIFT uses Gaussian transformation to filter ROI's on several scales and octaves. Based on zero crossing and interval tree, potential key-points

are localized and difference of Gaussians is computed to identify extrema. SIFT does not use edges as features and potential key-points that are on edges will be eliminated from the outcome, using Taylor series and the Hessian matrix. At this point, key-points are identified which are the features of ROI. SIFT's strength is in having a descriptor for each feature, which is assessed using derivatives, gradient magnitude and directions. Classification accuracies are relatively high when SIFT features are incorporated in ANN (>96.5% for up to 4 classes) comparing to those of texture and fractal dimensions (>83% for up to four classes). A variety DLD patterns have been studied under texture quantification for over a decade and the attention toward a method that is scale and rotation invariant has not been examined in detail. With this thesis, there is evidence to support the use of SIFT based features through ANNs, by a professional radiologist while making diagnosis. To better identify pathological pattern, not only the appearance and surface changes matters, SIFT implicitly quantifies zooming in/out and analyses changes by computing the image at different scales and octaves which is the property of affine transformation. Also, these features would be identified on a ROI from any angle because SIFT features are insensitive to rotation. SIFT also prevents illumination and noise variability effects in feature extraction which texture analysis is sensitive to. Furthermore, SIFT generated features cannot be generated with texture analysis, thus, contributing to increased classification performance. Having SIFT features along with texture analysis provides a strong quantification because the new set of features provide non-overlapping characterization of the information contained within the imaged data. In many instances

CT images disease patterns of more than 7 classes are present and an ANN can be employed to classify as many 10 types of disease patterns.

Since blinded image data was not available, the assessment of the classification accuracy was performed through leave-one-out and 5-fold cross validation techniques. However, 5-fold cross validation techniques shows results based on a fair comparison. These techniques together contribute to the minimization of methodological bias. Leave-one-out method has marginally higher classification accuracy, but 5-fold method is a better verification technique. This result is expected because every time ANN is trained, it will create the relationships and learning patterns based on fewer number of ROI's and therefore less number of features. Also, testing based on 5F model generated based on this learning process is more rigid compared to leave-one-out, which results in a lower accuracy. However, the descriptiveness of each feature and their combination is still useful, because the accuracy increases when new features are added. Classification accuracy for any combination of classes up to seven classes is higher than 91%, and for eleven classes it is 85% (figure 6.4). The accuracy for up to three classes is 99% which demonstrates a very accurate quantification. These methods and quantifications contributes to computerised analysis of DLD and can be used towards generating a second opinion to a radiologist's assessment.

In Figure 7.1, L1 refers to leave-one-out and 5F refers to 5-fold cross validation methods. Classification results of 2, 3, 4, 7 and 11 classes are listed for both types of validations based on ANN for ten DLD patterns and healthy lung regions extracted from CT images by an expert chest radiologist.

Table 7.1 demonstrates the total number of features for each texture and fractal method described in chapter 3 and 4 along with SIFT features from chapter 5. A total of 48 and 29 features are extracted based on all texture and fractal methods, respectively.

All these 77 features along with the number of features extracted based on SIFT are the inputs of an ANN. These features are extracted from ROI's that were chosen based on DLD patterns from CT images of the lung as described in earlier chapters.

Nature of features	Feature Method	Number of Features	
Texture Analysis	Tamura	3	48
	CLBP	13	
	GLCM	13	
	Haralick	13	
	Gabor	3	
	MF	3	
Fractal Analysis	Box-counting	3	29
	SFTA	24	
	Semi-variance	2	
Local Extrema	Number of features depends on the ROI	Descriptor for each feature is a vector of size 128	

Table 7.1 Number of features for each texture, fractal and SIFT method are represented



Figure 7.1. Comparison of Classification Accuracy of All Texture, Fractal and SIFT features Based on 5-Fold Cross validation and leave-One-Out Methods on ANN

Classification accuracy of ten DLD patterns were provided based on 5-fold cross (5F) validation on ANN and the results were compared with leave-one-out (L1) method. Classification accuracy increases in both methods when smaller number of classes are present for classification.

Classification accuracy of texture features are assessed based on the combination of six methods, where Haralick, Tamura and GLCM have the highest classification results, and Gabor, CLBP and MF features follow for both types of validations. Classification accuracy of texture features drops from 98% to 90% for two classes (figure 7.1) when assessed with L1 and 5F respectively, however there was only a 3% decrease when comparing eleven classes, for all texture features combined.

Classification accuracy of SIFT features are also lower with 5F compared with L1 but the results are consistently increasing when comparing individual features and their combinations. With 5F, accuracy of eleven classes increased from 68% with SIFT features to 84% with SIFT and texture features combined; and 85% percent when fractal features were added up to the SIFT and texture feature combination (figure 7.1).

III. Contributions

This thesis has attempted to identify and employ innovative computational algorithms for identification and classification of several DLD patterns. A large number of texture algorithms and quantitative indices from fractal analysis have been invoked to obtain a broad range of features. In addition, a novel scale invariant feature transform (SIFT) has been incorporated to obtain unique features from the regions with irregular parenchymal pathologies in lung CT images, to enhance the machine learning and pattern classification.

The SIFT analysis on its own generated more than 96% accuracy when classifying up to four classes and 68% for up to eleven classes with 5-fold cross validation technique (figure 7.1). A combination of texture and fractal methods combined with SIFT provided increased classification accuracies when analysing CT images of the lung. More than 98.8% accuracy for up to four classes and 85% accuracy in classifying eleven classes, including healthy ROI's, was achieved.

Many textural, fractal and scale invariant based features that can characterise DLD patterns with non-overlapping information, have been assembled in this thesis work. This combination takes several characteristics such as texture, morphology, scale, position and frequency domain features into account.

Although in real life applications, to use a computer aided diagnostic system as a potential second opinion, one must be able to classify several patterns. None of the research in the state-of-the-art have provided detailed classification for up to eleven classes. The analysis provided in earlier chapters combined with two validation methods used to assess the strength and stability of the extracted features justify claims presented in this thesis.

IV. Future Work

Image processing and especially medical image quantification has been the focus of many researchers, therefore, more algorithms are on its way to target these problems. Based on the methods described in this thesis and results that were achieved, below is a list of ideas for future research.

1. Features described in this thesis can be researched and applied to identify diseases of other organs such as kidney, liver and brain from various image modalities

2. The classification can be analysed using SVM and K-nearest neighbour methods
3. Identifying the location and the nature of the disease is very important in classification. This can be used as extra features for quantifying the ROI's.
4. Adding the capability to trace a potential disease through cross sectional images to differentiate it with other organs. Sometimes if one looks at a single cross sectional image of the lung, it is difficult to separate nodularity with a blood vessel; but a blood vessel can be traced through images before and after the particular image.
5. Ideally blinded image data can be examined with the classifiers and features designed in this thesis
6. Analysing and identifying the shape and position of a disease in frequency domain by quantifying the and researching the changes on signals is very interesting
7. New scanners incorporates CT and MR imaging in one machine. Quantifying images based on the outcome of these scanners or even researching the raw data acquired from them to see if features can be extracted from that level of information is something no researcher has done before.
8. Radiologists zoom in and zoom out, and also track organs through different slices of cross sectional images, to find a disease. Possibly, segmentation of the whole long and identification of every organ will provide information about pathology and their location. Based on that and a gold standard model of the body, finding irregularities can be made easier.
9. Identifying cancer in an early stage is crucial. Radiologists take several scans over a period of time (3 times in 6 months) and compare the cancerous region to see if it

is getting bigger or metathesizing. Therefore, localizing the cancerous region and analysing the area by comparing it with subsequent scans can be an interesting application

10. One could write software on a web-based or mobile/tablet platform that takes all the images of a patient and identify locations with possible abnormalities. The results should be a decision making approach with appropriate probabilities of a disease. Bayesian approach may contribute to better decision making.
11. The computer aided diagnostic system can be installed on the machine which is scanning the patient, and run the analysis in real time.
12. Parallel processing can be used to speed up the classification and quantification

APPENDIX I: DIFFUSE LUNG DISEASES

Diffuse lung diseases (DLD) constitute a variety of acute and chronic interstitial pneumonias. These are diseases of the intralobular and interlobular interstitium. As a consequence there is airspace involvement and often secondary involvement of the peripheral airways. Many DLDs are rare entities if considered separately, although they account for one third of overall morbidity.

Below is a representation and brief description of: consolidation, cyst, emphysema, fibrosis, ground glass opacity, honey combing, nodularity, reticulation, scar and tree-in-bud.

Consolidation (Figure 1) is recognised by the radiological pattern of air-space opacification. The alveolar spaces may be opacified by fluid (heart failure), infective inflammatory exudate (pneumonia), blood (pulmonary haemorrhage) and cells (lung cancer). Presentation is dependent on the underlying cause. Depending on aetiology, symptoms may include shortness of breath, productive cough, haemoptosis, fevers/chills/rigors and weight loss, particularly in malignancy. This high attenuation pattern obscures underlying interstitial structure and compromises visual assessment of the interstitium.



Figure 1. CT Image of the lung identified with consolidation

Pulmonary cysts (Figure 2) are cystic spaces within the lung parenchyma that have a wall thickness that measures between 1 and 4 mm. The visual assessment of this pattern is analyzed by low attenuation with a well-defined with a measurable wall thickness.

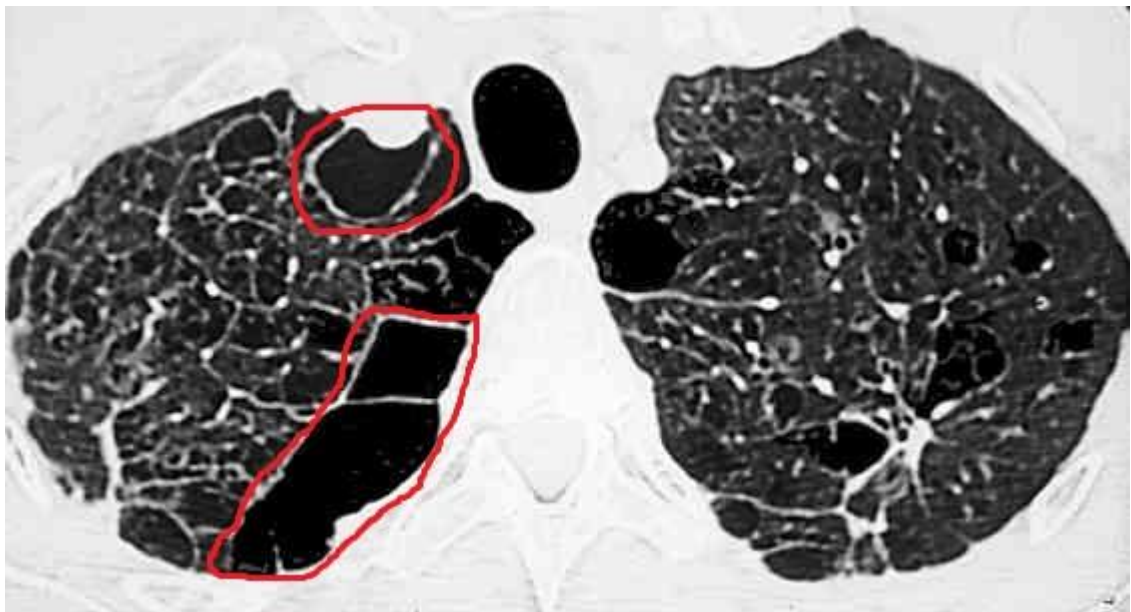


Figure 2. CT image of the lung identified with pulmonary cyst

Pulmonary emphysema (Figure 3) is defined as the "abnormal permanent enlargement of the airspaces distal to the terminal bronchioles accompanied by destruction of the alveolar wall and without obvious fibrosis". Chronic obstructive pulmonary disease (COPD) is a combination of emphysema and chronic bronchitis. This low attenuation pattern in emphysema does not have a vivid boundary or wall thickness like cyst.

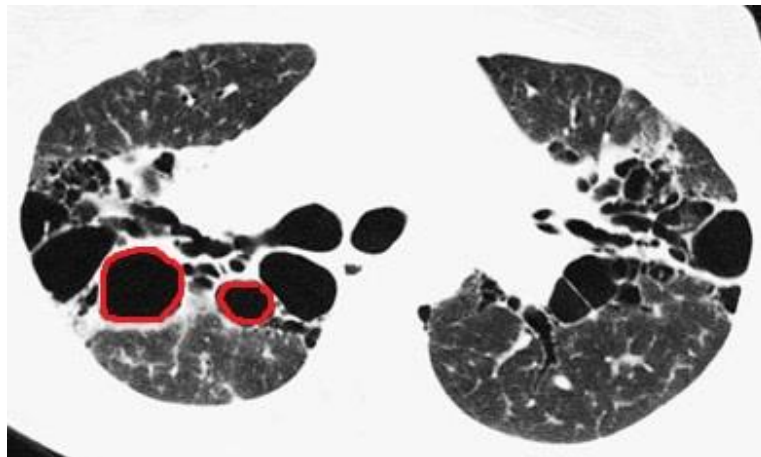


Figure 3. CT image of the lung identified with pulmonary emphysema

Pulmonary fibrosis (Figure 4) is a "descriptive" term given when there is excess of scar tissue in the lung. It can be precipitated by protean causes. Pulmonary fibrosis can be localised, affect a segment, lobe or the entire lungs. Fibrosis in the lung is a process that occurs in the interstitium. It is therefore also termed interstitial fibrosis.

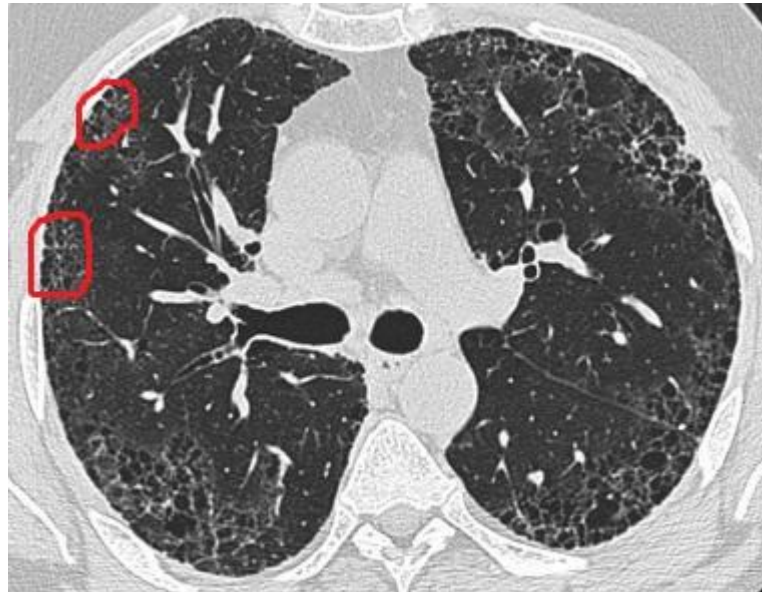


Figure 4. CT image of the lung identified with pulmonary fibrosis

Ground-glass opacification/opacity (GGO), Figure 5, refers to a hazy area of increased attenuation in the lung with preserved bronchial, and vascular visualization. It is a non-specific sign with a wide aetiology including infection, chronic interstitial disease and acute alveolar disease.

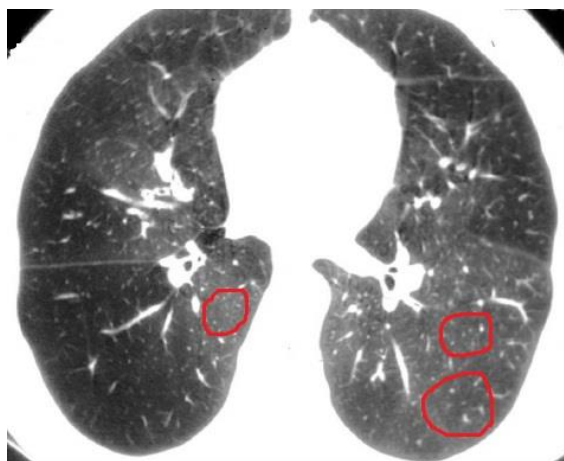


Figure 5. CT image of the lung identified with GGO

Honeycombing (Figure 6) is a feature of advanced pulmonary fibrosis, also referred as usual interstitial pneumonia. CT images demonstrates clustered or layered cystic air spaces between 0.3-1.0 cm in diameter, which are usually sub-pleural and basal in distribution. Criteria for diagnosis vary but a common standard of triple layering is well recognised.

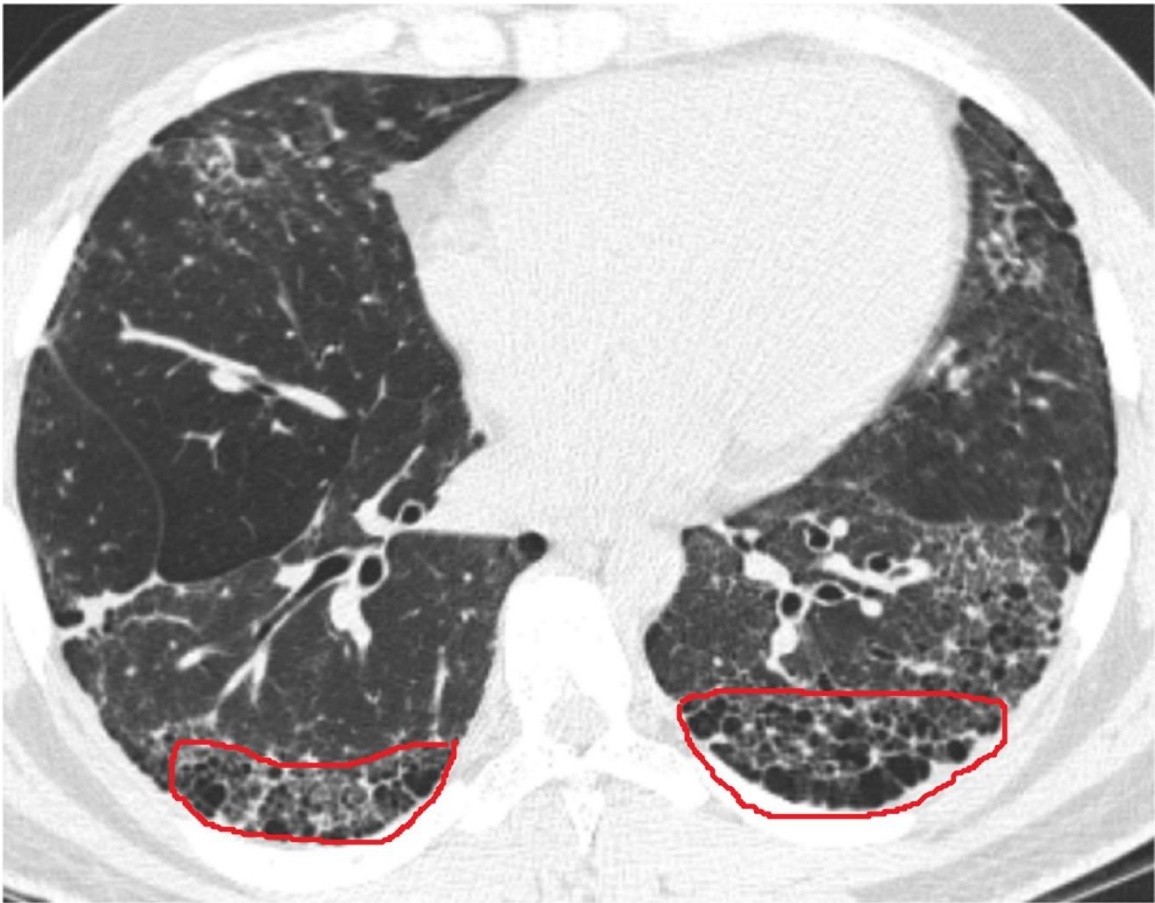


Figure 6. CT image of the lung identified with honeycombing

A Pulmonary nodule (Figure 7) is a lung parenchymal abnormality measuring between 1-30mm in size surrounded by normal or abnormal lung parenchyma. Single or multiple, these can signify disease processes affecting either the interstitium or the airspace. They

can arise from a vast number of pathological entities. Nodules can be centrilobular, random or perilymphatic depending on their position in the pulmonary lobule.



Figure 7. CT image of the lung identified with pulmonary nodule

Reticulation (Figure 8) is the thickening of any of the interstitial compartments by blood, water, tumour, cells, fibrous disease or any combination thereof. The thickening of the interstitium can be reticular, reticulonodular, or linear where the predominant pattern is a result of the underlying pathological process.

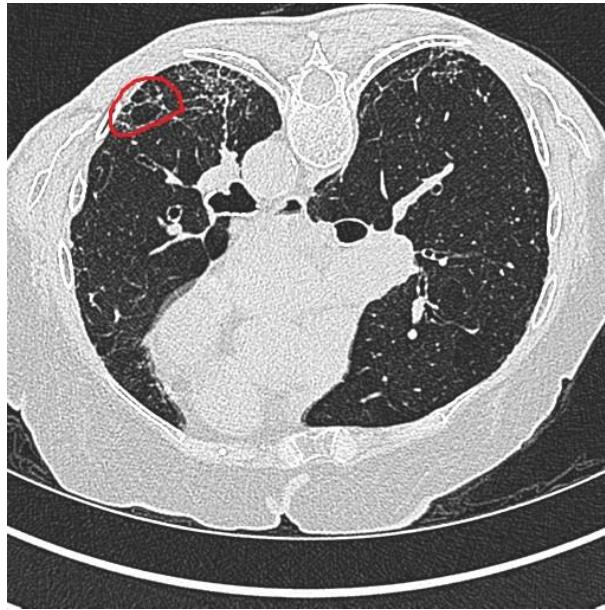


Figure 8. CT image of the lung identified with reticulation

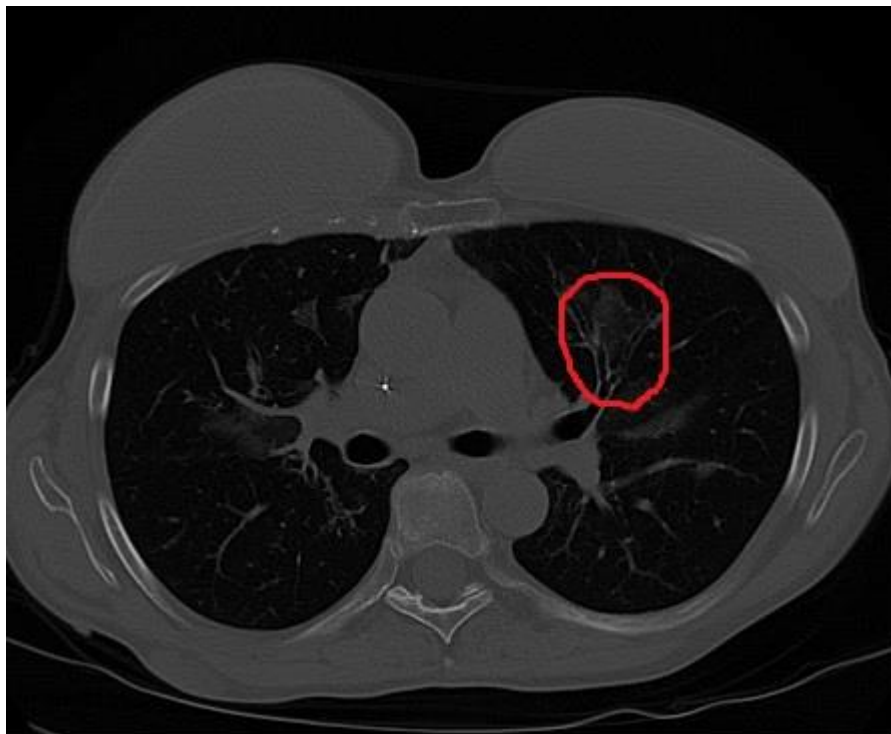


Figure 9. CT image of the lung identified with scar

Tree-in-bud (Figure 10) is a pattern that demonstrates multiple areas of centrilobular nodules with a linear branching pattern. It usually indicates spread of air way infection.

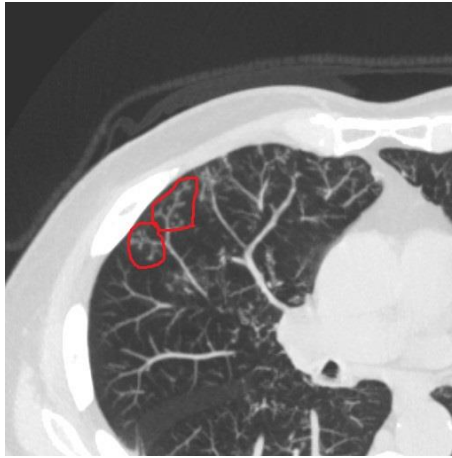


Figure 10. CT image of the lung identified with tree-in-bud

APPENDIX II: MINKOWSKI FUNCTIONALS

Consider region R_i in an excursion set $P\{\mathit{supf}(t)_{t \in T} \geq u\}$ with $v(\theta, \varphi) \equiv \frac{\Delta T(\theta, \varphi)}{\sigma_0} > v_t$,

where $\sigma_0 = \left(\left(\frac{\Delta T}{T}\right)^2\right)^{\frac{1}{2}}$, $v(\theta, \varphi)$ is the number of maxima and v_t is the threshold¹²⁴.

Complex regions require more parameters to be characterized. Three partial Minkowski Functionals (MF) are: the area of the region (a_i), counter length (l_i) and the number of holes (n_{hi}). Number of holes are the Euler characteristic or the number of disjoint boundaries. The sum of these three quantities on all disjoint regions of excursion set results in MF analysis.

MF are special geometric quantities because they are translation and rotation invariant with intuitive measurements. Also, global morphological properties such as motion invariance and additivity of any d dimensional patterns can be charectrized with $d + 1$ MF.

Global MF of Gaussian field in 2D are¹²⁴:

$$A(v) = \frac{1}{2} - \frac{1}{2} \Phi\left(\frac{v}{\sqrt{2}}\right)$$

$$L(v) = \frac{1}{8\theta_c} v e^{\frac{v^2}{2}}$$

$$G(v) = \frac{1}{(2\pi)^{\frac{3}{2}}} \left(\frac{1}{2\pi_c^2}\right) v e^{-\frac{v^2}{2}}$$

where $\Phi(x) = \frac{2}{\sqrt{\pi}} \int_0^x e^{-x'^2} dx'$ is the error function. Sprectrum dependency is evaluated

based on the length scale of the field $\theta_c = \frac{\sigma_0}{\sigma_1}$ where

$$\sigma_0 = \frac{1}{4\pi} \sum_l (2l + 1) C_l,$$

$$\sigma_1 = \frac{1}{4\pi} \sum_l (2l + 1)(l + 1) l C_l.$$

All disjoint regions are identified by a threshold. For positive peaks threshold is $v > v_t$

and for negative peaks the threshold is $v < -v_t$. For every region R_i MF are:

$$\mathbf{a}_i = v_1^i, l_i = v_2^i, n_{hi} = v_3^i.$$

To compute partial MF following convergence properties should be satisfied¹²⁴:

$$v_{kp}^i - v_k^i \rightarrow \mathbf{0} \text{ as } h \rightarrow \mathbf{0}$$

$$\frac{v_{kp}^i - v_k^i}{v_k^i} \approx \mathbf{O}(h^2), k = 1, 2$$

Where v_{kp}^i is the k th MF of i th cluster, calculated on pixel values, and v_k^i is the exact value of the function on a continuous field.

Pixel (k_1, k_2) where the maxima satisfies $v_{k_1, k_2} > v_t$ is considered to be inside the region if the pixel value is below v_t threshold at least in one of the four neighbourhoods $((k_1 + 1, k_2), (k_1 - 1, k_2), (k_1, k_2 + 1), (k_1, k_2 - 1))$. To assess the boundary curve with the grid lines, an approximation of smoothed boundary curve using a polygon with linear interpolation of inner and outer boundary pixels is used¹²⁴:

$$\theta_b = k_1 h + h \frac{v_t - v_{k_1, k_2}}{v_{k_1+1, k_2} - v_{k_1, k_2}}, \varphi_b = k_2 h$$

For φ grid line and $\theta_b = k_1 k, \varphi_b = k_2 k + h \frac{v_t - v_{k_1, k_2}}{v_{k_1, k_2+1} - v_{k_1, k_2}}$ for θ grid lines. θ_b and

φ_b denote coordinates of the boundary points $X_m = (\theta_b, \varphi_b)$ on polygon which

converges to smooth boundary lines as $h \rightarrow \mathbf{0}$.

APPENDIX III: MOST POPULAR CLASSIFIERS IN MEDICAL IMAGING

There are several classification techniques such as ANN, SVM and K-nearest that were used in the state of the art to report classification accuracies based on features that were extracted from pathological patterns on the lung. This dissertation has chosen ANN for the learning purpose because features are not scaled or heterogeneous. For the same purpose SVM and K-nearest could not be useful for classification accuracy assessment because they are depend on distance functions (homogeneity of data). The structure and fundamentals of these three classifiers are provided below.

A. Artificial Neural Networks

Historically artificial neural networks (ANN) are responsible for the revival in machine learning. Research into machine learning got a boost because of ANN. Furthermore, ANN algorithms were based on concepts found in nature and algorithms were easy to implement. They have achieved success in engineering, finance, robotics, medical science and several other fields. Nowadays newer machine learning models might be in favor, but still in many cases they can do the job just as good as recent procedures.

Each neuron in an ANN is characterized by an input, a computational component and an output. A typical ANN is built with these basic building blocks. The computational element of each neuron is defined by a transfer function which can be tailored to meet a specific computational task. For classification problems, a sigmoid transfer function is often used. The sigmoid transfer function between the input and output neurons is continuous and differentiable. Therefore, finding derivatives of such a function is computationally straightforward. The sigmoid transfer function is defined as¹⁴⁷

$$\sigma(x) = \frac{1}{(1 + e^{-x})}$$

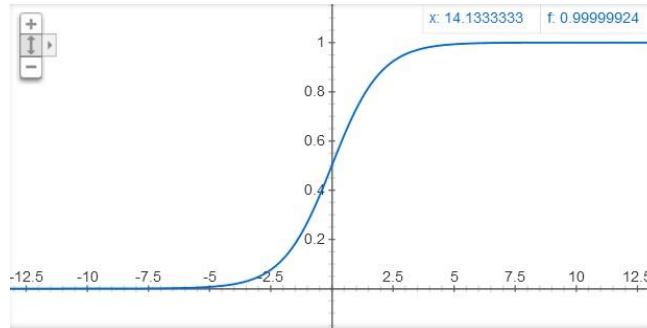


Figure 11 Sigmoid transform function

To find the derivative of this function³⁷

$$\begin{aligned} \frac{d}{dx} \sigma(x) &= \frac{d}{dx} \left(\frac{1}{(1 + e^{-x})} \right) \\ &= \frac{e^{-x}}{(1 + e^{-x})^2} = \frac{(1 + e^{-x}) - 1}{(1 + e^{-x})^2} = \frac{1 + e^{-x}}{(1 + e^{-x})^2} - \left(\frac{1}{1 + e^{-x}} \right)^2 \\ &= \sigma(x) - \sigma(x)^2 \Rightarrow \sigma' = \sigma(1 - \sigma) \end{aligned}$$

A neuron would be represented as follows³⁷

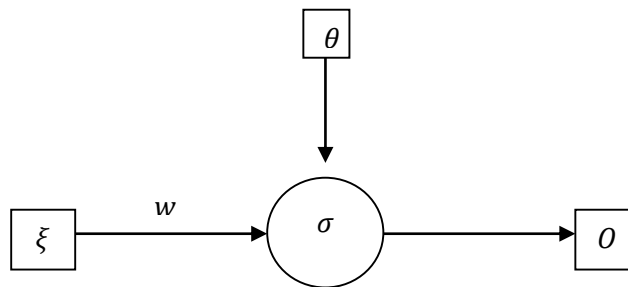


Figure 12 An example of a neuron

Where ξ is the input data, w is the weight, σ is the transfer function that we will use for this neuron and O is the output for this NN. A threshold is always associated with neurons which is denoted by θ . The threshold will allow a neuron to fire, if the result of the input

and its weight exceeds the threshold. To define the output of this function one can use this

$$O = \sigma(\xi w + \theta)$$

and if the number of inputs are more (n) the equation would be³⁷

$$O = \sigma(\xi_1 w_1 + \xi_2 w_2 + \xi_3 w_3 + \dots + \xi_n w_n + \theta)$$

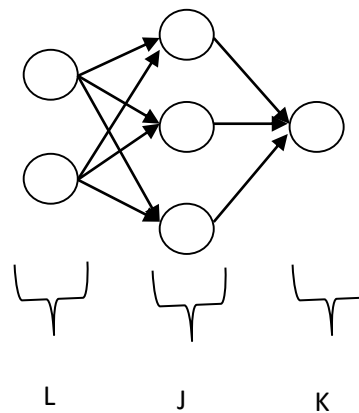


Figure 13 An example of 2x3x1 NN

The representation of a neural network is shown above. The first two neurons are the input layer (L), there neurons in the middle are the hidden layer (J) and the final neuron is the output layer (K).

The most commonly used algorithm of ANN is back-propagation technique. Having a set of training data sets t_j and outputs O_j , the error equation would be³⁷

$$E = \frac{1}{2} \sum_{k \in K} (O_k - t_k)^2$$

We calculate the rate of change of error with respect to weight w_k to minimize $\frac{\delta E}{\delta w_{jk}^l}$, and we use that to do the gradient decent on the gradient of E with respect to the weights. Then

we propagate that backwards to the network and adjust the weights. The notations below are defined for further use:

x_j^l : Input to node j of layer l

w_{ij}^l : Weight from layer $l - 1$ node i to layer l node j

θ_j^l : Bias of node j of layer l

O_j^l : Output of node j in layer l

t_j : Target value of node j of the output layer

To calculate the back-propagated value we encounter two types of weights, the connecting the output layer to the hidden layer and the one that goes from the hidden layer to the input. So we have calculated the errors based on the target values for each one³⁷:

1. If the node is an output layer node we calculate the derivative of E with respect to the weight from j to k

$$\frac{\partial E}{\partial w_{jk}} = \frac{\partial}{\partial w_{jk}^2} \frac{1}{2} \sum_{k \in K} (O_k - t_k)^2 = (O_k - t_k) \frac{\partial}{\partial w_{jk}} O_k$$

Since the weight between j and k are related to $k \in K$ we will lose the sum after taking the derivatives. Output of k is just the sigmoid function of the input of k

$$\begin{aligned} &= (O_k - t_k) \frac{\partial}{\partial w_{jk}} \sigma(x_k) = (O_k - t_k) \sigma(x_k) (1 - \sigma(x_k)) \frac{\partial}{\partial w_{jk}} x_k \\ &\Rightarrow \frac{\partial E}{\partial w_{jk}} = (O_k - t_k) O_k (1 - O_k) O_j \end{aligned}$$

If $(O_k - t_k) O_k (1 - O_k) = \delta_k$

$$\Rightarrow \frac{\partial E}{\partial W_{jk}} = \delta_k O_j$$

If the node is a hidden layer node, we calculate the derivative of E with respect to the weight from i to j

$$\begin{aligned} \frac{\partial E}{\partial W_{ij}} &= \frac{\partial}{\partial W_{ij}^2} \frac{1}{2} \sum_{k \in K} (O_k - t_k)^2 = \sum_{k \in K} (O_k - t_k) \frac{\partial}{\partial W_{ij}} O_k \\ &= \sum_{k \in K} (O_k - t_k) \frac{\partial}{\partial W_{ij}} \sigma(x_k) \\ &= \sum_{k \in K} (O_k - t_k) \sigma(x_k) (1 - \sigma(x_k)) \frac{\partial x_k}{\partial W_{ij}} \\ &= \sum_{k \in K} (O_k - t_k) O_k (1 - O_k) \frac{\partial x_k}{\partial O_j} \cdot \frac{\partial O_j}{\partial W_{ij}} = \sum_{k \in K} (O_k - t_k) O_k (1 - O_k) W_{jk} \cdot \frac{\partial O_j}{\partial W_{ij}} \\ &= \frac{\partial O_j}{\partial W_{ij}} \sum_{k \in K} (O_k - t_k) O_k (1 - O_k) W_{jk} = \frac{\partial O_j}{\partial W_{ij}} \sum_{k \in K} \delta_k W_{jk} \\ &= O_j (1 - O_j) \frac{\partial x_j}{\partial W_{ij}} \sum_{k \in K} \delta_k W_{jk} \\ &\Rightarrow \frac{\partial E}{\partial W_{ij}} = O_i O_j (1 - O_j) \sum_{k \in K} \delta_k W_{jk} \end{aligned}$$

If $\delta_j = O_j (1 - O_j) \sum_{k \in K} \delta_k W_{jk}$ then

$$\Rightarrow \frac{\partial E}{\partial W_{ij}} = \delta_j O_i$$

From the bias term we know $\frac{\partial O}{\partial \theta} = 1$ and $\frac{\partial E}{\partial \theta} = \delta_i$.

The back-propagation algorithm works as follows:

1. Run the network and generate the outputs
2. for every output node calculate δ_k
3. for every hidden layer node calculate δ_j
4. Then update the weights and biases based on the changes as follows:

$$\Delta W = -\eta \delta_l O_{l-1}$$

$$\Delta \theta = -\eta \delta_l$$

Now apply the changes

$$W + \Delta W \rightarrow W$$

$$\theta + \Delta \theta \rightarrow \theta$$

By continuing this procedure for the rest of our data set, the NN will be trained and proper weights would be assigned to connection from the input to output. Based on the final set of weights, classification can begin.

B. Support Vector Machine

Support vector machines (SVM)¹⁴⁸ are used for classifying a set of data in feature space. Suppose we have two features x_1 and x_2 and two classes of blue squares and red circles. SVM separates these two classes by drawing a line between them. There are infinite lines that could be drawn. Therefore, SVM is an optimization problem where it finds the optimal line to maximize the straight between classes.

To find the proper hyper plane we first find three support vectors s_1, s_2 and s_3 . These are vectors that should be a combination of classes where the distances from each other are least possible choice. Each vector has a position based on the features. A bias input would

be added as the last element of a support vector, i.e. $s_1 \begin{bmatrix} x_1 \\ x_2 \end{bmatrix} \Rightarrow s'_1 = \begin{bmatrix} x_1 \\ x_2 \\ bias \end{bmatrix}$. To find the proper hyper plane we solve the following equation based on three parameters β_1, β_2 and β_3 ¹⁹:

$$\beta_1 s'_1 s_1 + \beta_2 s'_2 s_1 + \beta_3 s'_3 s_1 = -1$$

$$\beta_1 s'_1 s_2 + \beta_2 s'_2 s_2 + \beta_3 s'_3 s_2 = -1$$

$$\beta_1 s'_1 s_3 + \beta_2 s'_2 s_3 + \beta_3 s'_3 s_3 = 1$$

Each equation is equal to ± 1 depending on the supporting vector class. That is because the result of the dot product of a vector which is perpendicular to the medium (separator line) and a sample data would result in a positive value if the data is over that line. The larger the value of this product, the further the point is from the line. And if the result is negative, that means the point is behind the line¹⁹. In this example we considered red circles as -1 and blue squares as +1. The equation for finding the hype plane is:

$$w' = \sum_i \beta_i s'_i$$

Therefore, the hyper plane is $y = wx + b$, where $w = \begin{bmatrix} \alpha_1 \\ \alpha_2 \end{bmatrix}$ and b is the offset created from

the bias $w' = \begin{bmatrix} \alpha_1 \\ \alpha_2 \\ b \end{bmatrix}$.

So we need to come up with a value for the bias and a kernel or similarity function. If we decide not to use any kernel then we have linear kernel, such as the method explained above. When we have large number of features, and the number of training examples is

small, we can choose a linear kernel and a bias value of one. In this way we avoid the complexity of a kernel function by over fitting the prediction¹⁹.

But if we decide to have kernel function (non-linear), then a Gaussian function can be useful:

$$f = \exp\left(-\frac{\|x_1 - x_2\|^2}{2\sigma^2}\right).$$

This choice is made when the number of features is small and we have a large data set. Feature scaling is an important pre-analysis method when using Gaussian kernels. This is because, when finding the norm $\|x_1 - x_2\|^2$ (magnitude of x), since features are different, one feature might result in a big value and therefore, its norm value could dominate other results. So by scaling, we make sure other features play their role as they should.

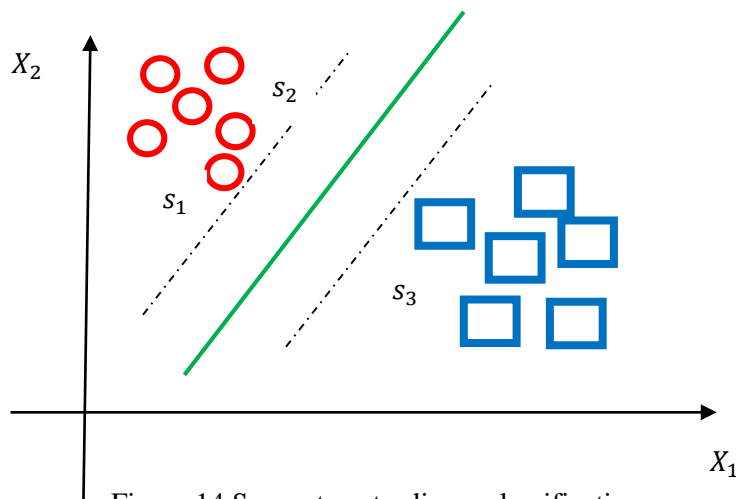


Figure 14 Support vector linear classification

C. K-Nearest Neighbor

Suppose we have a data set x_i as vector d and $x \in R^d$ and two classes $y_i \in \{0,1\}$. We want to use KNN to find the corresponding class of a new data x . The main idea of this algorithm is to take x and classify it based on the majority vote of K nearest points in the training data.

Suppose we have two classes of data, green circles and red triangles. A new data point is among them which is shown as Blue Square. We do not know the class it belongs.

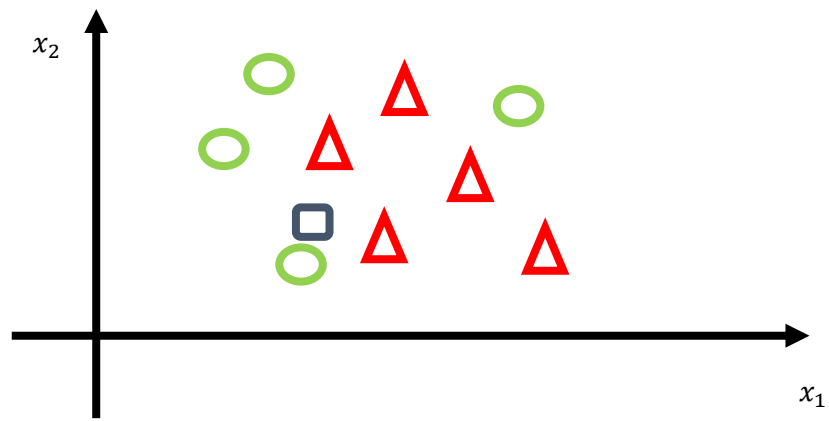


Figure 15 K-Nearest neighbour classifier

Starting with $k = 1$, the Euclidean distance between x_i and x_j which are two different data points is

$$(x_i, x_j)^2 = \|x_i - x_j\|^2 = \sum_{k=1}^d (x_{ik} - x_{jk})^2$$

and we look for only one data which closer to our new data point as if we include other data points in a circle where the square is the center. In this case the square belongs to the

circle class since it is closer to it. But if we increase the number of K neighbors, our decision might change. For $K = 3$, there is one circle and two triangles close to the square data point, so the proper class should be a red triangle. So deciding on the number of neighbors is an important factor in this type of classification that could be overcome by cross-validation.

To find the proper class based on the number of neighbors close to it, a simple probabilistic problem could be solved by calculating the fraction of points x_i in K nearest points of x such that $y_i = y$ and

$$\hat{y} = P(y|x, D)$$

where \hat{y} is the probabilistic of a class and D is the data set (x_i, y_j) .

REFERENCES

1. Al-Kadi OS, Watson D. Texture analysis of aggressive and nonaggressive lung tumor CE CT images. *IEEE TBME*. 2008 Jul;55(7):1822-1830.
2. Shi, J., Malik, J. Normalized cuts and image segmentation. *IEEE CVPR*. 2002 Aug 06;22(8):888-905.
3. Boser B. E. Guyon I. M. Vapnik, V. N. A training algorithm for optimal margin classifiers. *Annual Workshop on Computational Learning Theory (COLT)*. 1992 Jul 1:144-152.
4. Youxin M. Medical Imaging. In Chapter: Nailon W.H. *Texture Analysis Methods for Medical Image Characterisation*. Publisher InTech; 2010. p. 75-96.
5. Tuceryan M and Jain A.K. *Handbook of Pattern Recognition and Computer Vision*. Chapter on Texture Analysis. 2nd ed. World Scientific Publishing, Singapore; 1998. p. 207-248,
6. Zavaletta VA, Bartholmai BJ, Robb RA. High resolution multidetector CT-aided tissue analysis and quantification of lung fibrosis. *Acad Radiol*. 2007 Jul;14(7):772-87.
7. Roumi M. *Implementing Texture Feature Extraction Algorithms on FPGA [Master's dissertation]*. Delft University of Technology; 2009.
8. Xu Y, Sonka M, McLennan G, Guo J, Hoffman E. MDCT-based 3-D texture classification of emphysema and early smoking related lung pathologies. *IEEE Trans Med Imaging*. 2006 Apr;25(4):464-475.

9. Vasconcelos V, Silva JS, Marques L, Barroso J. Statistical textural features for classification of lung emphysema in CT images: A comparative study. Information systems and technologies (CISTI) Iberian conference; Santiago de Compostela, 2010 Jun 16;5:1-5.
10. Korfiatis PD, Karahaliou AN, Kazantzi AD, Kalogeropoulou C, Costaridou LI. Texture-Based Identification and Characterization of Interstitial Pneumonia Patterns in Lung Multidetector CT. IEEE trans inf technol biomed. 2010 May;14(3):675-80.
11. Mariolis I, Korfiatis P, Costaridou L, Kalogeropoulou C, Daoussis D, Petsas T. Investigation of 3D textural features discriminating ability in diffuse lung disease quantification in MDCT. 2010: IEEE International Conference; 2010 July 1-2; IEEE; 2010. p 135-138.
12. Chen CC, Daponte JS, Fox MD. Fractal feature analysis and classification in medical imaging. IEEE tran med imaging. 1989;8: p.133-142.
13. Caban JJ, Rheingans P. Texture-based transfer functions for direct volume rendering. IEEE Transactions on Visualization and Computer Graphics. 2008;14(6):1364-1371.
14. Yao J, Dwyer A, Summers RM, Mollura DJ. Computer-aided diagnosis of pulmonary infections using texture analysis and support vector machine classification. Acad Radiol. 2011 Mar;18(3):306-314.
15. Song Q, Sonka M, Hoffman EA, Reinhardt JM. Segmentation of pathological and diseased lung tissue in CT images using a graph-search algorithm. IEEE International Symposium on Biomedical Imaging: From Nano to Macro. 2011;2072-2075.
16. Oh S. and Choe Y. Texture Segmentation in 2D vs. 3D: Did 3D Developmentally Precede 2D? Proceedings of the Third International Conference on Development and

Learning, Developing Social Brains, UCSD Institute for Neural Computation, San Diego; 2004; p. 175-182.

17. Wei Q, Hu Y. A study on using texture analysis methods for identifying lobar fissure regions in isotropic CT images. Annual International Conference of the IEEE Engineering in Medicine and Biology Society; 2009 Sep, Minneapolis, MN: IEEE; 2009. p. 3537-6540.

18. Korfiatis P, Kazantzi A, Kalogeropoulou C, Petsas T, Costaridou L. Optimizing lung volume segmentation by texture classification. 10th IEEE International Conference on Information Technology and Applications in Biomedicine; 2010 Nov 3-10, Corfu; IEEE. p. 1-4.

19. Cristianini N., Shawe-Taylor J. An Introduction to Support Vector Machines and Other Kernel-Based Learning Methods. Cambridge University, Cambridge, UK. 1st ed, 2000.

20. Singh, P.K., Compton, P. Texture based region annotation in HRCT lung images. IEEE Proceedings of the Eighth International Symposium on Signal Processing and its Applications, Sydney, Australia. 2005 August 28-31;1: p. 219 – 222.

21. Helen R, Kamaraj N, Selvi K, Raja Raman V. Segmentation of pulmonary parenchyma in CT lung images based on 2D Otsu optimized by PSO. IEEE Emerging Trends in Electrical and Computer Technology (ICETECT), Tamil Nadu. 2011 Mar 23-24; Tamil Nadu: p. 536 – 541.

22. Liming D, Caiming Z, Shanshan G. A new algorithm of automatic lung parenchyma segmentation based on CT images. International Conference on Consumer Electronics, Communications and Networks (CECNet). 2011 Apr 16-18; XianNing: p. 976 – 979.

23. Jiantao Pu, C. Fuhrman, W.F. Good, F.C. Scirba, D. Gur. A Differential Geometric Approach to Automated Segmentation of Human Airway Tree. *IEEE Transactions on Medical Imaging*. 2010 Sep 16;30(2): p. 266 – 278.
24. Haibo W, Jing Z, Liwei W. Segmentation of thoracic CT image based on FCM clustering. *Advanced Computer Theory and Engineering (ICACTE)*, 2010 3rd International Conference. 2010 Aug 20-22;3; Chengdu; p. V3-405 - V3-408.
25. Babin D, Vansteenkiste E, Pizurica A, Philips W. Segmentation of airways in lungs using projections in 3-D CT angiography images. *Annual International Conference of the IEEE Engineering in Medicine and Biology Society (EMBC)*. 2010 Aug 31-Sep 4; Buenos Aires; p. 3162-3165.
26. Farag A, Graham J, Farag A. Robust segmentation of lung tissue in chest CT scanning. *17th IEEE International Conference on Image Processing (ICIP)*. 2010 Sep 26-29; Hong Kong; p. 2249-2252.
27. Wang Z, Meng X, Zhao Y, Xue H, Li Q, Li J, et al. Lung Lobe Segmentation Based on HRCT Data. *International Conference on Biomedical Engineering and Computer Science (ICBECS)*. 2010 Apr 23-25; Wuhan; p. 1-4.
28. Kockelkorn TTJP, Van Rikxoort EM, Grutters JC, Van Ginneken B. Interactive lung segmentation in CT scans with severe abnormalities. *IEEE International Symposium on Biomedical Imaging: From Nano to Macro*. 2010 Apr 14-17; Rotterdam, Netherlands; p. 564-567.

29. Van Rikxoort EM, Prokop M, De Hoop B, Viergever MA, Pluim JPW, Van Ginneken B. Automatic segmentation of pulmonary lobes robust against incomplete fissures. *IEEE Transactions on Medical Imaging*. 2010 Mar 18;29(6): p. 1286-1296.
30. Zhu C, Qi S, van Triest H, Wang S, Kang Y, Yue Y. Automatic 3D segmentation of human airway tree in CT image. *IEEE 3rd International Conference, Biomedical Engineering and Informatics (BMEI), Yantai*. 2010 oct 16-18;1; Yantai: p 132-136.
31. Plajer IC, Richter D. A new approach to model based active contours in lung tumor segmentation in 3D CT image data. *2010 10th IEEE International Conference on Information Technology and Applications in Biomedicine (ITAB), Corfu*. 2010 Nov 3-5; Corfu: p. 1-4.
32. Yan-hua R, Xi-wen S, Sheng-dong N. A 3D Segmentation Method of Lung Parenchyma Based on CT Image Sequences. *IEEE International Conference on Information Networking and Automation (ICINA), Kunming*. 2010 Oct 18-19;2; Kunming: p. V2-332 - V2-336.
33. Korfiatis PD, Kalogeropoulou C, Karahaliou AN, Kazantzi AD, Costaridou LI. Vessel tree segmentation in presence of interstitial lung disease in MDCT. *IEEE Transactions on Information Technology in Biomedicine*. 2011 Feb 10;15(2):214-220.
34. Yu PY, Zhang GP, Yan JW, Liu MS. The application of the watershed algorithm based on line-encoded in lung CT image segmentation. *3rd International Workshop on Intelligent Systems and Applications (ISA)*. 2011 May 28-29; Wuhan: p. 1-4.
35. Ceylan M, Ozbay Y, Yildirim E. A new approach for biomedical image segmentation: Combined complex-valued artificial neural network case study: Lung segmentation on

- chest CT images. IEEE 5th International Biomedical Engineering Conference (CIBEC), Cairo. 2010 Dec 16-18; Cairo: p. 33-36.
36. Qaiser N, Hussain M, Iqbal N, Hussain A. Dissimilarity Analysis of Signal Processing Methods for Texture Classification. 9th International Multi-topic Conference, IEEE INMIC. 2005 Dec 24-25; Karachi: p. 1-6.
37. Rojas R. Neural networks: a systematic introduction. Springer Science & Business Media; 1996 Jul 12.
38. Park M, Jin JS, Wilson LS. A new texture analysis method for classification of interstitial lung abnormalities in chest radiography. IEEE 7th International Conference on Control, Automation, Robotics and Vision (ICARCV), Singapore. 2002 Dec 2-5;3:p. 1636-1640.
39. van Ginneken B, Katsuragawa S, ter Haar Romeny BM, Doi K, Viergever M a. Automatic detection of abnormalities in chest radiographs using local texture analysis. IEEE Transactions on Medical Imaging. 2002 Feb;21(2):p. 139-149.
40. Tang XTX, Tao DTD, Antonio GE. Texture classification of SARS infected region in radiographic image. International Conference on Image Processing. 2004 Oct 24-27;5:p. 2941-2944.
41. Tolouee A., Abrishami-Moghaddam H, Garnavi R, Forouzanfar M, Giti M. Texture Analysis in Lung HRCT Images. IEEE Digital Image Computing: Techniques and Applications (DICTA), Canberra, ACT. 2008 Dec 1-3;Canberra, ACT:p. 305-311.

42. Costa AF, Humpire-Mamani G, Traina AJM. An Efficient Algorithm for Fractal Analysis of Textures. IEEE Graphics, Patterns and Images 25th SIBGRAPI Conference, Ouro Preto. 2012 Aug 22-25; Ouro Preto:p. 39-46.
43. Xu CXC, Tian-ge ZTZ, Yan-qing HYH. Discrimination of ground glass opacity on lung HRCT images using visual complexity measurements. IEEE Proceedings of the Second Joint 24th Annual Conference of Engineering in Medicine and Biology Society, Huston, Tx. 2002;2:p. 1116-1117.
44. Huang P., Lin P., Lee CH., Kuo, C.H. A classification system of lung nodules in CT images based on fractional Brownian motion model. IEEE International Conference on System Science and Engineering (ICSSE), Budapest. 2013 Jul 4-6; Budapest:p. 37-40.
45. Kido S, Kuriyama K, Higashiyama M, Kasugai T, and Kuroda C. Fractal analysis of internal and peripheral textures of small peripheral bronchogenic carcinomas in thin-section computed tomography: Comparison of bronchiole alveolar cell carcinomas with nonbronchioloalveolar cell carcinomas. PubMed, comput Assist tomogr. 2003 Jan;27:p. 56–61.
46. Kido S, Kuriyama K, Higashiyama M, Kasugai T, Kuroda C. Fractal analysis of small peripheral pulmonary nodules in thin-section CT- Evaluation of the lung–nodule interfaces. J Comput Assist Tomogr.2002;26:p. 573–578.
47. Malone J, Rossiter JM, Prabhu S, Goddard P. Identification of disease in CT of the lung using texture-based image analysis. IEEE Record of Thirty-Eighth Asilomar Conference, PACIFIC GROVE, CALIFORNIA. 2004 Nov 7-10;2:p. 1620-1624.

48. Tong T, Huang Y, Wang X, Feng H, Li C. Automatic extraction of three dimensional lung texture tree from HRCT images. IEEE International Conference Bioinformatics and Biomedical Technology (ICBBT), Chengdu. 2010 Apr 16-18;p.198-202.
49. Wong JSJ. Automatic Honeycombing Detection Using Texture and Structure Analysis. Computational Intelligence Methods and Applications. ICSC Congress, Istanbul; 2005:p.1-4.
50. Shyu C-R, Brodley CE, Kak AC, Kosaka A, Aisen AM, Broderick LS. ASSERT: A Physician-in-the-Loop Content-Based Retrieval System for HRCT Image Databases. Computer Vision and Image Understanding. 1999 Jul 1-2;75(1-2):p. 111-132.
51. Uppaluri R, Hoffman EA, Sonka M, Hartley PG, Hunninghake GW, McLennan G. Computer recognition of regional lung disease patterns. American Journal of Respiratory and Critical Care Medicine. 1999;160(2):p. 648-654.
52. H.J. Kim, D.P. Tashkin, P. Clements, G. Li, M.S. Brown, R. Elashoff, D.W. Gjertson, F. Abtin, D.A. Lynch, D.C. Strollo, J.G. Goldin. A computer-aided diagnosis system for quantitative scoring of extent of lung fibrosis in scleroderma patients. Clin Exp Rheumatol; 2010 Nov 3;28(5 Suppl 62);p.26-35.
53. Sørensen L, Shaker SB, De Bruijne M. Quantitative analysis of pulmonary emphysema using local binary patterns. IEEE Transactions on Medical Imaging. 2010 Feb;29(2):p. 559-569.
54. Sluimer IC, Prokop M, Hartmann I, van Ginneken B. Automated classification of hyperlucency, fibrosis, ground glass, solid, and focal lesions in high-resolution CT of the lung. PubMed, Med Phys, 2006 Jul;33(7);p.2610-20

55. Boehm HF, Fink C, Attenberger U, Becker C, Behr J, Reiser M. Automated classification of normal and pathologic pulmonary tissue by topological texture features extracted from multi-detector CT in 3D. *Eur Radiol.* 2008 Dec;18(12):p.2745-55.
56. Patil SA, Udipi VR, Kane CD, Wasif AI, Desai J V., Jadhav AN. Geometrical and texture features estimation of lung cancer and TB images using chest X-ray database. *Biomedical and Pharmaceutical Engineering. ICBPE International Conference; 2009 Dec 2-4; Singapore:p. 1-7.*
57. Anand S.K.V. Segmentation coupled Textural Feature Classification for Lung Tumor Prediction. *International Conference on Communication Control and Computing Technologies (ICCCCT); IEEE. 2010 Oct 7-9; Ramanathapuram, India: p. 518-524.*
58. Sato Y, Nakajima S, Shiraga N, Atsumi H, Yoshida S, Koller T, Gerig G and Kikinis R. Three-dimensional multi-scale line filter for segmentation and visualization of curvilinear structures in medical images. *Med Image Analysis.* 1998 Jun;2(2):p.143-68.
59. Yu Y, Zhao H. A Texture-based Morphologic Enhancement Filter in Two-dimensional Thoracic CT scans. *Proceedings of the 2006 IEEE International Conference on Networking, Sensing and Control.* 2006; Ft. Lauderdale, FL: p. 850-855.
60. Al-Kadi OS, Watson D. Susceptibility of texture measures to noise: An application to lung tumor CT images. *BioInformatics and BioEngineering (BIBE), 8th IEEE International Conference; 2008 Oct 8-10; Athens: p. 1-4.*
61. Huber MB, Nagarajan MB, Leinsinger G, Eibel R, Ray LA, Wismüller A. Performance of topological texture features to classify fibrotic interstitial lung disease patterns. *PUBMED Med Phys.* 2011 Apr;38(4):2035-44

62. D. G. Lowe. Object Recognition from Local Scale-Invariant Features. The Proceedings of the Seventh IEEE International Conference, Kerkyra, 1999 Sep 20-27;(2)p. 1150-1157.
63. P. Kamencay, R. Hudec, M. Benco and M. Zachariasova. Feature extraction for object recognition using PCA-KNN with application to medical image analysis. Telecommunications and Signal Processing (TSP), 36th International Conference, Rome; 2013 July 2-3;p. 830-834.
64. F. Zhang, Y. Song, W. Cai, Y. Zhou, S. Shan and D. Feng. Context curves for classification of lung nodule images. Digital Image Computing: Techniques and Applications (DICTA), International Conference, at Hobart, TAS; 2013 Nov 26-28; p.1-7.
65. F. Zhang, W. Cai, Y. Song, M. Lee, S. Shan, D. Dagan. Overlapping Node Discovery for Improving Classification of Lung Nodules. Engineering in Medicine and Biology Society (EMBC), 35th Annual International Conference of the IEEE, Osaka, Japan; 2013 July 3-7; p. 5461-5464.
66. A. Farag, A. Ali, J. Graham, A. Farag, S. Elshazly and R. Falk. Evaluation of geometric feature descriptors for detection and classification of lung nodules in low dose CT scans of the chest. Biomedical Imaging: From Nano to Macro, IEEE International Symposium, Chicago, IL; 2011 Apr 2 – Mar 30; p. 169-172.
67. N. Kato, M. Fukui, T. Isozaki. Bag-of-features approach for improvement of lung tissue classification in diffuse lung disease. Proc. SPIE 7260, Medical Imaging: Computer-Aided Diagnosis; 2009 Feb 28;(7260);p. 72600C-1 - 72600C-10

68. W. Zhao, R. Xu, Y. Hirano, R. Tachibana, S. Kido. Classification of diffuse lung diseases patterns by a sparse representation based method on HRCT images. Engineering in Medicine and Biology Society (EMBC), 35th Annual International Conference of the IEEE, Osaka; 2013 Jul 3-7; p. 5457-5460.
69. Yonghong Shi, Feihu Qi, Zhong Xue, Liya Chen, K. Ito, H. Matsuo, Dinggang Shen. Segmenting Lung Fields in Serial Chest Radiographs Using Both Population-Based and Patient-Specific Shape Statistics. Medical Imaging, IEEE Transactions on; April 2008 ;27(4):P 481 - 494
70. Kyohei Karasawa, Shoji Kido, Yasushi Hirano, Kazuki Kozuka. Determination of lung regions on chest ct images with diffuse lung diseases by use of anatomical structures and pulmonary textures. Engineering in Medicine and Biology Society (EMBC), 2015 37th Annual International Conference of the IEEE, Milan. 25-29 Aug. 2015:P 2985 – 2988.
71. K. Punithavathy, M. M. Ramya, Sumathi Poobal. Analysis of statistical texture features for automatic lung cancer detection in PET/CT images. International IEEE Conference on Robotics, Automation, Control and Embedded Systems (RACE), Chennai. 18-20 Feb. 2015: P 1-5.
72. Xiaomin Li, Yuanyuan Wang, Jinhua Yu, Ping Chen. Fetal lung segmentation using texture-based boundary enhancement and active contour models. 3rd IEEE International Conference on Biomedical Engineering and Informatics (BMEI), Yantai. 16-18 Oct. 2010; 1:P 264 - 268
73. Yrjö Häme, Elsa D. Angelini, Megha A. Parikh, Benjamin M. Smith, Eric A. Hoffman, R. Graham Barr, Andrew F. Laine. Sparse sampling and unsupervised learning

of lung texture patterns in pulmonary emphysema: MESA COPD study. IEEE 12th International Symposium on Biomedical Imaging (ISBI), New York. 16-19 April 2015:P 109 – 113.

74. Ra Gyoung Yoon, Joon Beom Seo , Namkug Kim, Hyun Joo Lee, Sang Min Lee, Young Kyung Lee, Jae Woo Song, Jin Woo Song, Dong Soon Kim. Quantitative assessment of change in regional disease patterns on serial HRCT of fibrotic interstitial pneumonia with texture-based automated quantification system. Springer Chest European Radiology. March 2013, 23(3):p 692-701

75. Jiahui Wang, Feng Li, Kunio Doi, Qiang Li . A novel scheme for detection of diffuse lung disease in MDCT by use of statistical texture features. SPIE Medical Imaging 2009, Computer-Aided Diagnosis.. February 27, 2009.

76. Rui Xu, Yasushi Hirano, Rie Tachibana, Shoji Kido. Classification of Diffuse Lung Disease Patterns on High-Resolution Computed Tomography by a Bag of Words Approach. Springer Medical Image Computing and Computer-Assisted Intervention – MICCAI 2011. Volume 6893 of the series Lecture Notes in Computer Science; p 183-190

77. Kiet T. Vo, Arcot Sowmya. Directional Multi-scale Modeling of High-Resolution Computed Tomography (HRCT) Lung Images for Diffuse Lung Disease Classification. Springer Computer Analysis of Images and Patterns
Volume 5702 of the series Lecture Notes in Computer Science pp 663-671

78. Yoshikazu Uchiyama, Shigehiko Katsuragawa, Hiroyuki Abe, Junji Shiraishi, Feng Li, Qiang Li, Chao-Tong Zhang, Kenji Suzuki, and Kunio Doi. Quantitative computerized

analysis of diffuse lung disease in high-resolution computed tomography. American Association of Physicists in Medical Physics. 16 Mar 2003;30(9):P2440-2454

79. J.C. Caicedo and E. Izquierdo. Combining Low-level Features for Improved Classification and Retrieval of Histology Images. IBAI TRANSACTIONS ON MASS-DATA ANALYSIS OF IMAGES AND SIGNALS. September 2010;2(1):P 68-82.

80. Daniel Markel, Curtis Caldwell, Hamideh Alasti, Hany Soliman, Yee Ung, Justin Lee, and Alexander Sun. Automatic Segmentation of Lung Carcinoma Using 3D Texture Features in 18-FDG PET/CT. International Journal of Molecular Imaging. Jan 2013: Article ID 980769

81. Chih-Yi Chiu, Hsin-Chih Lin, Shi-Nine Yang. Texture Retrieval with Linguistic Descriptions. Springer publications, Chapter: Advances in Multimedia Information Processing — PCM 2001. Volume 2195 of the series Lecture Notes in Computer Science pp 308-315

82. D Markel, C Caldwell, H Alasti, A Sun, H Soliman, J Lee, Y Ung, P McGhee and D Webster. Automatic Segmentation of Non-Small Cell Lung Carcinoma Using 3D Texture Features in Co-Registered FDG PET/CT Images. American Association of Physicists in Medicine. July 2011;38(6)

83. Curtis Caldwell, Daniel Markel, Alexander Sun and Hamideh Alasti. Automatic segmentation of lung cancer based on texture features of PET/CT images. The journal of nuclear medicine. May 2011;52(1794)

84. Lee, Min-Zhao. Computer-Aided Diagnosis in Radiology: Medical Image Analysis for the Scoring of Chest Radiographs in Cystic Fibrosis. University of Sydney Faculty of Engineering and Information Technologies, Master's Thesis; June 2015.
85. Muthukumar S, Vijayananth V. INVOLUNTARY DETECTION OF TUBERCULOSIS USING ACTIVE EEMERGENCE MODEL (AAM) IN CHEST RADIOGRAPHS. International Journal of Emerging Technology and Innovative Engineering. June 2015; 1(6):p24-28.
86. S. Sumaiya Banu, S. Syed Farmhand, P. Prabakaran, L. Malathi. Detection and Classification of Lung Tissue Using Block Based Intensity Features. Journal of Advanced Engineering Research. 2014;1(1):p97-101
87. Sreeja Mole S S, Aiswarya A K, Akhila L S, Akhila S. Automated Approach for Detecting Tuberculosis using Chest Radiographs. 2015 International Journal of Scientific Research in Science, Engineering and Technology (IJSRSET); 1(3):p125-129
88. Peter Howarth and Stefan R"uger. Evaluation of Texture Features for Content-Based Image Retrieval. Springer Verlag Berlin, CIVR 2004, LNCS 3115, pp. 326–334, 2004.
89. <https://www.cs.auckland.ac.nz/courses/compsci708s1c/lectures/Glect-html/topic4c708FSC.htm>
90. Gil Paulo Melendez, Macario Cordel. Texture-based detection of lung pathology in chest radiographs using local binary patterns. 2015 8th Biomedical Engineering International Conference (BMEiCON), Pattaya. 25-27 Nov. 2015;P1-5

91. David Hébert, Chesner Désir, Caroline Petitjean, Laurent Heutte, Luc Thiberville. Detection of pathological condition in distal lung images. 2012 9th IEEE International Symposium on Biomedical Imaging (ISBI), Barcelona. 2-5 May 2012;P1603-1606.
92. Zehra Amlica, H. R. Tizhoosh, Farzad Khalvati. Medical Image Classification via SVM Using LBP Features from Saliency-Based Folded Data. 2015 IEEE 14th International Conference on Machine Learning and Applications (ICMLA), Miami. 9-11 Dec. 2015;P128-132.
93. Xiabi Liu, Ling Ma, Li Song, Yanfeng Zhao, Xinming Zhao, Chunwu Zhou. Recognizing Common CT Imaging Signs of Lung Diseases Through a New Feature Selection Method Based on Fisher Criterion and Genetic Optimization. IEEE Journal of Biomedical and Health Informatics. 02 June 2014;19(2):p635-647.
94. Teresa Zulueta-Coarasa, S. Kurugol, James C. Ross, George G. Washko. Emphysema classification based on embedded probabilistic PCA. Engineering in Medicine and Biology Society (EMBC), 2013 35th Annual International Conference of the IEEE, Osaka. 3-7 July 2013;P3969 – 3972.
95. Yang Song, Weidong Cai, Yun Zhou, David Dagan Feng. Feature-Based Image Patch Approximation for Lung Tissue Classification. IEEE Transactions on Medical Imaging. Jan 2013;32(4):P797-808
96. Amit Satpathy, Xudong Jiang. Human detection using Discriminative and Robust Local Binary Pattern. IEEE international conference on Acoustics, Speech and Signal Processing (ICASSP), Vancouver. 26-31 May 2013;P 2376 – 2380

97. Niraj P. Doshi, Gerald Schaefer. Texture classification using compact multi-dimensional local binary pattern descriptors. IEEE conference on Informatics, Electronics & Vision (ICIEV), Dhaka. 17-18 May 2013; P1-6
98. Ching-Te Chiu, Cyuan-Jhe Wu. Texture classification based low order local binary pattern for face recognition. IEEE international conference on Image Processing (ICIP), Brussels. 11-14 Sept. 2011; P 3017 – 3020
99. Taruna Aggarwal, Asna Furqan, Kunal Kalra. Feature extraction and LDA based classification of lung nodules in chest CT scan images. 2015 conference on Advances in Computing, Communications and Informatics (ICACCI), Kochi. 10-13 Aug. 2015; P 1189 – 1193
100. Lakshmi Devan, Roy Santhosham, R. Hariharan. Non-invasive Method of Characterization of Fibrosis and Carcinoma Using Low-Dose Lung CT Images. 2013 conference on Systems, Man, and Cybernetics (SMC), Manchester. 13-16 Oct. 2013; P 2168 – 2172
101. Huber MB, Bunte K, Nagarajan MB, Biehl M, Ray LA, Wismüller A. Texture feature ranking with relevance learning to classify interstitial lung disease patterns. PUBMED Artif Intell Med. 2012 Oct;56(2):91-7
102. Chang Y, Lim J, Kim N, Seo JB, Lynch DA. A support vector machine classifier reduces interscanner variation in the HRCT classification of regional disease pattern in diffuse lung disease: comparison to a Bayesian classifier. PUBMED Med Phys. 2013 May;40(5):051912

103. Zayed N, Elnemr HA. Statistical Analysis of Haralick Texture Features to Discriminate Lung Abnormalities. PUBMED Int J Biomed Imaging. 2015;2015:267807
104. Veeramani SK, Muthusamy E. Detection of abnormalities in ultrasound lung image using multi-level RVM classification. PUBMED J Matern Fetal Neonatal Med. 2015 Aug 10:1-9
105. Han F, Wang H, Zhang G, Han H, Song B, Li L, Moore W, Lu H, Zhao H, Liang Z. Texture feature analysis for computer-aided diagnosis on pulmonary nodules. PUBMED J Digit Imaging. 2015 Feb;28(1):99-115
106. Lam MO, Disney T, Raicu DS, Furst J, Channin DS. BRISC-an open source pulmonary nodule image retrieval framework. PUBMED J Digit Imaging. 2007 Nov;20 Suppl 1:63-71.
107. Ching-Wei, Cheng-Ping Yu Automatic Morphological Classification of Lung Cancer Subtypes with Boosting Algorithms for Optimizing Therapy. Springer Chapter, Machine Learning in Medical Imaging. Volume 7009 of the series Lecture Notes in Computer Science pp 217-224
108. Ching-Wei Wang , Cheng-Ping Yu. Automated morphological classification of lung cancer subtypes using H&E tissue images. Springer Machine Vision and Applications. October 2013, 24(7):p 1383-1391
109. Robert M. Haralick, K. Shanmugam and Its'hak Dinstein. Texture features for image classification. IEEE Transaction on system, man and cybernetics. Nov 1973;SMC-3(6):P610-621

110. Rusu M, Golden T, Wang H, Gow A, Madabhushi A. Framework for 3D histologic reconstruction and fusion with in vivo MRI: Preliminary results of characterizing pulmonary inflammation in a mouse model. *pUBMED Med Phys*. 2015 Aug;42(8):4822-32.
111. Rijal OM, Ebrahimian H, Noor NM, Hussin A, Yunus A, Mahayiddin AA. Application of phase congruency for discriminating some lung diseases using chest radiograph. *PUBMED Comput Math Methods Med*. 2015;2015:424970.
112. Ergen B1, Baykara M2. Texture based feature extraction methods for content based medical image retrieval systems. *PUBMED Biomed Mater Eng*. 2014;24(6):3055-62.
113. Farag A, Elhabian S, Graham J, Farag A, Falk R. Toward precise pulmonary nodule descriptors for nodule type classification. *PUBMED Med Image Comput Comput Assist Interv*. 2010;13(Pt 3):626-33.
114. Al-Kadi OS. Assessment of texture measures susceptibility to noise in conventional and contrast enhanced computed tomography lung tumour images. *PUBMED Comput Med Imaging Graph*. 2010 Sep;34(6):494-503.
115. Kakar M, Olsen DR. Automatic segmentation and recognition of lungs and lesion from CT scans of thorax. *PUBMED Comput Med Imaging Graph*. 2009 Jan;33(1):72-82
116. Nicolai Petkov. 2D Gabor functions and filters for image processing and computer vision. Intelligent Systems group Institute for Mathematics and Computing Science, University of Groningen. http://bmia.bmt.tue.nl/Education/Courses/FEV/course/pdf/Petkov_Gabor_functions2011.pdf

117. Fox MJ, Gibbs P, Pickles MD. Minkowski functionals: An MRI texture analysis tool for determination of the aggressiveness of breast cancer. PUBMED J Magn Reson Imaging. 2015 Oct 10
118. Spyropoulos-Antonakakis N, Sarantopoulou E, Trohopoulos PN, Stefi AL, Kollia Z, Gavriil VE, Bourkoula A, Petrou PS, Kakabakos S, Semashko VV, Nizamutdinov AS, Cefalas AC. Selective aggregation of PAMAM dendrimer nanocarriers and PAMAM/ZnPc nanodrugs on human atheromatous carotid tissues: a photodynamic therapy for atherosclerosis. PUBMED Nanoscale Res Lett. 2015 May 7;10:210.
119. Huber MB, Carballido-Gamio J, Fritscher K, Schubert R, Haenni M, Hengg C, Majumdar S, Link TM. Development and testing of texture discriminators for the analysis of trabecular bone in proximal femur radiographs. PUBMED Med Phys. 2009 Nov;36(11):5089-98.
120. Boehm HF, Fink C, Attenberger U, Becker C, Behr J, Reiser M. Automated classification of normal and pathologic pulmonary tissue by topological texture features extracted from multi-detector CT in 3D. PUBMED Eur Radiol. 2008 Dec;18(12):2745-55
121. Xiaoxing Li, Paulo R. S. Mendonça and Rahul Bhotika. Texture Analysis using Minkowski Functionals. <http://citeseerx.ist.psu.edu/viewdoc/download?doi=10.1.1.368.6392&rep=rep1&type=pdf>
122. Klaus R. Additivity, Convexity, and Beyond: Applications of Minkowski Functionals in Statistical Physics. Mecke Fachbereich Physik, Bergische Universität Wuppertal, Germany

123. DAVID LEGLAND, KIÊN KIÊU AND MARIE-FRANÇOISE DEVAUX. COMPUTATION OF MINKOWSKI MEASURES ON 2D AND 3D BINARY IMAGES. *Image Anal Stereol* 2007;26(2):83-92
124. D. Novikov, Hume A. Feldman and Sergei F. Shandarin. Minkowski Functionals and Cluster Analysis for CMB Maps. *International journal of modern physics D, Gravitation; Astrophysics and Cosmology*. Volume 08, Issue 03, June 1999.
125. Chapter 4 – calculating: Fractal dimension.
http://www.wahl.org/fe/HTML_version/link/FE4W/c4.htm
http://www.wahl.org/fe/HTML_version/link/FE4W/c4.htm
126. BENOIT B. MANDELBROT, DANN. E. PASSOJA, ALVIN J. PAULLAY. Fractal character of fracture surfaces of metals. *Letter to Nature* 308; 19 April 1984:P 721 - 722
127. Benoit B Mandelbrot. Self-Affine Fractals and Fractal Dimension. *Physica Scripta*. 13 June 1985;32(4)
128. Benoit B. Mandelbrot. Fractal analysis and synthesis of fracture surface roughness and related forms of complexity and disorder. 2006 Springer Netherlands, Book Title *Advances in Fracture Research*, Chapter: *Advances in Fracture Research*. p 13-17
129. Kido S, Tamura S. Computerized classification of interstitial lung abnormalities on chest radiographs with normalized radiographic index and normalized fractal dimension. *PUBMED Eur J Radiol*. 2001 Mar;37(3):184-9.
130. Kido S1, Kuroda C, Tamura S. Quantification of interstitial lung abnormalities with chest radiography: comparison of radiographic index and fractal dimension. *PUBMED Acad Radiol*. 1998 May;5(5):336-43.

131. Floyd CE Jr, Patz EF Jr, Lo JY, Vittitoe NF, Stambaugh LE. Diffuse nodular lung disease on chest radiographs: a pilot study of characterization by fractal dimension. PUBMED AJR Am J Roentgenol. 1996 Nov;167(5):1185-7.
132. Kido S, Ikezoe J, Naito H, Tamura S, Machi S. Fractal analysis of interstitial lung abnormalities in chest radiography. PUBMED Radiographics. 1995 Nov;15(6):1457-64.
133. Shimizu K, Johkoh T, Ikezoe J, Ichikado K, Arisawa J, Nakamura H, Tamura S, Nagareda T. Fractal analysis for classification of ground-glass opacity on high-resolution CT: an in vitro study. PUBMED J Comput Assist Tomogr. 1997 Nov-Dec;21(6):955-61.
134. Alceu Ferraz Costa, Gabriel Humpire-Mamani, Agma Juci Machado Traina. An Efficient Algorithm for Fractal Analysis of Textures. IEEE 2012 25th SIBGRAPI Conference on Graphics, Patterns and Images (SIBGRAPI), Ouro Preto. 22-25 Aug. 2012:P39 – 46
135. David G. Lowe. Distinctive Image Features from Scale-Invariant Keypoints. Springer International Journal of Computer Vision. November 2004;60(2):p 91-110
136. Jun Luo, Y. Ma, Takikawa, E. ; Lao, S. ; Kawade, M. ; Bao-Liang Lu. Person-Specific SIFT Features for Face Recognition. IEEE International Conference on Acoustics, Speech and Signal Processing, ICASSP. 15-20 Apr 2007;2:P 593-596.
137. Changyou Zhang , Xiaoya Wang, Jun Feng, Yu Cheng, Cheng Guo. A car-face region-based image retrieval method with attention of SIFT features. Springer Multimedia Tools and Applications. 22 February 2016:p 1-20

138. Ajmal Mian, Mohammed Bennamoun, Robyn Owens. An Efficient Multimodal 2D-3D Hybrid Approach to Automatic Face Recognition. *IEEE Transactions on Pattern Analysis and Machine Intelligence*. Nov. 2007;29(11):P 1927 – 1943
139. Zhimin Cao, Qi Yin, Xiaoou Tang, Jian Sun. Face recognition with learning-based descriptor. *IEEE Conference on Computer Vision and Pattern Recognition (CVPR)*, San Francisco, CA. 13-18 June 2010:P2707 – 2714
140. HaoxiangLi, Gang Hua, Zhe Lin, Jonathan Brandt, Jianchao Yang. Probabilistic Elastic Matching for Pose Variant Face Verification. *IEEE Conference on Computer Vision and Pattern Recognition (CVPR)*, Portland, OR. 23-28 June 2013:P3499 – 3506.
141. Chris Harris & Mike Stephens. A COMBINED CORNER AND EDGE DETECTOR. *In Proc. of Fourth Alvey Vision Conference 1998*; P 147-152.
142. Konstantinos G. Derpanis. Outline of the relationship between the difference-of-Gaussian and Laplacian-of-Gaussian. Department of Computer Science and Engineering, York University. September 19, 2006.
<http://citeseerx.ist.psu.edu/viewdoc/download?rep=rep1&type=pdf&doi=10.1.1.217.4931>
143. R.K. Sidhu. Improved canny edge detector in various color spaces. *IEEE 3rd International Conference on Reliability, Infocom Technologies and Optimization (ICRITO) (Trends and Future Directions)*; Noida. 8-10 Oct. 2014;P 1-6.
144. A. Jose, K.D.M. Dixon, N. Joseph, E.S. George, V. Anjitha. Performance study of edge detection operators. *IEEE Conference on Embedded Systems (ICES)*, Coimbatore. 3-5 July 2014;P 7-11.

145. Andrew P. Witkin. Scale-Space filtering: A new approach to multi-scale description. IEEE International Conference on Acoustics, Speech, and Signal Processing ICASSP '84. Mar 1984;9:P150 – 153
146. Mehrdad Alemzadeh, Colm Boylan, Markad V. Kamath. A Review of Texture Quantification of CT images for classification of Lung Diseases. Begell House Critical Reviews in Biomedical Engineering. 2015; 43(2-3):P183-200.
147. Rojas, Raul. Neural Networks A Systematic Introduction. Springer-Verlag Berlin Heidelberg. Edition 1, eBook ISBN 978-3-642-61068-4
148. Shigeo Abe. Support Vector Machines for Pattern Classification. Advances in Computer Vision and Pattern Recognition, 2010 Springer-Verlag London. Edition 2 eBook ISBN 978-1-84996-098-4
149. Ricardo Gutierrez-Osuna. Intelligence Sensor Systems, Lecture 13: Validation. Wright State University. http://research.cs.tamu.edu/prism/lectures/iss/iss_113.pdf